European Commission

JRC SCIENTIFIC AND POLICY REPORTS

Assessment of the seismic vulnerability of an old RC viaduct with frame piers and study of the effectiveness of base isolation through PsD testing (RETRO)

SERIES Transnational Access report

Fabrizio Paolacci, Pierre Pegon, Francisco Javier Molina, Martin Poljansek, Renato Giannini, Luigi Di Sarno, Giuseppe Abbiati, Arkam Mohamad, Oreste Bursi, Fabio Taucer, Rosario Ceravolo, Philippe Caperan, Luca Zanotti Fragonara, Raffele De Risi, Mauro Sartori, Silvia Alessandri Cem Yenidogan

2014

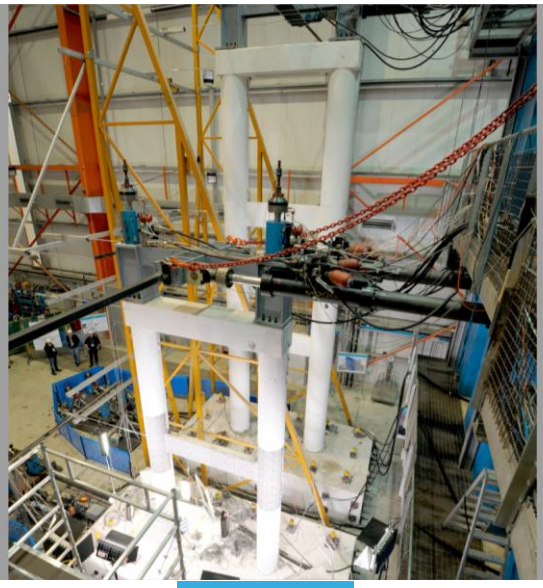

Report EUR 26471 EN

Joint Research Centre

European Commission
Joint Research Centre
Institute for the Protection and Security of the Citizen

Contact information
Fabio Taucer
Address: Joint Research Centre, Via Enrico Fermi 2749, TP 480, 21027 Ispra (VA), Italy
E-mail: fabio.taucer@jrc.ec.europa.eu
Tel.: +39 0332 78 5886
Fax: +39 0332 78 9049

http://elsa.jrc.ec.europa.eu/
http://www.jrc.ec.europa.eu/

This document replaces "Assessment of the seismic vulnerability of an old RC viaduct with frame piers and study of the effectiveness of base isolation through PsD testing (RETRO)" with ISBN number 978-92-79-35271-3 and PUBSY request number JRC87771. The corrections made in the new document are: i) changed the date on p. 5 from 21.01.2014 to 18.02.2014; ii) replacement of the term "pseudodynamic technique with substructuring" by the term "continuous pseudo-dynamic technique with non-linear substructuring" in the Abstract and in Section 2; iii) updating of Table 5.1 and of third paragraph of Section 5.1; iv) updating of first paragraph of Section 7.3; v) updating of Table 9.1 and more in general of Section 9; vi) updating of Section 10.1.1; vii) updating of the legend of Figure 10.6; viii) updating of Section 10.3.2; ix) updating of Conclusions.

JRC89069

EUR 26471 EN

ISBN 978-92-79-36477-8

ISSN 1831-9424

doi: 10.2788/33048

Luxembourg: Publications Office of the European Union, 2014

Printed in Ispra Italy

SEVENTH FRAMEWORK PROGRAMME
Capacities Specific Programme
Research Infrastructures
Project No.: 227887

SERIES
SEISMIC ENGINEERING RESEARCH INFRASTRUCTURES FOR EUROPEAN SYNERGIES

Work package 6

RETRO
Assessment of the seismic vulnerability of an old RC viaduct with frame piers and study of the effectiveness of base isolation through PsD testing on a large scale model

TA Project Final Report

Work Package Leader: Fabio Taucer, Joint Research Centre
User Group Leader: Fabrizio Paolacci, University Roma Tre
Final: 18.02.14

2014

This page is intentionally left blank.

Abstract

The RETRO project aims at studying the seismic behaviour of existing reinforced concrete bridges (RC) and the effectiveness of innovative retrofitting systems. Emphasis has been paid on old bridges generally not properly designed for seismic action. On the basis of a previous experimental campaign consisting of cyclically imposed displacements on 1:4 reduced scale models of a frame pier, belonging to a typical old RC highway viaduct, a new experimental activity has been proposed. Two specimens (scale 1:2.5), a frame pier of 2 levels (height 5.8 m) and a frame pier of 3 levels (height 10.3 m), have been built and tested using the continuous Pseudo-dynamic (PsD) method with non-linear substructuring technique, including the modelling of the remaining entire viaduct to which they belong. Two test configurations have been considered: 1) retrofitted viaduct using Friction Pendulm Isolators, and an 2) "as-built" configuration imposing a Serviceability and Ultimate limit state conditions. For each phase of the experimental campaign model identification has been performed. The aim of the campaign was twofold: 1) increasing the knowledge on the non-linear behaviour of RC frame piers in presence of plain steel bars and detailing of the late 1950's for which few studies have been carried out, and 2) study the effectiveness of seismic isolation systems for the seismic response mitigation.

Keywords: Reinforced Concrete bridge, Plain steel bars, Frame piers, Deck Isolation, Friction Pendulum Bearings, Experimental Analysis, Numerical Simulations, Pseudo-Dynamic Tests.

Acknowledgments

The research leading to these results has received funding from the European Union Seventh Framework Programme [FP7/2007-2013] under grant agreement n° 227887 [SERIES].

This report and particularly the test campaign is the work not only of the authors but also of numerous colleagues in the ELSA laboratory who have done a fantastic work setting up and running the experiments and being so generous with their knowledge in the design and execution of the tests performed. This project would not have been possible were it not for the contributions of the colleagues listed below.

Bernard Viaccoz
Georges Magonette
Patrick Petit
Marco Peroni
Raoul Kiefer
Giuseppe Bof
Antonio Zorzan
Olivier Hubert
Jose Esteves

Report Contributors

University Roma Tre	Fabrizio Paolacci
	Renato Giannini
	Silvia Alessandri
	Arkam Mohamad
European Commission - JRC	Martin Poljanšek
	Pierre Pegon
	Francisco Javier Molina Ruiz
	Fabio Taucer
	Philippe Caperan
University of Sannio	Luigi Di Sarno
University of Naples "Federico II"	Raffaele De Risi
University of Trento	Oreste S. Bursi
Politecnico of Torino	Rosario Ceravolo
	Luca Zanotti Fragonara
Alga Spa, Milan	Mauro Sartori

Table of contents

1. INTRODUCTION

The seismic vulnerability assessment of existing and new lifeline systems, especially transportation systems, is becoming of paramount importance in resilient social communities. Bridge systems and highways are primary elements that can be utilized for rescue operations in the aftermath of moderate-to-major earthquake ground motions. Most of today's existing transportation systems in Europe were built chiefly in the late 60s and early 70s and were designed primarily for gravity loads. As a result, such systems do not employ seismic details and hence their structural performance is inadequate under earthquake ground motions.

Recently, a comprehensive research program (Reluis DCP 2005-2008 – Research Thrust 3 – Prof. P.E. Pinto and G. Mancini) was initiated in Italy to formulate pre-normative European guidelines for the assessment of existing bridges. This novel program was motivated by the urgent needs to assess the seismic vulnerability and retrofit of existing bridge structures. The outcomes of the aforementioned research are summarized in [1]. However, a number of design issues require further developments. The implementation of comprehensive guidelines for the seismic assessment and retrofit of existing bridges is time consuming as it requires the thorough understating of complex local and global response mechanisms. Full scale testing programs should be employed to validate provisional models and to assess their reliability for parametric analyses. In the US it took more than ten years, dating back to the failures of modern bridges during the San Fernando (1971) earthquake, for the Federal Highway Administration (FHWA) to issue the "Retrofitting guidelines for Highway Bridges" [2].

Since 1992, a refined research program funded by FHWA has been undertaken in the US to investigate a number of topics related to the seismic assessment and retrofit of bridges [3] [4]. The European standards, i.e. Eurocodes, include a document for the seismic design of new bridges, namely Eurocode 8 Part 2 [5]. Part 3 of Eurocode 8 [6] addresses existing buildings, but there is no part of Eurocode 8 covering existing bridges. The assessment of the seismic vulnerability of existing bridges is a complex process. The assessment scheme requires a comprehensive dataset, which is often unavailable due to the lack of information, especially for reinforced concrete structures (adequate knowledge of the mechanical and geometrical characteristics of the structure and materials, information on structural modification occurred during the life of the bridge, a reliable estimation of the gravity load, etc.). These difficulties

affect detrimentally the seismic response evaluation, and as a result the structural vulnerability cannot not reliably be estimated.

The evaluation of the expected seismic response of bridge structures is influenced by several uncertainties relative to mechanisms characterizing the post-elastic structural response. As a result, the effective use of methods and processing tools employing nonlinear analyses is often prohibitive and/or misleading. Nevertheless, non-linear procedures are becoming popular in the frameworks of structural assessment, thus, there is a need to accurately model the dissipative zones to provide reliable indications about the performance of the structure. In addition, the steel reinforcement of old constructions was comprised mainly by smooth steel bars. The influence of such bars in the response of the structure, especially their bond and anchorage mechanisms, has not been adequately investigated (both numerically and experimentally) in the past. Existing formulations simulating the behaviour of smooth bars and their anchorage shows that the existing experimental tests appear old and not comprehensive. Conversely, in recent years, this problem has been reconsidered and a systematic approach to the study of bond-slip and anchorage efficiency of plain steel bars has been adopted [7] [8] [9].

Another interesting issue is the rehabilitation of old bridges using innovative techniques. Seismic isolation is an effective way to reduce the response of bridges designed for vertical loads only. This technique, widely studied in the past, has been marginally investigated concerning its effectiveness on old bridges. In addition, further comparative analyses, numerical and experimental, are needed to better understand the performance of different isolation systems [10] [11].

Finally, the introduction of innovative retrofitting schemes, e.g. based on active/passive control technologies and application of FRPs in critical regions, call for models with predictive capacity. To do so, structural identification and monitoring are expected to play an important role. Considering that only a limited number of dynamic features of an existing bridge can be extracted from experimental modal analysis [12], new non-linear identification techniques should be developed and tested in the future to capture the global dynamic response at the ultimate limit states [13]. In view of the strategic nature of transportation infrastructures a further thorough study is becoming urgent and is deemed necessary. Towards this end, experimental test programs are vital to characterize the quality and quantity of typical structural systems. Furthermore, a scarce experimental activity on old reinforced concrete structures renders this topic crucial for future assessment guidelines [14] [15] [16]

[17] [18]. As a result, the state of the art on seismic assessment and retrofit of old bridges requires further advancement.

2. OBJECTIVES

RETRO' project aims at studying the seismic behaviour of existing reinforced concrete (RC) bridges and the effectiveness of innovative retrofitting systems. The research program focuses on old bridges, not properly designed for seismic action. In particular, the seismic vulnerability of an old Italian viaduct with portal frame piers has been evaluated. A proper isolation system has been designed using Slide Spherical Bearings (SSB). In this report the non-linear response of the case study "Rio-Torto" viaduct in "as-built" and "isolated" configurations has been tested through an experimental test campaign considering two prototype piers.

The experimental test campaign described herein follows a previous experimental campaign consisting of cyclically imposed displacements on 1:4 reduced scale models of a reinforced concrete portal frame pier, belonging to a typical old highway viaduct. In particular, two specimens (scale 1:2.5), a 2-level and a 3-level one-bay reinforced concrete frame, were constructed and tested using the continuous pseudo-dynamic (PsD) technique with non-linear substructuring, including the modelling of the entire viaduct. During the test, different configurations were considered, namely the retrofitted viaduct using Spherical Sliding Bearings and the "as-built" viaduct.

The main goals of the proposed experimental activity are:

(i) Increasing the knowledge on the non-linear behaviour of portal frame piers in presence of plain steel bars for which few studies have been carried out.

(ii) Employment of large-scale experimental tests for the seismic assessment of existing bridges.

(iii) Study of the effectiveness of traditional and innovative seismic isolation systems (FP isolators).

3. DESCRIPTION OF RIO-TORTO BRIDGE

3.1. Geometric characteristics

Rio Torto bridge is an old reinforced concrete bridge consisting of a thirteen-span bay deck with two independent roadways supported by 12 couples of portal frame piers (Fig. 3.1), each composed by two solid or hollow circular columns of variable diameter (120-160 cm), connected at the top by a cap-beam and at various heights by one or more transverse beams of rectangular section.

Figure 3.1 A view of Rio Torto bridge

The height of the piers varies between 13.8 m, near the abutments, to 41 m, at the center of the bridge. The deck is constructed by two "∏" shape reinforced concrete beams 2.75 m high (Fig. 3.2) interrupted by Gerber saddles (Fig. 3.3) placed at the second, seventh and twelfth bays. The deck is connected to the piers by two steel bars inserted in the concrete, whereas the bearings at the abutments are constructed with fixed devices.

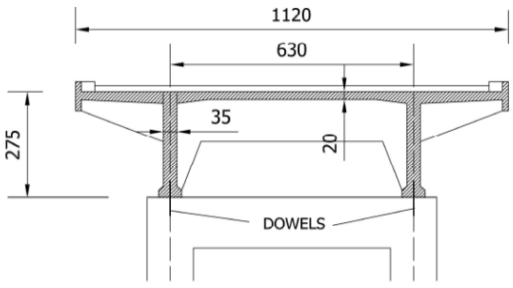

Figure 3.2 Cross-section of the deck

Figure3.3. Garber Saddles

The cross section properties of the deck are given in following table.

Table 3.1 Deck characteristics

Area [m^2]	J [m^4]	I_y [m^4]	Iz [m^4]
4.6621	**0132375**	**51.87**	**3.466**

The columns have two types of cross-sections: a solid circular one with diameter of 120 cm and a hollow section with external and internal diameters equal to 160 cm and 100 cm respectively. Details of the longitudinal steel bars in these two sections are illustrated in Fig. 3.4 for piers 9 and 11.

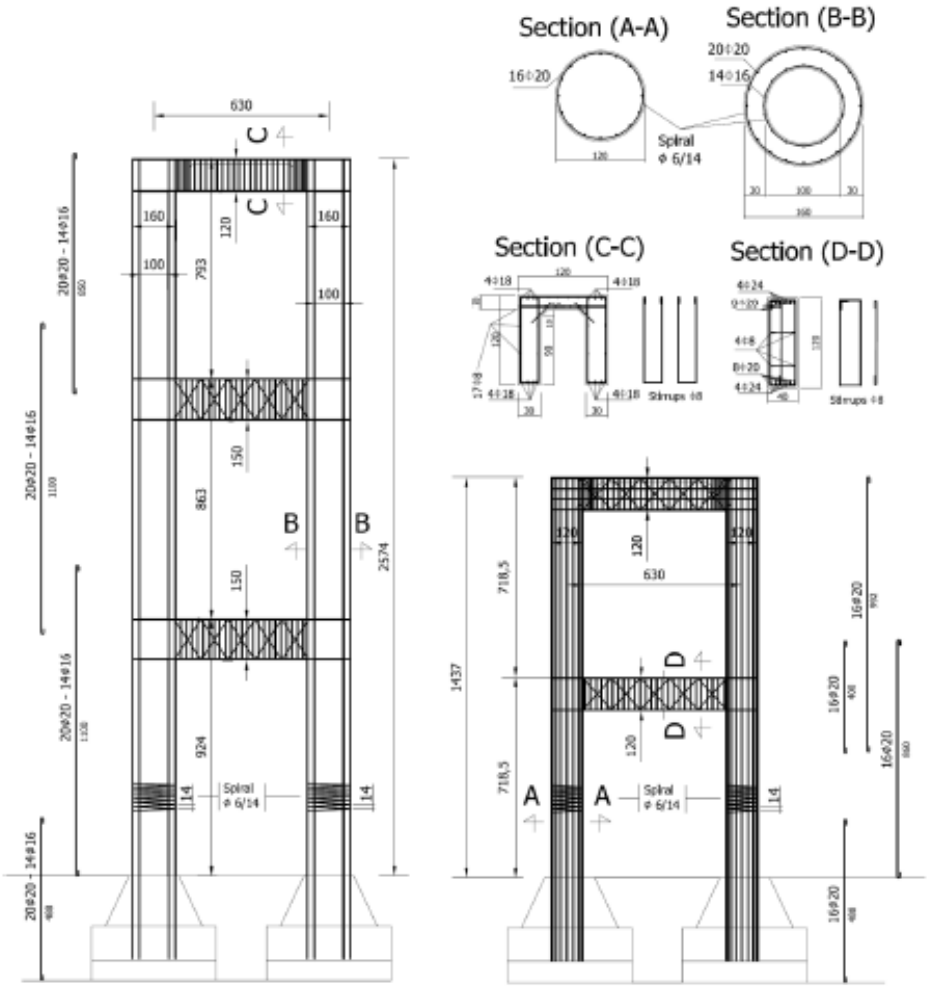

Figure 3.4 Reinforcement details of pier 9 and 11

In order to carry out the PsD test of the viaduct with substructuring, piers 9 and 11 were reproduced at a scale of 1:2.5, whereas the remaining part of the viaduct was numerically simulated. The details of the reinforcement of each portal frame and the geometry of each pier can be found in [19]. The overall dimensions of the piers are illustrated in Fig. 3.5.

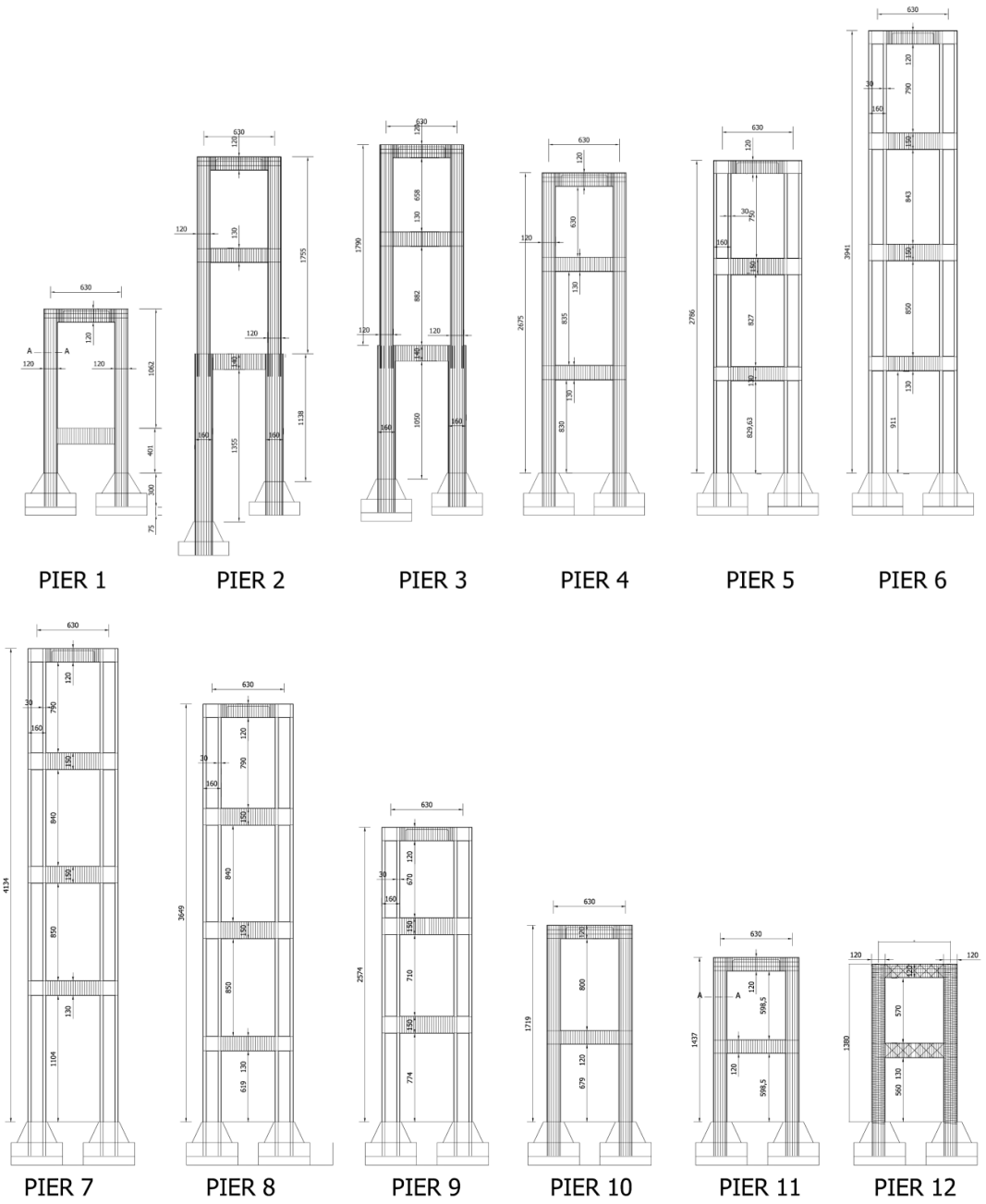

Figure 3.5 Overall dimensions of all piers (full scale)

3.2. Material properties

Limited data about the materials used in the bridge is available. The class of concrete corresponds to a mean resistance of 30 MPa, while the class of steel used in Italy when the bridge was constructed was AQ42, corresponding to a mean strength of 350 MPa [20]. To increase the knowledge on the material properties of the bridge, in-situ tests should be carried out. The possibility of doing them is under investigation.

3.3. Vertical loads

The overall weight of a single deck component is indicated in the following table:

Table 3.2 Vertical loads distributions

Element	Thickness [m]	Area [m²]	Volume weight [kN/m³]	Total weight [kN/m]
R.C. Deck	--	4.48	25	112
Slab				6
Stiffeners				10
Concrete asphalt (thickness 15 cm)	0.15	2	24	30
Guard Rail	--	--	--	2
Waterproofing membrane	0.04	0.5	20	1
Parapet				5
TOTAL				≈ 170 kN/m

Considering that the length of the bays varies between 33 and 29 meters, the permanent vertical load at acting on each pier varies between 5600 kN and 5300 kN. The total weight acting on piers 9 and 11 is equal to 5600 kN (2800 kN for each column).

3.4. Reinforcement details

The details on the placement of the longitudinal steel bars in the solid and hollow circular sections of the columns are illustrated in (Fig. 3.6). The solid section has bars ϕ 16 mm, whereas the hollow section has ϕ 16 and ϕ 14 mm steel bars, externally and internally, respectively. The transverse reinforcement for all the columns consists of a ϕ 6 mm steel spiral with a spacing of 14 mm.

The transverse beams have a rectangular section with a width of 40 cm and a height varying between 120 cm and 150 cm. The longitudinal reinforcement consists of ϕ 24 and ϕ20 steel bars. The transverse reinforcement consists of ϕ8 steel bars spaced at 20 cm and inclined at 45°. The cap-beam of all piers presents a U-shape section, with ϕ 18 longitudinal steel bars and ϕ 8 mm transverse reinforcement. The reinforcement details of all piers are illustrated in [21].

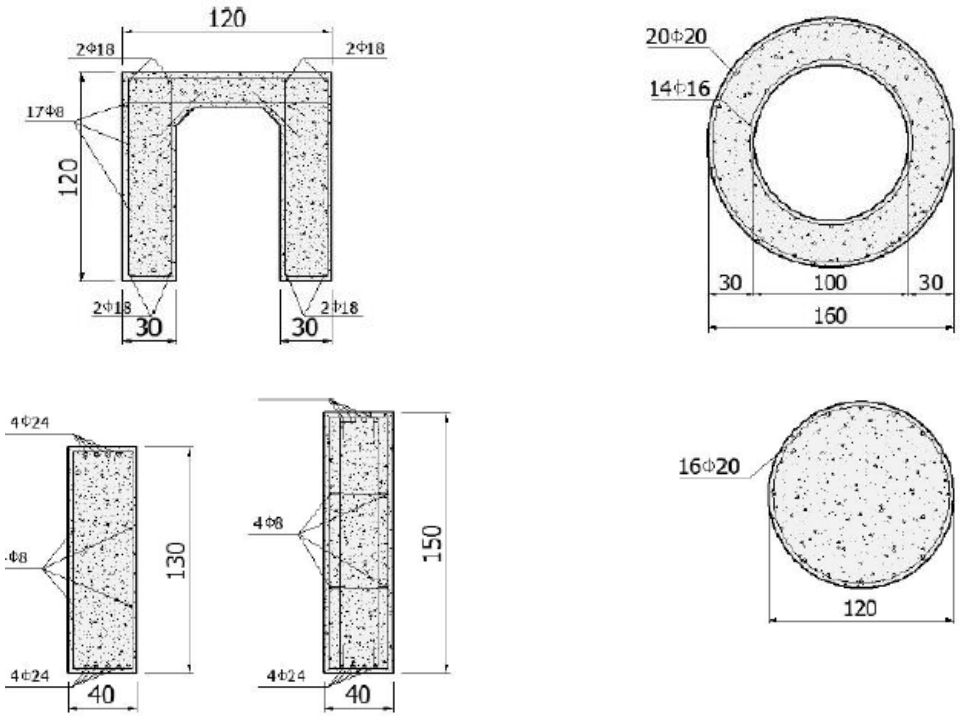

Figure 3.6 Full-scale cross-sections of the transverse, the cap-beam, and the columns

3.5. Soil conditions

Fig. 3.7 shows the geological map of the zone where the Rio-Torto viaduct is placed. From the analysis of the map emerges that the viaduct was built on an extensive zone of argillite calcareous (light green zone) and on lens of sandstones (white-red zones).

Figure 3.7 Geological conditions of the zone

3.6. Seismogenic zone and response spectra

The viaduct was constructed on a zone with moderate-to-high seismic activity. The seismogenic zone (913, according to the Italian catalogue) where the bridge is placed is indicated in Fig. 3.8a.

The associated shaking map (from INGV) shows (Fig. 3.8b) that the expected PGA ranges between 0.23g and 0.25g for the life safety condition (probability of 10% in 50 years), whereas for the collapse prevention condition (probability of 2% in 50 years) PGA ranges between 0.30g and 0.35g.

For the current Italian seismic code, assuming rigid soil conditions (soil A), nominal life = 100 years and class of construction = IV, the maximum PGA for the following limit states is: PGA = 0.147g for immediate occupancy, PGA=0.308g for life safety and PGA=0.334g for collapse prevention. This is consistent with the indications of the INGV shaking map. The response spectra for the different limit state conditions are illustrated in (Fig. 3.9).

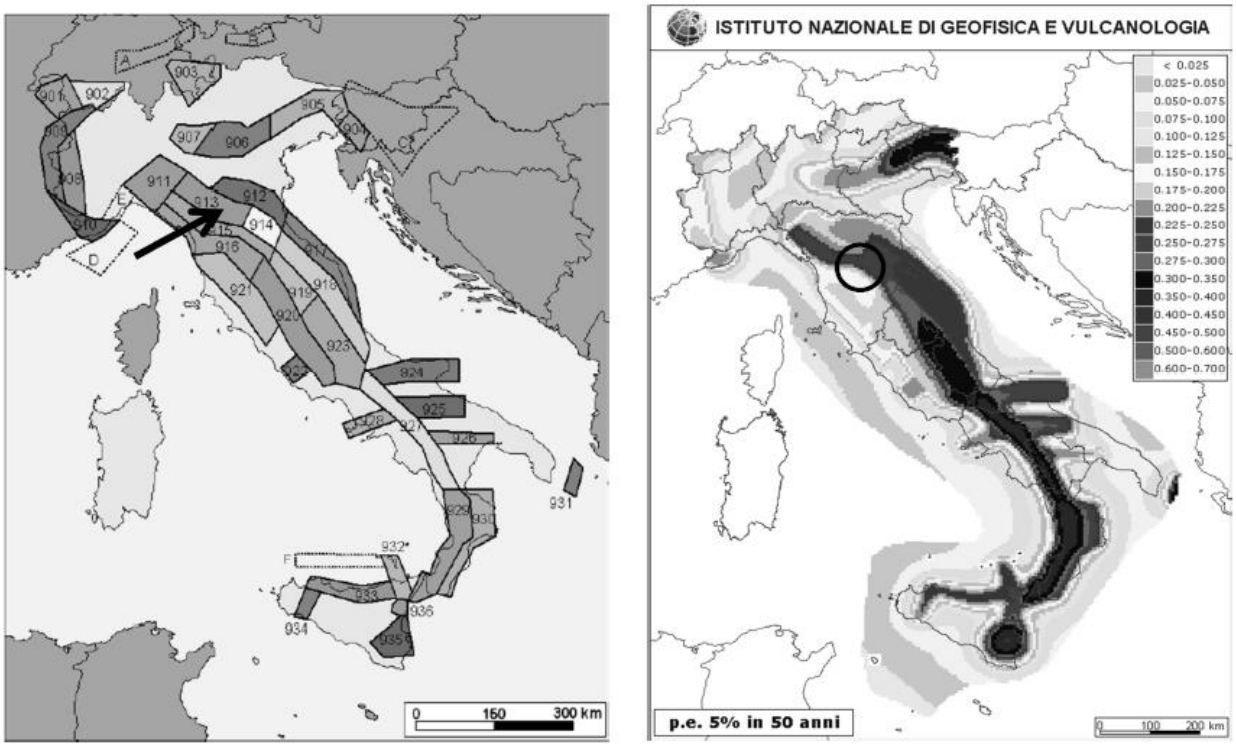

Figure 3.8 (a) Seismogenic zones (b) Italian ground shaking intensity map on Bedrock (INGV)

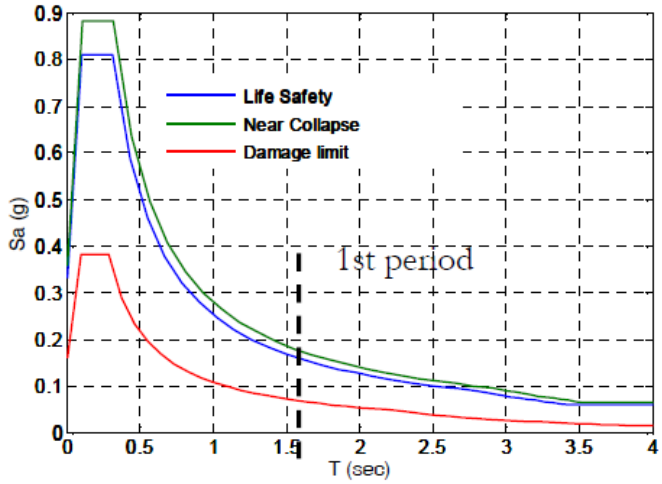

Figure 3.9 Response spectra of the viaduct according to the current Italian code (Soil A)

The most recent database on the historical seismic activity of zone 319 evidences earthquakes with magnitude ranging from 6.13 to 6.6; no active faults have been identified.

In order to obtain preliminary results on the seismic hazard at the site the results obtained using the MathHazard software are presented [22]. The program is based on the Gutemberg-Richter law to estimate the probability of occurrence of the earthquake and on the Sabetta-Pugliese attenuation law to provide the probability of occurrence for a given exposition time. The results are summarized in Fig. 3.10, where the seismogenic zones used in the simulation and the corresponding hazard function for an exposition time of 50 years are shown.

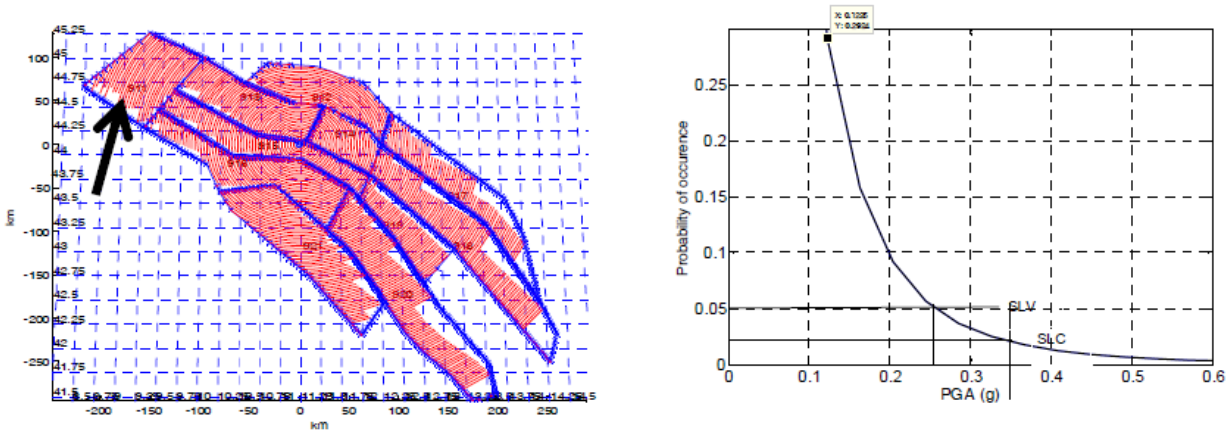

Figure 3.10 (a) Seismogenic zone of the viaduct (b) seismic hazard in terms of PGA for 50 years

The results are in agreement with the hazard result provided by the Italian regulation and the INGV. In particular, PGAs of 0.25g (Life safety limit state - SLV) and 0.33g (Collapse limit state - SLC) are obtained for probabilities of occurrence of 5% and 2% over a 50 year period, respectively.

4. DESIGN OF THE FP ISOLATION SYSTEM

The isolation system adopted in this test includes the Friction Pendulum (FP) system (e.g. [23], [24], among many others). The design of the FP devices was carried out with a displacement-based procedure focusing on two objectives:

(a) Keep the piers in the (quasi-) elastic range of response.
(b) Minimize the displacement demand on the expansion joints located at the abutments.

In general, there are three basic types of FP devices used for new and existing constructions:

(i) Isolators with one spherical sliding surface that may be at the top or at the bottom of the device, connected to a spherical hinge.
(ii) Isolators with two main spherical surfaces and an interposed point rocker articulation that allows relative rotations (e.g. [25]).
(iii) Devices with two perpendicular cylindrical surfaces and two perpendicular cylindrical articulations allowing two relative rotations [26].

The selection of the FP device to be used in a specific project depends on the structure to be retrofitted. The type of FP depends on the allowable displacement of the structural system. Such displacements generally control the design of the isolators. The second type is often used to minimize the plan dimensions of the isolator and to limit the vertical load eccentricity caused by the horizontal displacement. The third type is used when a different behaviour is required in two perpendicular directions. The first type is the most commonly adopted due to its simplicity and was adopted to seismically isolate the Rio Torto bridge, which is characterized by relatively low displacements and similar response along the lateral and transverse directions. The basic elements of a single-surface FP, as shown in Fig. 4.1, are: the upper anchor plate (1), the sliding surface (2), the sliding material interface (3), the rotation element (4), the rotation sliding surface (5) and the lower anchor plate (6).
From a mechanical standpoint, the FP devices are characterized by a bilinear force displacement relationship:

$$V_{FPS} = \mu_f . N + \frac{N}{R} . \Delta_{iso} \quad (4.1)$$

Where μ_f is the friction coefficient, N is the normal force, R is the device curvature radius and Δ_{iso} is the sliding displacement in the isolator. Fig. 4.2 provides a typical hysteretic behaviour obtained during dynamic tests on a FP with a single sliding surface.

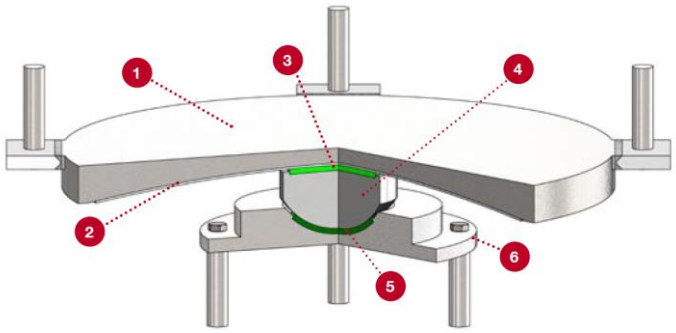

Figure 4.1 Single sliding surface friction pendulum system (courtesy of ALGA S.p.A)

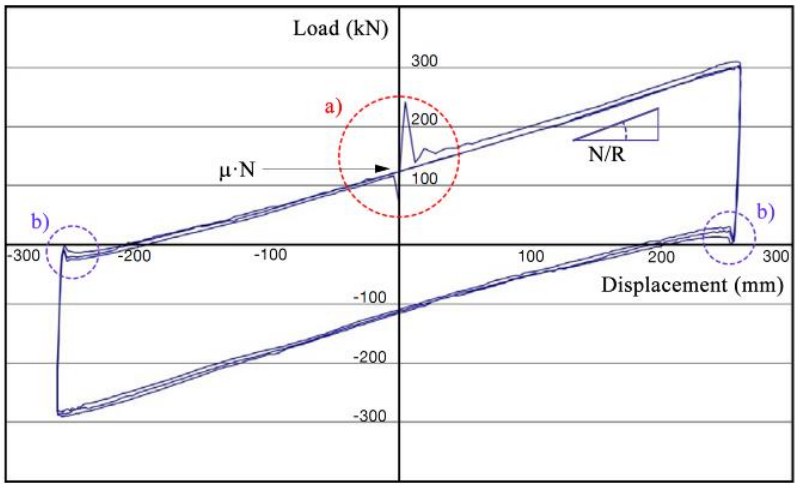

Figure 4.2 Hysteretic behaviour obtained during dynamic tests on single concave surface sliding pendulum

The variation of the friction coefficient relative to the breakaway of the motion (a) and change in sign of velocity (b) is also displayed in Fig. 4.2.

The FP isolation system was designed according to a displacement-based design method that is presented in detail in [27]. The method is based on the direct displacement based procedure proposed by Priestley *et al*. [28] A few modifications have been proposed to the general method and specific design tools were developed for the case of isolation by means of FPS. It

is worth mentioning that the adopted methodology for the specific case study is focused on the design of FP systems, but it can be easily extended to other systems exhibiting a bilinear hysteretic behaviour. The FPS designed for the seismic retrofitting of the Rio Torto had a radius of 3 m, a friction coefficient of 4%, an articulated slider of 9 cm height and an initial yield displacement of 0.5 mm. Nonlinear response history analyses for the base isolated model of the Rio Torto bridge were carried out by using the 20 and 29 May Emilia (Italy) earthquakes.

5. DESCRIPTION OF PIERS MOCKUPS

5.1. Scaling

When performing an experimental test on a specimen the problem of scale reduction needs to be addressed. This is solved by making use of a dimensional analysis governed by the well-known Buckingham Theorem.

A suitable scale reduction factor should be assumed in order to reduce lengths (Geometry and displacements) at a level compatible with the requirements of the experimental setup, especially in terms of maximum capacity of the actuators (Forces). This automatically reduces the cost of the experiment.

Table 5.1 Scale factors used in a PsD test

Quantity	Dimension	Scale Factor
Length	L	S
Stress	$ML^{-1}T^{-2}$	1
Strain	L/L	1
Force	MLT^{2}	S^{-2}
Stiffness	MT^{2}	S

Thus the only reduction factors to be selected are those of length and forces. The others can be evaluated by a dimensional analysis. If we assume that the model is made of the same material of the prototype, stress and strain can be kept constant. Forces and displacements are reduced by S^2 and S respectively, as shown in Table 5.1. The reduction factors of time and acceleration may be selected according to the needs of the test [29]; for the PsD method they lose their meaning because of the quasistatic implementation of the experiment.

Considering the constraints for the construction and the positioning of the specimens in the laboratory, in particular the dimensions of the reaction wall and of the access door, a reduction scale of 1:2.5 was selected.

5.1.1. Flexural and shear strength scaling

The correct flexural strength of columns and transverse beams was achieved with a rigorous geometrical scaling of the prototypes, including the diameters of reinforcement and their position. In particular for the columns of both piers 9 and 11, plain steel bars with diameters of 8 and 10 mm were used to respect the similitude requirements, given that the original diameters of the prototype are 20 and 24 mm, with a small approximation for the 24 mm diameter bars.

Regarding the shear strength the problem deserves particular attention. Many authors in the past have clarified the problem [30]. In particular, it is necessary to scale diameter and spacing of stirrups to have a correct strength and confinement effect. Concerning piers 9 and 11, scaling of shear strength is particularly important for the transverse beams, while for the columns it is less of an important issue, owing to their high shear strength. For the transverse reinforcement of the transverse beam, with 8 mm diameter stirrups at maximum spacing of 20 mm for the prototype, a scaled diameter of 3 mm diameter stirrups with a spacing of 8 mm was selected. Consequently, whereas a correct scaling of the confinement effect is respected, the shear strength is slightly underestimated, but considered acceptable for the test campaign. The total shear strength can be calculated according to [31].

$$V_t = V_c + V_s + V_p \tag{5.1}$$

$$V_c = k\sqrt{f_c}\,0.8A_c \tag{5.2}$$

$$V_s = \left(\frac{A_{sw}}{s_s}\right) f_y D \cot\theta + \frac{\sin\beta A_{sp}}{s_p} f_y D\,(\cot\theta + \cot\beta) \tag{5.3}$$

$$V_p = P\tan\alpha \tag{5.4}$$

where k is a curvature ductility-dependent coefficient, fc is the compressive concrete strength, f_y is the steel strength, Ac is the cross section area, Asw is the stirrups area and Asp is the area of inclined rebars (with angle β) and spacing ss and sp respectively. P is the normal force and α is the angle of inclination of the ideal line connecting the normal forces at top and bottom of the element. D is the distance between rebars at the top and bottom of the section. For

example, the shear strength of pier 11 assuming *k=0.2*, corresponding to a ductility of 3, *fc=26 MPa, fy=350 MPa, ss=20 cm, sp=114* and θ*=45°* cm, leads to *Vc=390 kN, Vs=520 kN*. Because *P*~0 the total strength of the transverse beam of pier 11 is V_t*=900 kN*. Consequently, a correct reduced scale model should have a shear strength $V_t=900/2.5^2$ *= 144 kN*, obtained using stirrups with a diameter of 3.2 mm. Since the closest diameter available on the market is 3, even if the confinement effect is respected given that the spacing was correctly scaled, the actual strength of the scaled model is V_s*=81.6 kN*. The approximation can be considered acceptable

5.1.2. Scaling of the bond slip phenomenon

More delicate is the scaling effect on concrete–steel bond conditions. Past experimental tests have shown that scaling may have a relevant influence on the bond of deformed bars, especially in terms of slippage and crack propagation [32]. In the case of plain steel bars, its influence can still be considered significant [33] [34]. However, since experimental evidence has demonstrated that in this case the anchorage effect of hooks prevails [7], the adopted geometrical scaling can be accepted.

According to the scaling effect described in the previous paragraphs the specimens were designed by Roma Tre. For example, in Fig. 5.1 the reinforcement of the cap-beam and of a transverse beam of pier 9 is shown. The full drawings of both the mockups are presented in Appendix C.

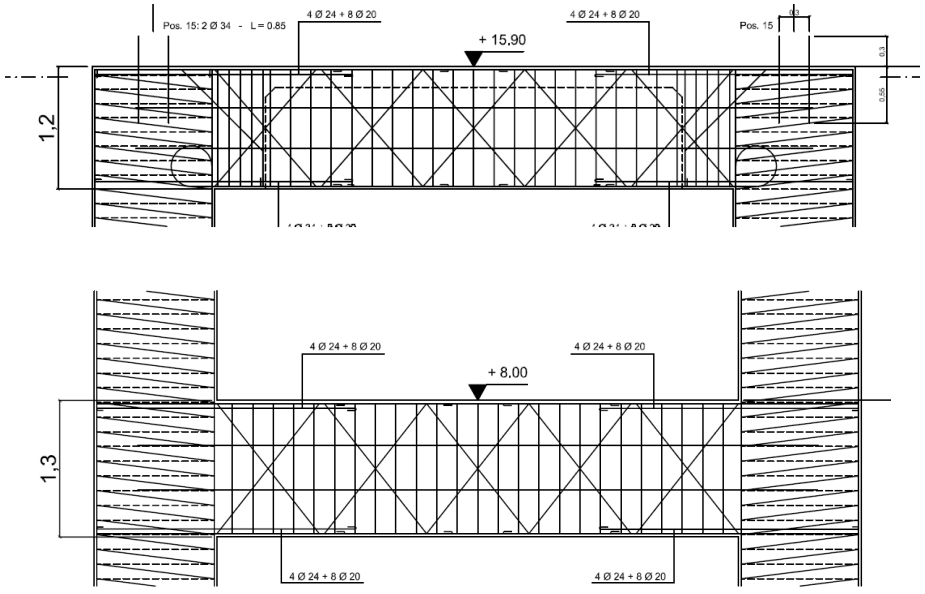

Figure 5.1 Reinforcement of cap and transverse beam of the tall pier

5.1.3. Scaling of the FP devices

According to [35], the full scale model of FP isolators designed according to displacement-based design should have a Radius *R*=3000 mm and a friction coefficient equal to 4%. The permanent loads axial force is approximately 7500 kN, whereas the seismic axial force is about 2800 kN. The constitutive law corresponding to the above parameters is therefore the following:

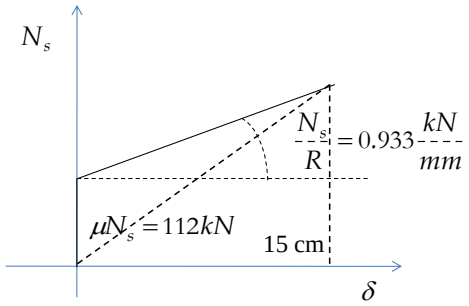

Figure 5.2 Constitutive low relationships

The effective stiffness corresponding to a displacement level of 15 cm is:

$$K_{eff} = \frac{N}{R} + \frac{\mu N}{D} = \frac{2800}{3000} + \frac{0.04 \times 2800}{150} = 1.68\ kN/mm \qquad (5.5)$$

Consequently the effective period is equal to

$$T_{eff} = 2\pi\sqrt{\frac{m}{K_{eff}}} = 2\pi\sqrt{\frac{N}{gK_{eff}}} = 2\pi\sqrt{\frac{2800}{9810 \times 1.68}} = 2.58\ sec \qquad (5.6)$$

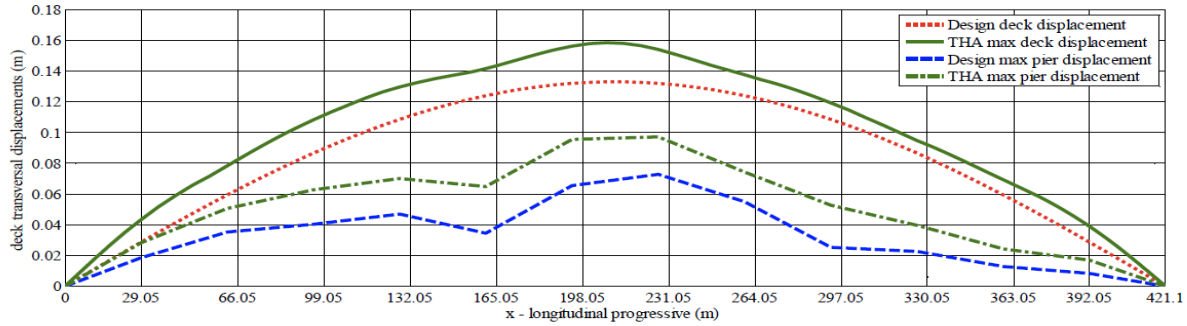

Figure 5.3 Maximum deck displacements

In Fig. 5.3 is shown the performance of the viaduct in terms of displacement based on non-linear dynamic analyses on a refined model [35]. The mode of failure of the piers is mainly given by shear failure of the transverse beams.

In order to respect the similitude requirements the 1:2.5 reduced scale model of FP isolators should have the following characteristics:

Radius: R=3000 /2.5 = 1200 mm

Friction coefficient: μ=4%

In fact, the equivalent stiffness and the effective period becomes respectively K_{eff}=*0.672 kN/m* and T_{eff}=*1.63 sec.*

5.2. Geometry and detailing of the piers mock-ups

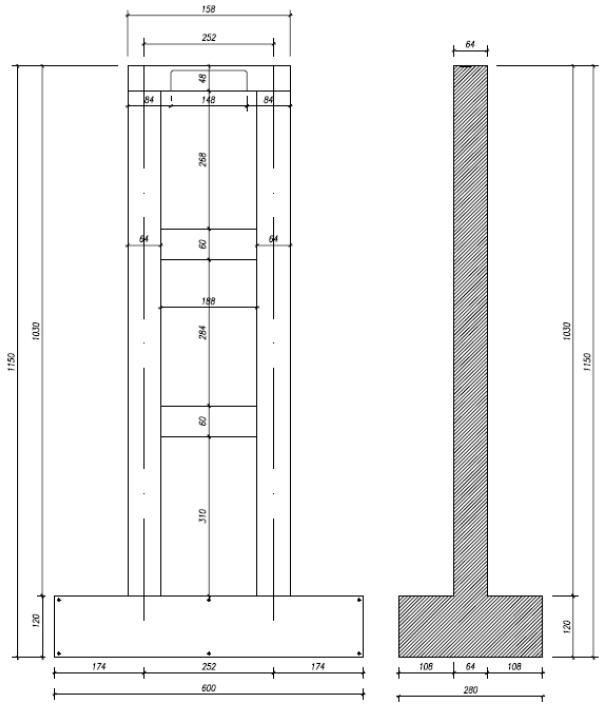

Figure 5.4 Geometry of pier 9

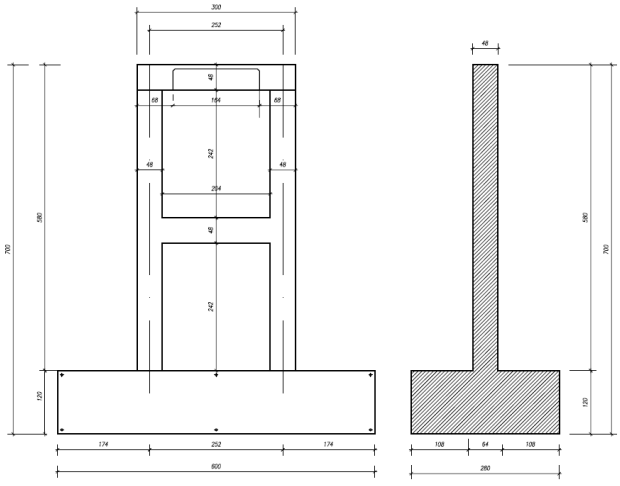

Figure 5.5 Geometry of pier 11

In the test campaign, two specimens of the piers of the Rio Torto viaduct were constructed and tested experimentally with the PsD testing technique. The first specimen, related to pier 11; is a 2 level 1-bay pier with a total height (including the base) of 700 cm. The second

specimen, related to pier 9, is a 3 level 1-bay pier with a total height of 1150 cm. The base of both piers is rectangular, 600 cm long and 280 m wide (Fig. 5.4 and Fig. 5.5).
The full drawings and steel detailing could be found on Appendix (C) subsequent to this Report.

5.3. Gravity loads

The vertical load on the piers is the result of a combination of the load applied by the actuators and the self-weight load of the testing rig elements as indicated in Table 5.2 and Table 5.3.

Table 5.2 Gravity load on the Pier 9 by different elements

Loading frame (1)	1842 kg
Vertical actuators (2)	552 kg
Horizontal actuators (½×2)	1097 kg
Load Cell (2)	127 kg
Total	**3618 kg**

Table 5.3 Gravity load on the Pier 11 by different elements

Loading frame (1)	1702 kg
Vertical actuators (2)	552 kg
Horizontal actuators (½×2)	1097 kg
Load Cell (2)	127 kg
Total	**3478 kg**

5.4. Description of the scaled isolation system

The test setup concerniong the isolation mockup is shown in Fig. 5.6. There is a first steel plate fixed at the strong floor of the lab on which are located the first two devices. For these two isolators the sliding surface is pointing upwards. On these two devices is located a second steel plate, linked to the horizontal actuator, that is free to move horizontally along the transverse direction of the bridge. On the top face of this plate are located the other two isolation devices, whose sliding surfaces are pointing downwards. These two devices host another steel plate loaded by the axial load generated by four vertical actuators.

The four vertical actuators are controlled trough a feedback system allowing the steel plates to move horizontally; the above system can also accommodate the vertical displacements of the plates due to sliding of the curved surface of the devices.

A fixed vertical load resulting from the self-weight of the testing rig, load cells and actuators acts on the devices and is computed as follows: middle plate (7.6 kN), top plate (22.6 kN), four vertical actuators (4 x 2.7 = 10.83kN), four load cells related to the vertical jacks (4 x 0.7 = 2.75 kN) and half of the horizontal actuator along with the connecting flange ((7.7+0.6)/2 = 4.5 kN), for a total load of 48.2 kN, about 50 kN considering also the isolators and other small components (bolts, the tubes, etc). For this reason, in the numerical analysis for the calibration of the devices mechanical properties, this value will be accounted for by adding it to the axial load applied through the vertical jacks.

The design mechanic properties of the devices are a curvature radius R equal to 3000 mm and a friction coefficient μ_f equal to 4%. Considering the scale factor S equal to 2.5 employed for the experimental tests, the mockup properties are R and μ_f equal to 1200 mm and 4%, respectively

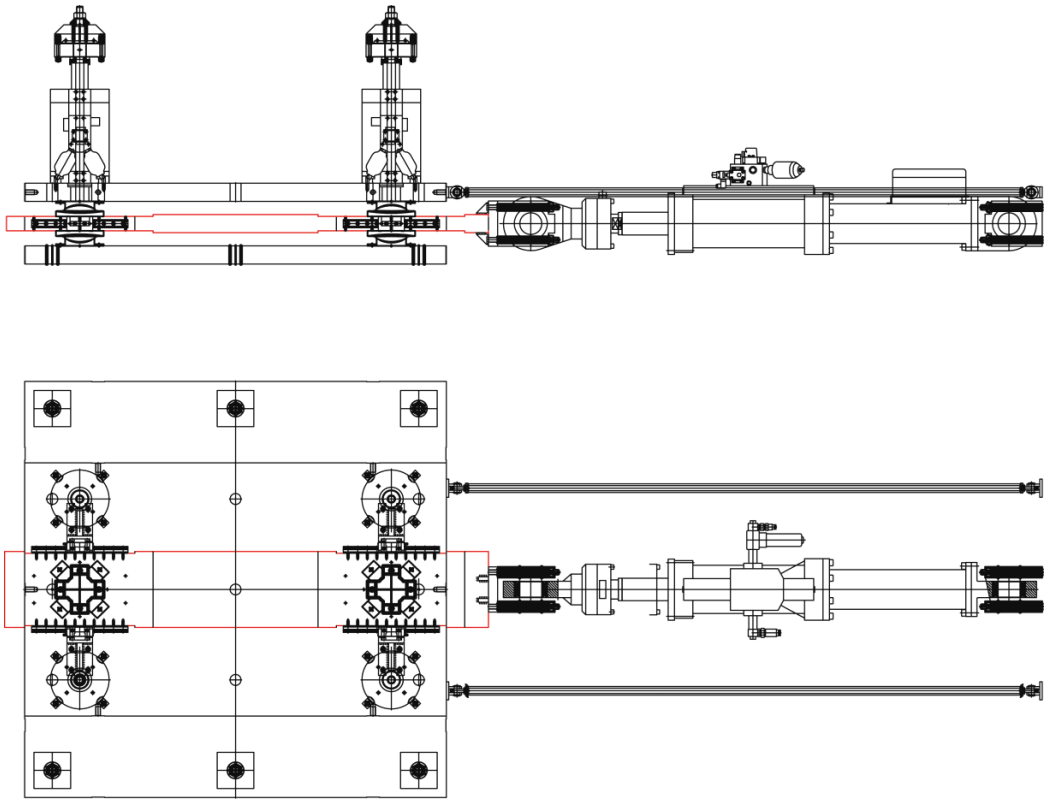

Figure 5.6 Isolation devices test setup

5.5. Mechanical properties of materials

To fully characterize the concrete of the two piers a series of compression tests were performed at JRC using 15×15×15 cm cube specimens. The aggregate design mix of concrete was performed using a maximum aggregate dimension of 3 cm, in order to have short-term properties compatible with the expected behaviour of the piers. The average value of the cubic strength obtained is about 41 MPa and consequently a cylindrical strength of about 34 MPa. This value is in line with the strength value of the concrete used for the construction of the real piers.

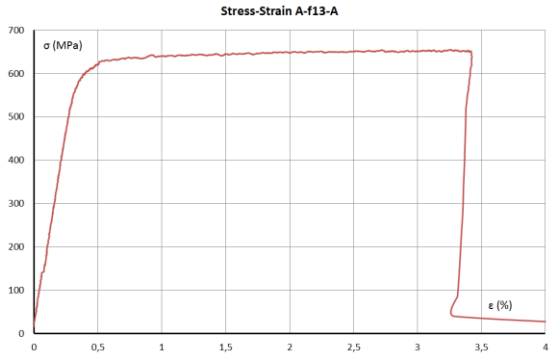

Figure 5.7 Stress-Strain behaviour of test A-fi3-A for plain 3mm steel bar

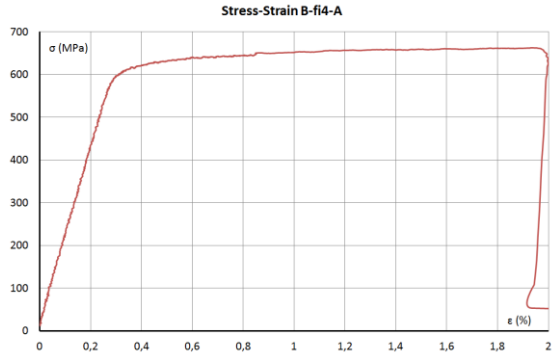

Figure 5.8 Stress-Strain behaviour of test A-fi4-A for plain 4mm steel bar

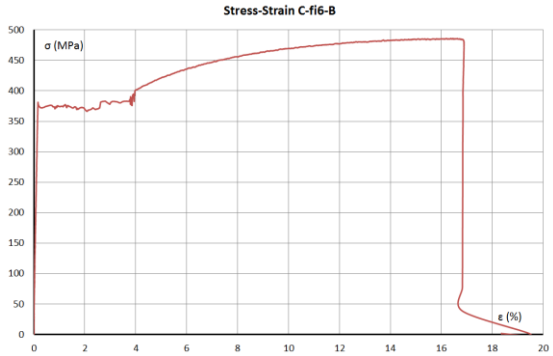

Figure 5.9 Stress-Strain behaviour of test C-fi6-B for plain 6mm steel bar

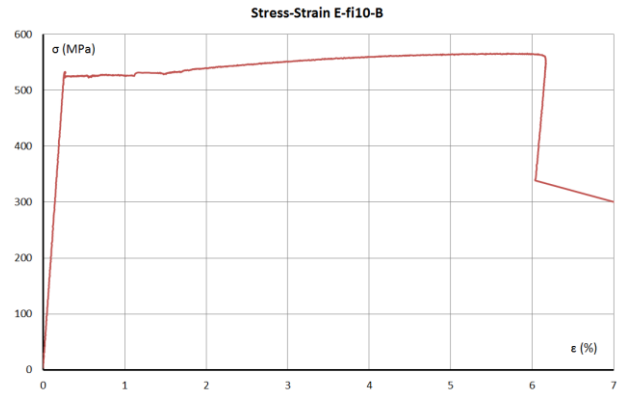

Figure 5.10 Stress-Strain behaviour of test E-fi10-B for plain 10mm steel bar

The class of the steel reinforcement used for the construction is not known. Since at that time AQ42 steel was commonly used in Italy, corresponding to a mean strength of 350 MPa [20], this value was adopted for design strength of the steel bars of the specimens. This consists of smooth rebars of diameter 3, 4, 8 and 10 mm, on which direct tensile tests for the evaluation

of the constitutive law of steel were carried out, obtaining an average value of 350 MPa. Fig. 5.7 through Fig. 5.10 show examples of stress-strain curves.

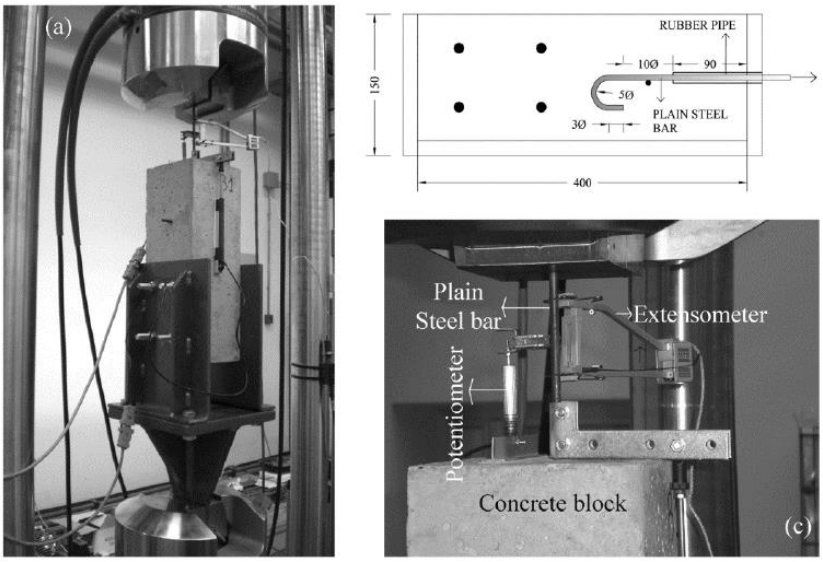

Figure 5.11 Set up of the pull out test

The bond mechanism of straight steel bars and bars with circular hooks was characterized by pull-out tests within an experimental campaign carried out at the University Roma Tre [17]. The tests consist of static displacements applied monotonically to a 10 mm steel bar anchored in a concrete block; a plastic pipe is used to avoid interaction between the rebar and the surrounding concrete except in the embedded zone, equal to 10 diameters of the bar. The force in the bar and the slip between the bar and concrete were continuously measured during the tests using a load cell and a linear potentiometer in conjunction with an extensometer. Fig. 5.11 shows one of the specimens during the preparation phase of the set-up for the pull-out test. Fig 5.12 shows an example of the response for different configurations (only bond, only hook, bond+hook) [17].

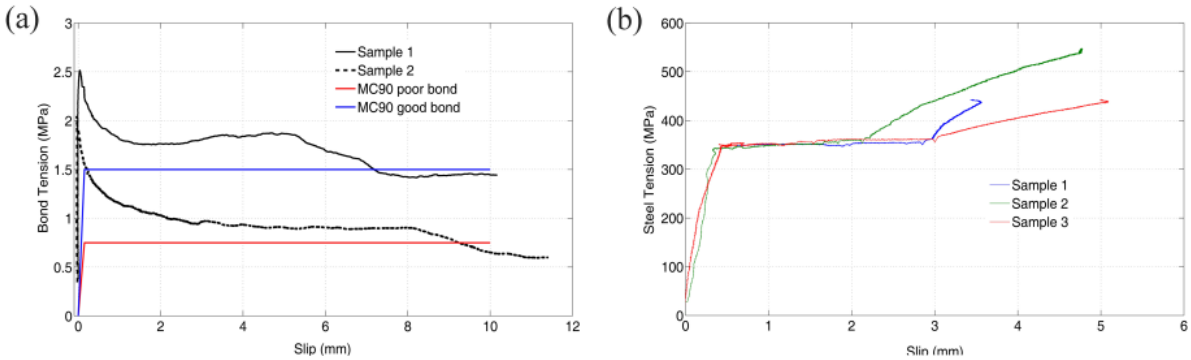

Figure 5.12 Results of the previous experimental campaign at University Roma Tre

6. PsD TEST DESIGN AND SUBSTRUCTURING TECHNIQUE IMPLEMENTATION

6.1. Testing Methods

The Pseudo-Dynamic (PsD) test method combines the numerical time integration of the equations of motion of a structure, properly condensed on a limited number of degrees-of-freedom (DoF), and the experimental measurement of the reaction forces resulting from this motion, applied by means of actuators. This hybrid analytical/experimental character is taken into account when introducing the subtructuring technique [36], allowing to obtain the dynamic response of a structure with only a part, usually the most vulnerable one, present in the laboratory.

The European Laboratory for Structural Assessment (ELSA) laboratory has been involved from some years in the development of the continuous PsD testing method [37], consisting of a PsD test with no hold period that avoids the load relaxation problem and increases the signal/noise ratio, and consequently improving the quality of the results. It allows also a considerable reduction of the test duration and provides much cleaner measurements.

This testing method, which is nowadays the only one used at ELSA, was implemented by means of a synchronous process with a short control period (2ms) and a small time step for the time integration.

Within this framework, it is straightforward to add some DoFs in the process of controlling the structure, providing that the total number of DoFs remains small and the numerical structure elastic. This *monolithic* approach cannot be followed when the number of DoFs increases or when the numerical structure is nonlinear, as for RETRO. In this case *two* processes should be ran in parallel, the first one responsible for the numerical structure and the other one responsible for the motion of the physical structure in the lab, preserving the smooth character of the continuous method. These two process should have *different time steps* (It is virtually impossible to ensure that, within the effective clock duration - 2ms - of one laboratory time step, the analytical process is able to successively perform all the tasks required for advancing its solution, in particular when non-linearities are present) and run *different time integration schemes* (conditional stability of the laboratory explicit central

difference scheme is easy to fulfil, but the numerical structure should use an implicit scheme, to manage the larger time step and the larger number of DoFs).

Starting from the domain decomposition scheme presented in [38], it was shown that it is possible to transform this essentially staggered asynchronous procedure in an inter-field parallel procedure suitable to work with one synchronous process, keeping most of the original characteristics of the scheme [39]. The non-linear case was also investigated and a combination of a non-iterative Operator Splitting strategy [40] [41], and of a non-linear condensation technique was proposed to handle the analytical structure [42]. This distributed scheme, including experimental results obtained in 2005 when testing an isolator. is described in detail in [43] and [44].

For the RETRO project, the research implementation performed for the validation tests of 2005 was insufficient. RETRO includes a much larger specimen, some of them (the piers) accumulating damage in an irreversible way. It was thus needed to substantially upgrade the substructuring implementation of 2005, in order to have during the tests the same standards for error and alarm management, the same input (plus the additional requested information specific of substructuring), the same output definition (adding few substructuring related variables) as what is the current state-of-the art in continuous PsD testing at ELSA.

As with all substructured tests performed in the past at ELSA, the software used for the numerical part is Cast3M [45], a multi-purpose finite element code which was also slightly modified in order to introduce the non-linear models used during the tests.

6.2. Numerical Modelling

6.2.1. Development of a refined model of the bridge in Opensees

In what follows a refined numerical model developed in OpenSees is described. Details on the constitutive laws of the used materials are provided together with model assumptions like finite element types, restraint and boundary conditions, modelling and position of the masses, etc. In this model the main non-linear phenomena (flexural behaviour of columns and beams, strain penetration, shear deformation, P-Delta effect, etc.) are included.

6.2.1.1. Description of the main non-linear phenomena of the Rio Torto viaduct

A preliminary investigation aiming at studying the cyclic behaviour of the piers was carried out both numerically and experimentally. A test campaign, performed at the structural

laboratory of University Roma Tre, consists of quasi-static cyclic displacements imposed to three 1:4 scale specimens of pier 12. Details on the experimental results can be found in [17]. The results confirmed that the response of the pier is highly affected by the behaviour of local details, such as non-linear shear deformability of the transverse beam or strain-penetration of the plain steel bars. In Fig. 6.1a the numerical and experimental cyclic force-deflection responses of pier 12 are shown, whereas in Fig. 6.1b the experimental shear crack pattern of the transverse beam is shown.

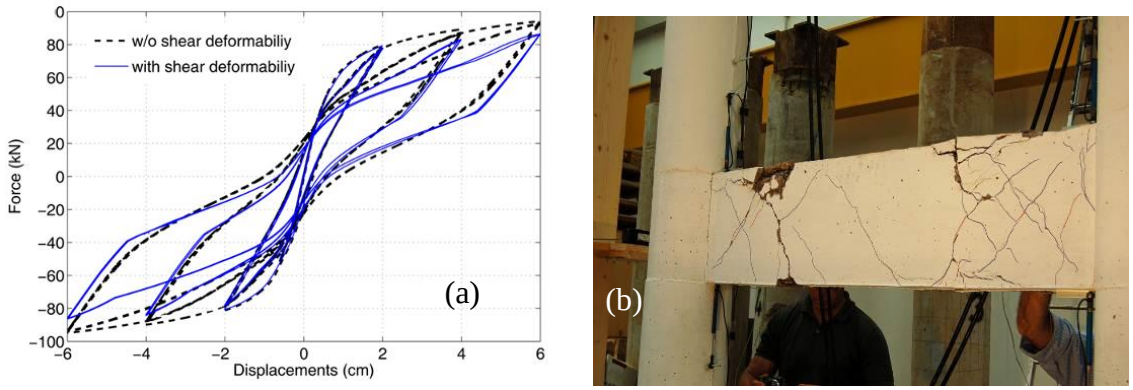

Figure 6.1 Experimental investigation at University Roma Tre: (a) Force-deflection cycle of pier 12, (b) Shear Damage in the transverse beam of pier 12

6.2.1.2. Implementation of the OpenSees F.E. model: "As Built" viaduct

The model was created for one lane of the bridge with full scale dimensions (Fig. 6.2).

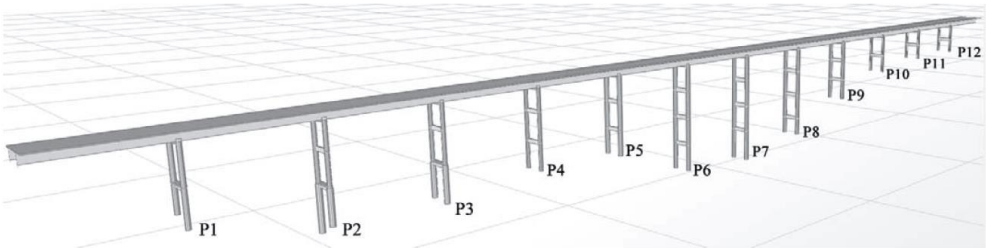

Figure 6.2 RIO-TORTO viaduct - Opensees

The model is composed by fibre beam elements reproducing the location of the reinforcing bars into the sections of beam and columns of the piers. For example, the finite element scheme of pier 12 is illustrated in Fig. 6.3

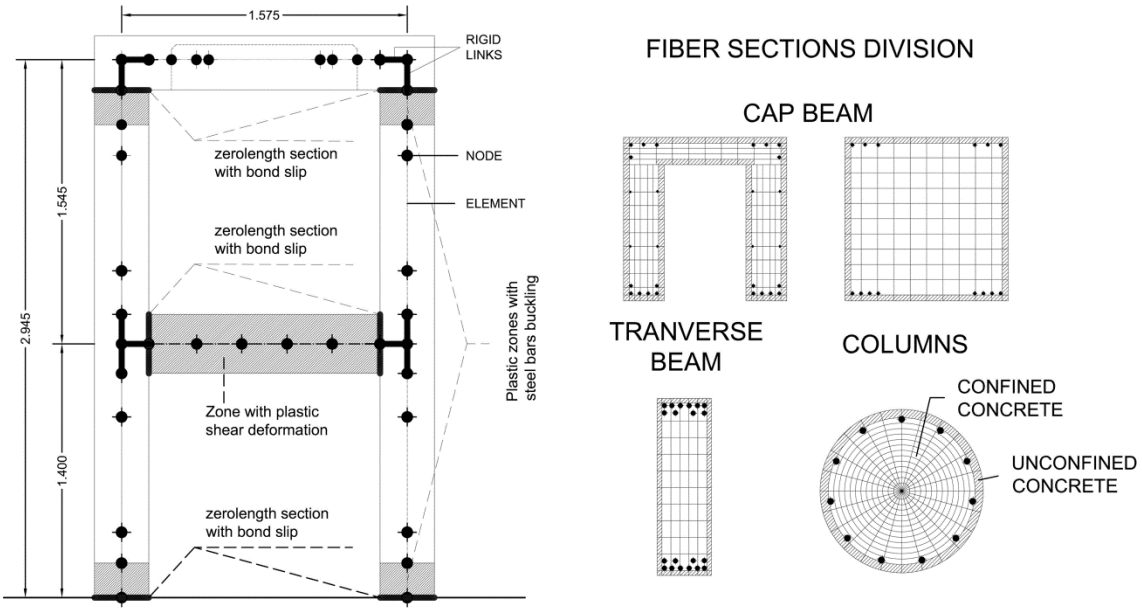

Figure 6.3 Numerical model of pier 12

The structural elements are modelled by nonlinear beam elements with flexibility formulation. All degrees of freedom are fixed at the base of the finite element model.

The section of each element is subdivided into fibres so that it is possible to assign for each material the constitutive law and the exact location and dimension of the reinforcing bars. The cross sections are also indicated in Fig. 6.3. The Kent-Scott-Park model is adopted for the stress-strain behaviour of concrete. This constitutive law has a first parabolic branch up to the peak compression stress equal to 26 MPa at a corresponding strain equal to 0.25%, and a decreasing linear branch to 22 MPa at a corresponding strain of 0.6%. According to the results reported in the literature, especially from experimental tests, the contribution of concrete tensile strength in modelling structures with plain steel bars and poor seismic details can be neglected [16].

The reinforcing steel bars are modelled according to the Menegotto-Pinto constitutive law. A yield stress equal to 360 MPa is assumed here, along with a modulus of elasticity equal to 205,000 MPa and a hardening parameter equal to 0.025. The transition parameters from elastic to plastic behaviour are chosen according to [46].

For assigning the mass along the deck, each span of the bridge was divided into 5 parts (with length ranging from 5.81 to 6.60 m), resulting in translational masses defined for each of these parts along the longitudinal, transverse and vertical directions (m_x, m_y *and* m_z). The effect of the rotational mass was neglected (Fig.6.4 and Fig. 6.5).

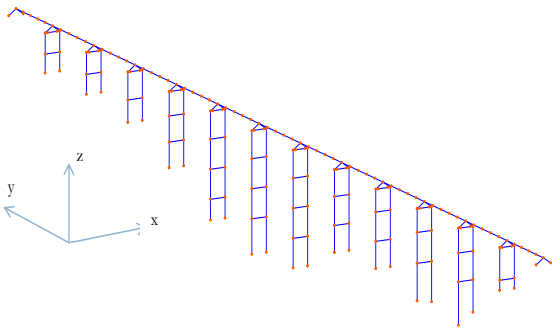

Figure 6.4 FEM Opensees model

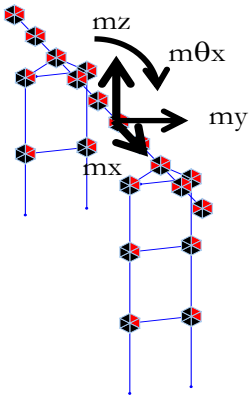

Figure 6.5 Mass placement

For the piers, the mass was calculated and assigned to the joints of the model considering the tributary contributions of members (columns, transverse beams, cap beam) for the longitudinal and transversal directions.

Concerning the Gerber saddles, the saddles were modelled as hinges, thus with the possibility of transferring shear in longitudinal and transversal direction. The reasons of this choice are several:

a) It is difficult to believe that in the transversal direction free movement of the saddles can be considered, at least under an equilibrium point of view of the piece between two saddle.
b) The viaduct has a slight curvature; this can induce the transmission of shear forces in the transversal direction due to rotation in the vertical direction of adjacent parts of the deck that can induce pounding.
c) The presence of saddles in the longitudinal direction would suggest the use of a gap element. This means that the four parts, in which the viaduct can be divided, would behave independently from each other. Thus the hypothesis of considering hinges is certainly more conservative.

6.2.1.3. Restraints and boundary conditions

The supports of the piers were considered as fully fixed in all directions while the abutments on both sides of the bridge were assumed to be simple supported in the longitudinal direction (global y), but restrained in the x and z directions (Fig. 6.6, Fig. 6.7 and Fig. 6.8).

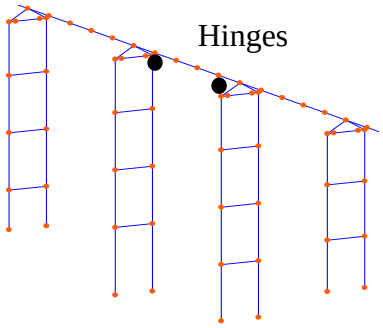

Figure 6.6 Hinge model for the Gerber saddles

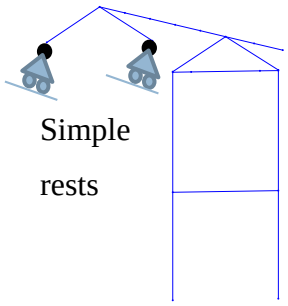

Figure 6.7 Restraint conditions between deck and abutment

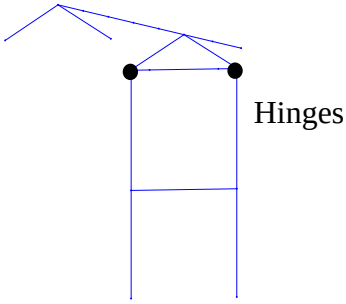

Figure 6.8 Restraint conditions between deck and abutment

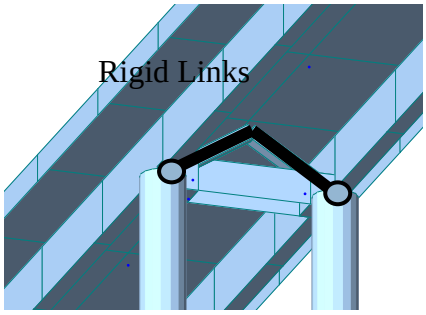

Figure 6.9 Rigid beams connecting the deck to the piers

As for connecting the deck to the piers, two rigid beams of infinite stiffness were created from the centre of mass of the deck to the top of the piers (Fig. 6.9).

6.2.1.4. Strain penetration effect of the plain steel bars

An important aspect to consider is the bond-slip effect in proximity to the bottom and top of the columns. This phenomenon is due to the difference between the deformation of the bars and concrete which yields a typical crack pattern (Fig. 6.10). In literature, the bond-slip problem and its contribution to the lateral flexibility of structures for horizontal forces has been widely investigated. It is worth pointing out that this effect may be pronounced for plain bars due to the low bond between concrete and steel. Following the approach proposed by

Zhao and Sritharan [47], one way to account for the bond-slip effect consists of concentrating the rotation due to the slippage of the bars in a section.

Figure 6.10 Crack opening for bar slippage

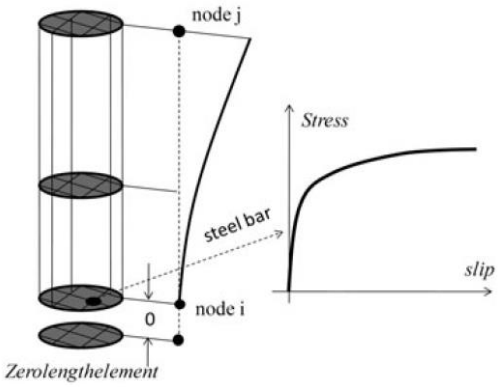

Figure 6.11 Zhao e Shritaran model

This may be done in OpenSEES by using a fibre zeroLengthSection element, for which a unit length is assumed. This implies that element deformations correspond to section deformations and then the moment-curvature is equivalent to the moment-rotation relationship. In this way, the rotation due to bond slip effect may be accounted for by defining a proper stress-slip relationship for steel, describing the interaction between concrete and the steel bar (Fig. 6.11). It was used to model the sections at the top and bottom of the columns and the end sections of the transverse beam. The bond-slip parameters are chosen according to experimental results of pull-out tests as previously described. In particular the value of slip sy, corresponding to the yielding of the bars, is equal to 0.5 mm, whereas the ultimate slip su was assumed equal to 40×sy.

Depending on the anchorage detail and the corresponding slippage mechanism, it is possible for steel bars with sufficient anchorage length to exhibit pinching in the hysteretic behaviour. For this reason the cyclic behaviour associated with the strain-penetration effect modelled by Zhao and Sritharan contains a coefficient Rc that permits the pinching characteristic to be accounted for in the analytical simulation of flexural members. The value adopted here for Rc is 0.5.

6.2.1.5. Modelling of non-linear shear behaviour

In order to calibrate the numerical model of the pier, a shear model of the transverse beam must be implemented. It is well known that shear response plays an important role especially

for existing structures that do not meet seismic engineering design criteria. In literature, several studies concerning the shear behaviour of reinforced concrete beams or walls and their interaction with flexural response are reported and compared with experimental results [48] [49].

Considering these formulations and the relatively scarce information about experimental results for shear behaviour in the presence of plain longitudinal bars, a phenomenological shear-strain hysteretic relationship for shear behaviour of the transverse beam was assumed. It consists of a tri-linear envelope curve with stiffness and strength degradation with pinching response which is always observable in reinforced concrete elements subjected to shear forces. The model is similar to the one proposed in [50] and [51], except for both the influence of axial force on the shear relationship, here neglected, and the use of a tri-linear backbone curve.

The force-deformation relationship for shear is implemented by using the OpenSEES command "Section Aggregator", which groups the behaviour of different materials into a single section force-deformation model; in this way, the shear and flexural behaviour are linked by means of equilibrium equations, even though their mechanical formulations are uncoupled.

In this case, a uniaxial material is chosen to represent the sectional shear behaviour. It is defined through three points of the envelope curve (Fig. 6.12).

The first point (A), corresponding to the onset of shear cracking, was evaluated experimentally for pier 12; it is characterized by a shear deformation γ_a equal to 3.5×10^{-4} and a shear strength V_a equal to 200 kN. The second point (B) was partially evaluated using the experimental data of pier 12. In particular, the force V_b equal to 900 kN was obtained with the formula proposed by Priestly et al. [52], and confirmed using the software Response 2000 [53], based on the Modified Compression Field theory [54]. The shear deformation γ_b equal to 1.0×10^{-3} was indeed obtained from the experimental data of pier 12, as already explained. The third point (C) has ordinate $V_c=V_b$ and shear deformation equal to $\gamma_c=10\cdot\gamma_b$, which implies that the overall shear force remains constant for the last cycles. For comparison, the shear strength V_b was also evaluated using the formula of Eurocode 8 part 3 [6], regarding the assessment and retrofitting of existing buildings, which depends on several parameters, among them the level of flexural ductility μ. Because the experimental results have shown for all the piers a very limited flexural damage, a ductility $\mu=1$ was considered reasonable. The corresponding strength V_b is about 900 kN.

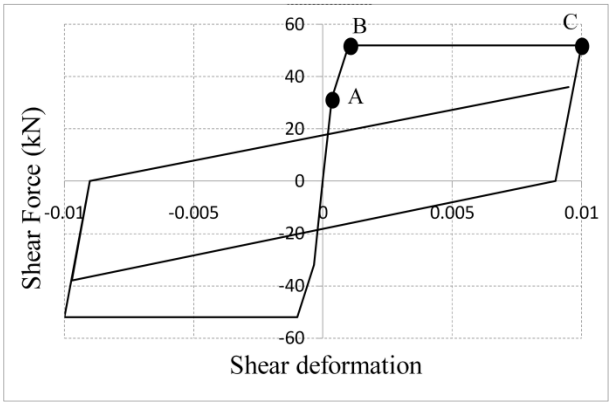

Figure 6.12 Shear force-deformation relationships

In order to account for the hysteresis phenomenon in the shear force-deformation relationship, a hysteresis law was used, characterized by several parameters which modify pinching and stiffness, namely the damage level as function of the ductility level, the damage related to the dissipated energy and the unloading stiffness as function of ductility [55].

6.2.1.6. OpenSees F.E. model: "Isolated" viaduct

The 3D model was developed to simulate accurately the seismic response of the Rio Torto bridge. The numerical model is similar to the FE system used for the non-isolated case: joints and elements labelling, modelling of the piers (considering all the nonlinear sources, i.e shear behaviour and fix-end rotation), deck represented as elastic beam, piers fixed to the base and end supports assumptions. Two differences were, however, included for the base isolated system: the Gerber-saddle was removed (i.e. a continuous beam was obtained) and isolation devices between the piers and the deck were introduced to represent the seismic retrofitting scheme. The use of base isolators for the bridge deck increased the number of vertical coordinates of the deck joints.

6.2.1.7. Implementation of isolators in the non-linear model

The FP devices used to seismically isolate the bridge deck of the Rio Torto were modelled in the computer program Opensees. The command used to simulate numerically the response of the FP is a "singleFPBearing" element object [56], which is defined by two nodes. The i-Node represents the concave sliding surface and the j-Node represents the articulated slider. The element can have zero length or the appropriate bearing height. The bearing has unidirectional (2D) or coupled (3D) friction properties (with post-yield stiffening due to the

concave sliding surface) for the shear deformations, and force-deformation behaviours defined by Uniaxial Materials in the remaining two (2D) or four (3D) directions. To capture the uplift behaviour of the bearing, the user-specified Uniaxial Material in the axial direction was modified for no-tension behaviour. By default P-Delta moments are entirely transferred to the concave sliding surface (i-Node). It is important to note that rotations of the concave sliding surface (rotations at the i-Node) affect the shear behaviour of the bearing. To avoid the introduction of artificial viscous damping in the isolation system (sometimes referred to as "damping leakage in the isolation system"), the bearing element does not contribute to the Rayleigh damping. If the element has non-zero length, as in this case, the local x-axis is determined from the nodal geometry unless the optional x-axis vector is specified in which case the nodal geometry is ignored and the user-defined orientation is utilized.

The mechanical properties used to define single FP Bearings in Opensees are the type of friction material, the curvature radius and the height of the device. The Coulomb approach was used for the simulation of the devices for the Rio Torto bridge; thus kinetic friction is independent of the sliding velocity, in compliance with Coulomb's law. The latter assumption is compliant with the PSD test procedure.

6.2.2. Reduced Model in Opensees

6.2.2.1 Model description

In order to provide stiffness and mass matrices for model reduction, a further 832-DoFs ANSYS Reference Model of the Bridge (RM) was implemented for the non-isolated case. Same constraint conditions, material properties and equivalent viscous damping of 5% of the OpenSEES RM were considered. Modes 2 and 4, depicted in Fig. 6.13, carry most of the modal mass in the direction of the earthquake excitation.

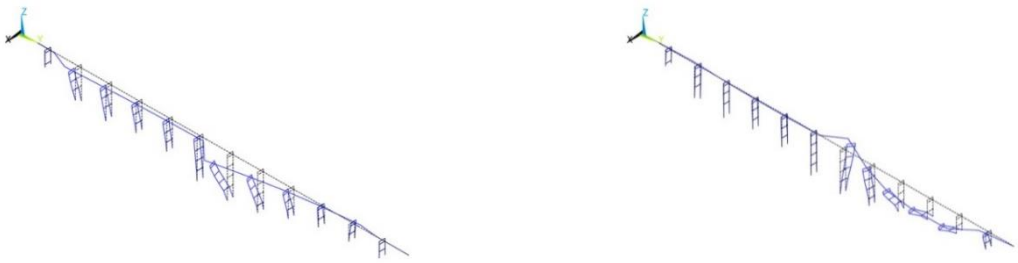

(a) 2nd eigenmode at 0.64 Hz **(b) 4th eigenmode at 1.10Hz**

Figure 6.13 ANSYS FE model of the Rio Torto viaduct

The seismic load excites the lowest global eigenmodes of the viaduct, which essentially displace the piers along the *y* transversal direction. Displacements of piers along the longitudinal direction of the bridge were negligible. As a result, an ANSYS Simplified Model of the Bridge (SM) embedding a simplified constraint setting was set; in particular, relative rotations between the deck and piers were released, whilst out-of-plane displacements of the piers were fixed. The first four eigenfrequencies of ANSYS RM, ANSYS SM and OpenSEES RM are reported in Table 6.1.

The ANSYS RM model agreed well with the OpenSEES RM. Deformed shapes of the same eigenmodes confirm the good matching between the OpenSEES RM and the ANSYS RM, at least in the linear range.

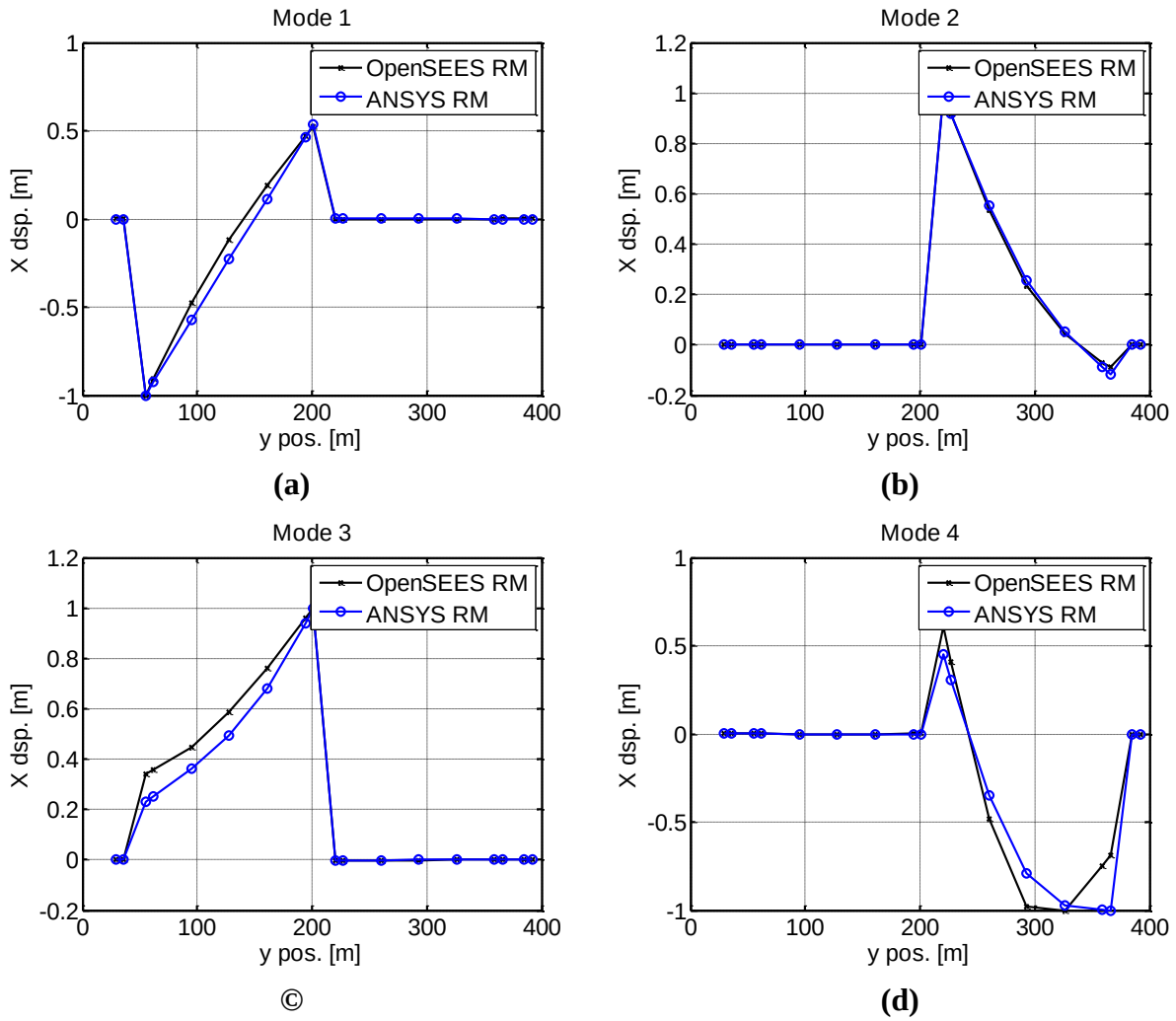

Figure 6.14 Plan views of Eigenmodes: a) mode 1, b) mode 2, c) mode 3 and d) mode 4 of the OpenSEES RM and ANSYS RM models

Table 6.1.Comparisons of eigenfrequencies among all bridge models.

Mode	OpenSEES RM [Hz]	ANSYS RM [Hz]	ANSYS SM [Hz]
1	0.6137	0.6254	0.6227
2	0.6432	0.6452	0.6433
3	0.6576	0.7017	0.7004
4	1.1383	1.1023	1.1007

As can be appreciated in Fig. 6.14, Gerber saddles split the deformed shapes of the deck. Modes 1 and 3 affect the left side of the deck, whilst Modes 2 and 4 affect the right side.

6.2.2.2 Model Reduction of Numerical Piers

Since the higher modes of the piers were not excited, the static Guyan reduction [57] was applied to obtain single DoF (S-DoF) reduced piers. Each translational interface DoF between the pier and the deck was retained, whilst the remaining ones were discarded. According to the relevant formulation, the static condensation reads:

$$\mathbf{u} = \begin{bmatrix} \mathbf{u}_R \\ \mathbf{u}_L \end{bmatrix} = \begin{bmatrix} \mathbf{I} \\ \mathbf{\Phi}_R \end{bmatrix} \cdot \mathbf{u}_R = \mathbf{T} \cdot \mathbf{u}_R \tag{6.1}$$

where, $\mathbf{u}_R$ and $\mathbf{u}_L$ are the retained and deleted DoFs, respectively, whilst matrix $\boldsymbol{\phi}_R$ collects constraint mode vectors projected on deleted DoFs, according to the Guyan formulation (Guyan, 1965). Linear parameters of reduced S-DoF piers were obtained as follows:

$$k = \mathbf{T}^T \mathbf{K} \mathbf{T}, m = \mathbf{T}^T \mathbf{M} \mathbf{T}, f = \mathbf{T}^T \mathbf{M} \mathbf{L} \tag{6.2}$$

where, $\mathbf{K}$, $\mathbf{M}$ and $\mathbf{L}$ are the stiffness, the mass and the Boolean lead matrices characterizing each single pier. The Craig-Bampton reduction method [58] is the natural extension of the proposed approach when local modes of piers are not negligible. Table 6.2 summarizes linear parameters of reduced S-DoF piers.

According to [17] most of the damage is concentrated within piers during a seismic event. Proposed reduced S-DoF piers lent themselves to an easy extension to the nonlinear range. More precisely, modified Bouc-Wen springs capable of reproducing the typical hysteretic

energy dissipation of piers were devised. Linear parameters of S-DoF reduced piers were assumed as basis. The resulting nonlinear model reads:

Table 6.2. Linear parameters of S-DoF reduced piers.

Pier	Stiffness *k* [N/m]	Mass *m* [kg]	Load *f* [kg]
1	3,22E+07	3,51E+04	4,50E+04
2	9,93E+06	7,53E+04	1,04E+05
3	8,83E+06	8,04E+04	1,09E+05
4	1,19E+07	6,72E+04	9,06E+04
5	1,84E+07	6,96E+04	9,69E+04
6	9,47E+06	9,29E+04	1,33E+05
7	8,43E+06	9,90E+04	1,41E+05
8	1,12E+07	8,52E+04	1,22E+05
9	2,36E+07	6,30E+04	8,84E+04
10	2,29E+07	4,26E+04	5,64E+04
11	3,81E+07	3,90E+04	5,07E+04
12	4,27E+07	3,71E+04	4,84E+04

$$m\ddot{x} + c\dot{x} + r = -f \cdot a_g(t) \tag{6.3}$$

$$\dot{r} = \left[\frac{\rho \cdot A}{\left(1 + \alpha \cdot x^2\right)} - (\beta \cdot \mathrm{sgn}(\dot{x} \cdot r) + \gamma) \,|\, r \,|^n \right] \cdot \dot{x} \tag{6.4}$$

where *A*, β, γ and *n* are parameters of the Bouc-Wen model. *A* was assumed equal to the linear stiffness element of the S-DoF reduced pier, whilst ρ was introduced to represent its average degradation. In order to decrease the number of tuning parameters, γ was set to zero and *n* to one. The softening factor α was introduced according to the material properties of the OpenSEES RM. With regards to the nonlinear identification of parameters, each substructured pier was considered as a stand-alone SISO system. Interface forces recorded from OpenSEES RM time history analyses were considered as input applied to the coupling DoF of the substructured pier, whilst cap beam level displacements were considered as output. A penalty function was defined as the Normalized Root Mean Square Error (NRMSE)

between the displacement response of the reduced pier and the displacement response calculated on the OpenSEES RM.

$$\left\{\hat{\rho},\hat{\alpha},\hat{\beta}\right\} = \min_{\rho,\alpha,\beta} NRMSE\left(\mathbf{x}_{ref},\mathbf{x}_{red}\left(\rho,\alpha,\beta\right)\right) = \frac{\sqrt{\sum_{i=1}^{n}\frac{\left(x_{ref,i}-x_{red,i}\left(\rho,\alpha,\beta\right)\right)^2}{n}}}{\max\left(\mathbf{x}_{ref}\right)-\min\left(\mathbf{x}_{ref}\right)} \tag{6.5}$$

where:

- $\mathbf{x}_{\mathrm{red}}$: displacement response history of a generic reduced pier;
- $\mathbf{x}_{\mathrm{ref}}$: displacement response history of a generic pier from the OpenSEES RM;
- n: length in sample of displacement response histories.

The MATLAB pattern search algorithm was employed to minimize the penalty function. Table 6.3 summarizes identified parameters for both the SLS and ULS, respectively.

Table 6.3 Identified parameters of reduced piers for both SLS and ULS.

Pier	SLS			ULS		
	ρ	α [1/m2]	β [1/m]	ρ	α [1/m2]	β [1/m]
1	1,00	1987,15	0,00	0,83	1942,26	0,10
2	0,67	32,50	1,17	0,50	0,19	2,13
3	0,81	108,82	1,32	0,96	215,65	2,19
4	0,66	125,55	2,51	0,50	24,98	3,93
5	0,63	248,94	1,90	0,68	338,44	0,60
6	0,79	161,51	1,25	0,50	8,66	1,44
7	0,50	7,94	1,05	0,50	8,34	1,94
8	0,59	44,75	0,58	0,50	29,30	1,25
9	0,73	338,32	0,84	0,95	1005,93	0,36
10	1,00	1151,93	0,00	0,59	387,69	1,58
11	0,79	919,21	1,84	0,50	490,84	1,31
12	0,99	1997,13	0,01	0,72	1090,46	3,10

It is interesting to note that appreciable stiffness degradation occurs at ULS. With reference to Pier 9, Fig. 6.15 compares transversal displacement responses of reduced models to relevant OpenSEES solutions at both limit states.

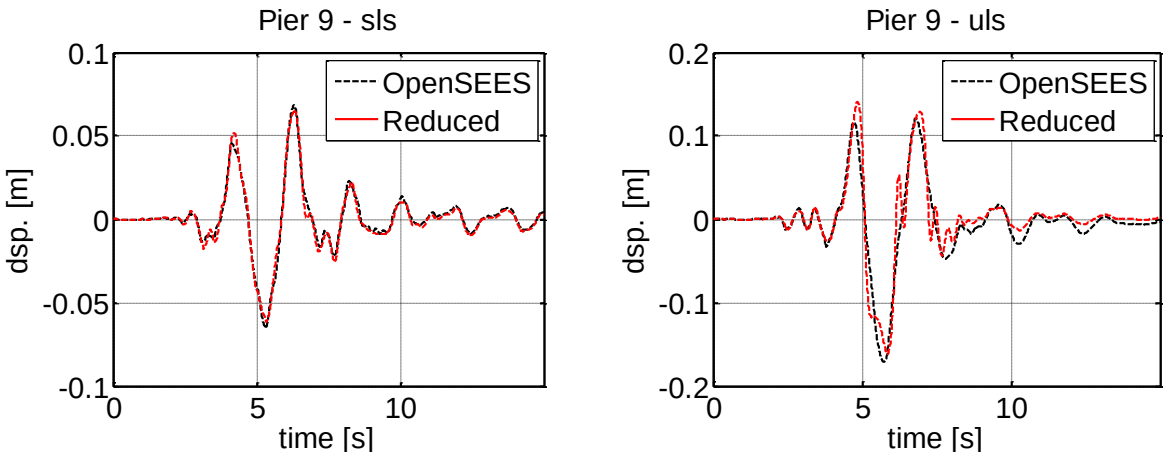

(a) Displacements **(b) Dissipated energy histories at ULS**

Figure 6.15 Validation of the reduced model of Pier 9

6.2.2.3 Model Reduction of Numerical Isolation Devices

The hysteretic model of nonlinear friction pendulum isolators employed in the isolated case, shown in Figure 6.16 (a), was based on the bilinear model proposed by Mostaghel [59]; see Fig.6.16 (b) and Fig. 6.16 (c) in this respect. The aforementioned bilinear model was used to reproduce the nonlinear behaviour of the two-node single FP Bearing element implemented in the OpenSEES RM.

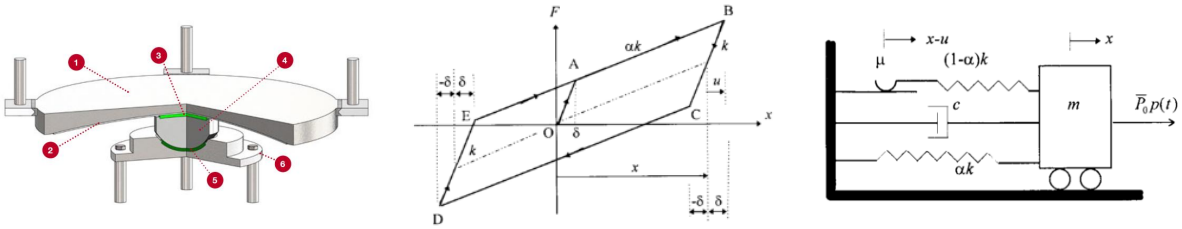

(a) **(b)** **©**

Figure 6.16 a) Sliding surface spherical bearing device (courtesy of ALGA Spa); b) Hysteretic loop for the bilinear system after Mostaghel (Mostaghel, 1999); c) bilinear S-DoF system

The slip behaviour of the element was considered by means of the state space variable *u*. The system of differential equations governing the behaviour of the bilinear system depicted in Fig. 6.16 (b) reads:

$$\begin{cases} m\cdot\ddot{x}+c\cdot\dot{x}+\alpha kx+(1-\alpha)ku=\bar{P}_0\cdot p(t) \\ \dot{u}=\dot{x}\left(\bar{N}(\dot{x})\bar{M}(u-\delta)+M(\dot{x})N(u+\delta)\right) \end{cases} \tag{6.6}$$

Where $N, M, \bar{N}$ and $\bar{M}$ are defined as polynomials of the *sign* function. The integration of the system defined in Eq. (6.6) entails the response of any non-degenerating hysteretic bilinear system under a given load. In the present case, no mass and damping contributions of isolators were considered. Parameters were deduced from the solution of the following optimization problem:

$$\left\{\hat{\alpha},\hat{k},\hat{\delta}\right\}=\min_{\alpha,k,\delta} NRMSE\left(\mathbf{r}_{ref},\mathbf{r}_{red}(\alpha,k,\delta)\right) \tag{6.7}$$

$$\begin{cases} r_{red,i}=\alpha\cdot k\cdot x_{ref,i}+(1-\alpha)\cdot k\cdot u_i \\ u_i=\sum_{j=1}^{i}\dot{x}_{ref,j}\left[\begin{array}{l}\bar{N}(\dot{x}_{ref,j})\bar{M}(u_j-\delta)+\ldots \\ \quad M(\dot{x}_{ref,j})N(u_j+\delta)\end{array}\right]dt \end{cases} \tag{6.8}$$

where:

- $\mathbf{r}_{red}$: is the restoring force history from the simplified bilinear model;
- $\mathbf{r}_{ref}$: is the restoring force history from theOpenSEESRM;
- $\mathbf{x}_{ref}$: is the relative displacement history from the OpenSEES RM;
- $\dot{\mathbf{x}}_{ref}$: is the relative velocity history from the OpenSEES RM.

The same NRMSE defined in Eq. (6.5) was considered. Identified parameters are:

$$\hat{k}=2.03e8\ \ N/m \qquad \hat{\alpha}=0.0046 \qquad \hat{\delta}=0.00050\ m$$

Fig. 6.17 compares the hysteretic loop and the dissipated energy history of one of the OpenSEES isolator pair installed on Pier 9 to its reduced counterpart at ULS.

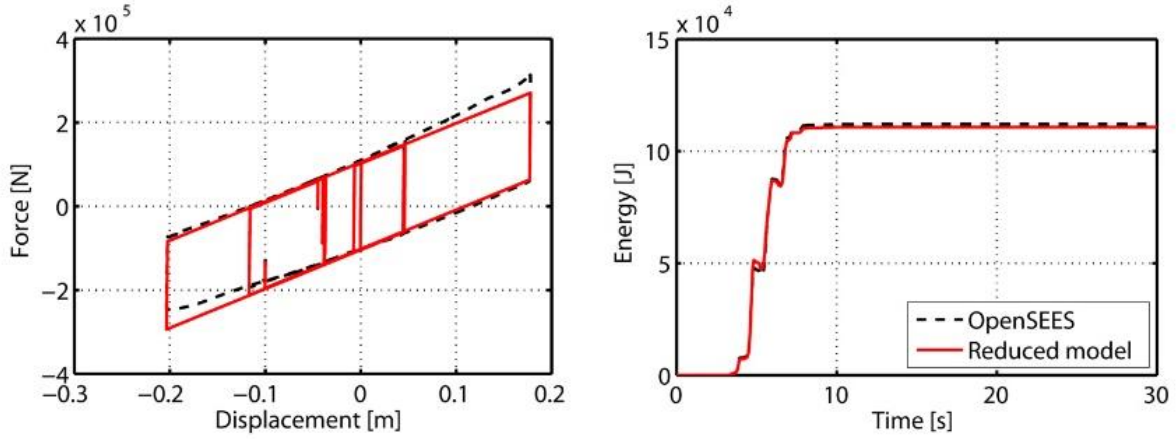

(a) **(b)**

Figure 6.17 Dynamic response of right isolator of Pier 9 at ULS: a) Hysteretic loop; b) dissipated energy

A similar matching level was achieved for all piers. Although the effect of a variable vertical loading was neglected, simplified bilinear models well reproduced the complex behaviour of OpenSEES isolator elements.

6.2.2.4 Numerical Validation of the reduced model of the non-isolated bridge

The reduced model of the non-isolated bridge was implemented by assembling substructured piers and the deck. Fig. 6.18 shows the reduced model of the non-isolated bridge provided with nonlinear S-DoF piers and node numbering enabled.

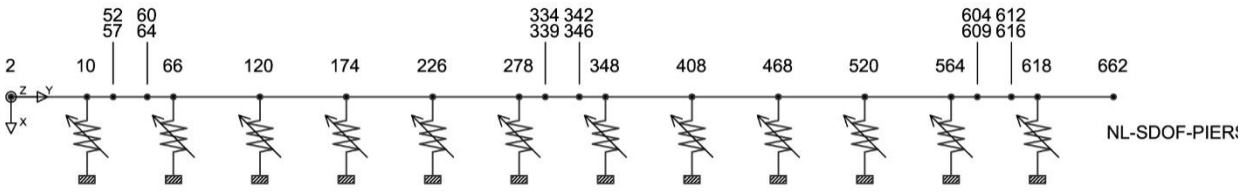

Figure 6.18 Plan view of the reduced model of the bridge in the non-isolated case

Deck matrices were derived from ANSYS and based on BEAM44 elements; nonlinear S-DoF piers acted as transversal springs. The external constraints are given in Table 6.4a.

Three Gerber saddles connect the two sides of the deck. They were implemented by means of the Constraint Equations (CEs) shown in Table 6.4b.

The resulting 88 DoFs model of the non-isolated bridge was validated though nonlinear time history analyses with foreseen seismic accelerograms. All simulations were conducted applying the Newmark time integration method [60]. With respect to the OpenSEES RM,

Table 6.5 summarizes NRMSEs on transversal kinematic quantities, i.e. displacements, velocities and accelerations, recorded at the top of each pier in the non-isolated case.

Table 6.4a Constraint equations for beams and columns

Node selection	Constraint setting
2,662	Ux,Uy,Uz,Roty = 0
10,66,120,174,226,278,348,408,468,520,564,618	Uy,Uz,Roty = 0

Table 6.4b Constraint equations for the Gerber saddles

Node selection	Coupled DoFs
52,57	Ux,Uy,Uz,Roty
60,64	Ux,Uy,Uz,Roty
334,339	Ux,Uy,Uz,Roty
342,346	Ux,Uy,Uz,Roty
604,609	Ux,Uy,Uz,Roty
612,616	Ux,Uy,Uz,Roty

As can be appreciated in Table 6.5, the displacement, velocity and acceleration responses of the reduced model match reasonably well the response of the OpenSEES RM. Fig. 6.19 compares the cap beam level transversal displacement responses of Pier 9 of the reduced model and the OpenSEES RM at both limit states.

Table 6.5 NRMSE values on kinematic quantities for the non-isolated case

Pier	SLS			ULS		
	Disp. [m]	Vel. [m/s]	Acc. [m/s2]	Disp. [m]	Vel. [m/s]	Acc. [m/s2]
1	0,04	0,03	0,02	0,07	0,06	0,07
2	0,06	0,07	0,04	0,06	0,04	0,03
3	0,05	0,05	0,03	0,05	0,04	0,03
4	0,04	0,04	0,02	0,04	0,03	0,03
5	0,03	0,03	0,02	0,04	0,03	0,02
6	0,04	0,04	0,02	0,04	0,04	0,03
7	0,05	0,05	0,03	0,05	0,03	0,04
8	0,05	0,05	0,03	0,04	0,04	0,03
9	0,05	0,05	0,02	0,05	0,07	0,05
10	0,04	0,03	0,02	0,08	0,09	0,07
11	0,03	0,03	0,02	0,09	0,09	0,09
12	0,02	0,02	0,02	0,05	0,04	0,04

In conclusion, the proposed reduced model of the bridge agrees with the OpenSEES RM at both limit states.

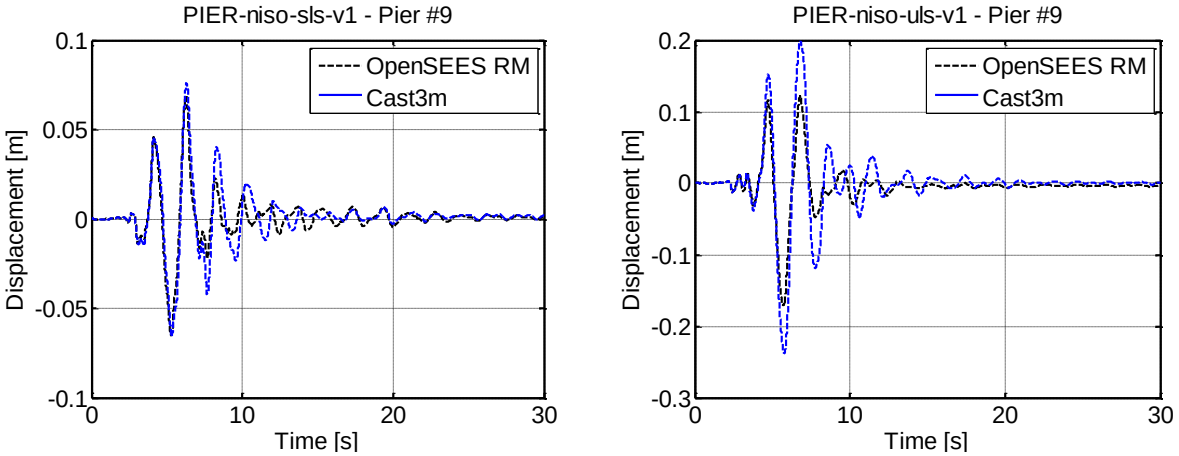

Figure 6.19 Cap beam level transversal displacement responses of Pier 9 in the non-isolated case at a) SLS; b) ULS

6.2.2.5 Numerical Validation of the model of the isolated bridge

The same reduced model of the non-isolated bridge was provided with reduced nonlinear isolators. This model was implemented for tests with isolators. Figure 6.20 shows the plan view of the model of the isolated bridge with node numbering enabled.

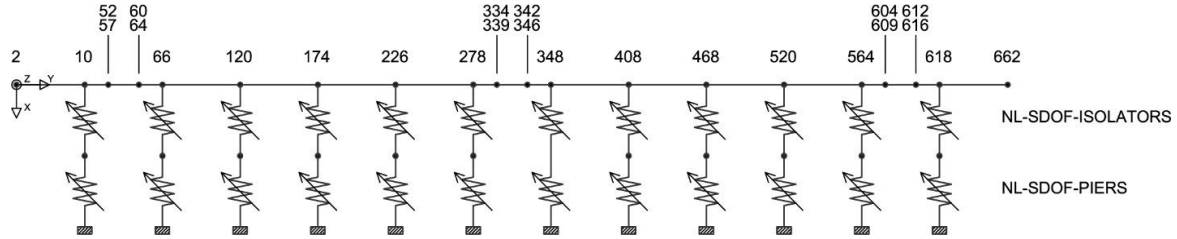

Figure 6.20 Plan view of the reduced model of the bridge in the isolated case

Same external constraints of the non-isolated bridge hold. Nonetheless, Gerber saddles were removed. Accordingly, the internal constraint setting changed. The CEs of the isolated bridge are shown in Table 6.4c.

Table 6.4c Internal constraints for the isolated bridge

Node selection	CoupledDoFs
52,57	Ux,Uy,Uz,Rotx,Roty,Rotz
60,64	Ux,Uy,Uz,Rotx,Roty,Rotz
334,339	Ux,Uy,Uz,Rotx,Roty,Rotz
342,346	Ux,Uy,Uz,Rotx,Roty,Rotz
604,609	Ux,Uy,Uz,Rotx,Roty,Rotz
612,616	Ux,Uy,Uz,Rotx,Roty,Rotz

Nonlinear S-DoF isolators and piers were connected in series. Resulting springs were connected to the deck. In order to take into account a pair of isolators for each pier, the restoring force of the proposed reduced isolator model was doubled. Same NRMSE scores were calculated with respect to the OpenSEES RM provided with isolator elements. They are reported in Table 6.6.

Table 6.6. NRMSE values for the isolated case.

Pier	SLS			ULS		
	Disp. [m]	Vel. [m/s]	Acc. [m/s2]	Disp. [m]	Vel. [m/s]	Acc. [m/s2]
1	0,12	0,07	0,08	0,09	0,09	0,08
2	0,07	0,06	0,11	0,05	0,05	0,08
3	0,07	0,05	0,13	0,10	0,06	0,07
4	0,10	0,09	0,13	0,10	0,09	0,08
5	0,13	0,11	0,13	0,12	0,11	0,09
6	0,09	0,08	0,11	0,09	0,08	0,08
7	0,09	0,09	0,12	0,10	0,08	0,07
8	0,09	0,07	0,09	0,08	0,08	0,09
9	0,14	0,10	0,09	0,11	0,12	0,10
10	0,11	0,09	0,09	0,08	0,06	0,08
11	0,13	0,09	0,07	0,10	0,09	0,08
12	0,10	0,09	0,09	0,08	0,08	0,06

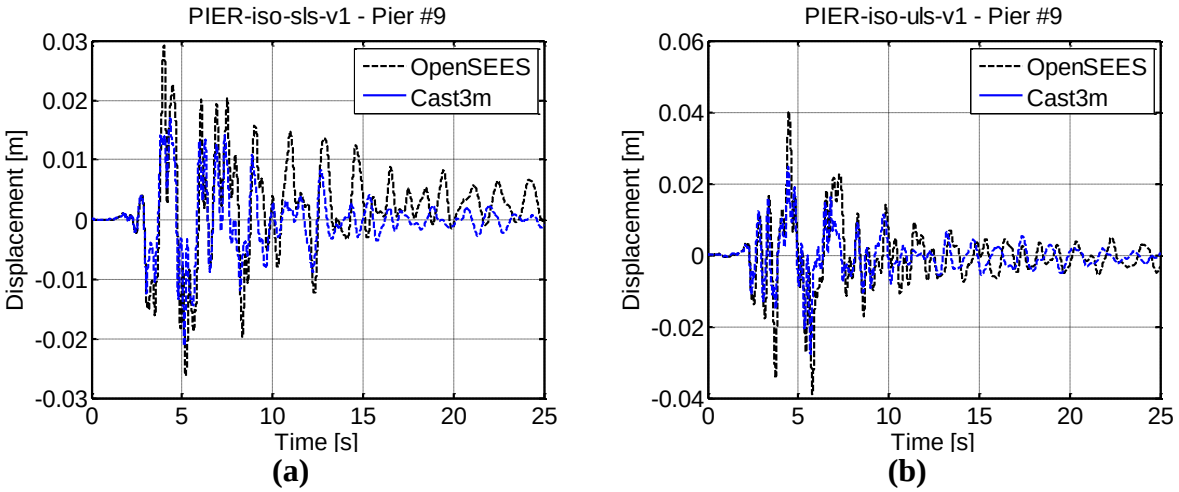

Figure 6.21 Cap beam level transversal displacement responses of Pier 9 in the isolated case at: a) SLS; b) ULS

As can be appreciated in Table 6.6, all displacements, velocity and acceleration responses of the reduced model match well the response of the OpenSEES RM. Fig. 6.21 compares cap beam level transversal displacement responses of Pier 9 obtained from the reduced model of the bridge to the OpenSEES reference solution:

A careful reader can observe a slight degradation of the matching quality occurred in the isolated case. The different mass matrix formulations of the (lumped) OpenSees and (consistent) reduced models can explain this phenomenon. In fact, to avoid matrix ill-conditioning, a consistent formulation was adopted for reduced models, whilst OpenSees allowed for lumped mass matrices only. Since hysteretic damping does not occur in the linear range experienced by piers in the isolated case, dynamic responses of higher eigenmodes, which are sensitive to small mass changes, deteriorate the kinematic matching. Proposed reduced models were implemented in the Cast3m FE code for the purpose of hybrid simulation. Scaled specimens of Piers 9 and 11 replaced relevant numerical models.

6.3. Model Updating

In order to simulate a consistent degradation of physical and numerical piers, a novel testing protocol was applied. It was based on recursive model identification and updating sessions aimed at propagating the damage experienced by the specimens to numerical piers. The block diagram of Fig. 6.22 summarizes this procedure:

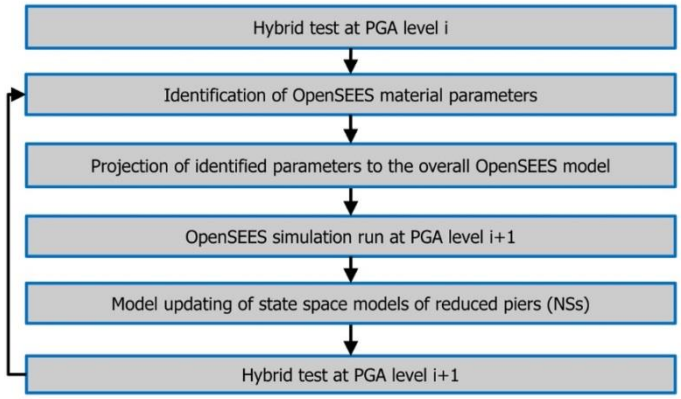

Figure 6.22 Flowchart of the testing procedure

According to Fig. 6.22, after a generic PsD run i-th-Step #1-, damage levels within both physical piers were identified in terms of *Concrete01* maximum compressive strengths $f_{pc}$of relevant OpenSEES 2D models -Step #2-. Fig. 6.23 depicts the constitutive law of the *Concrete01* OpenSEES material together with relevant parameters:

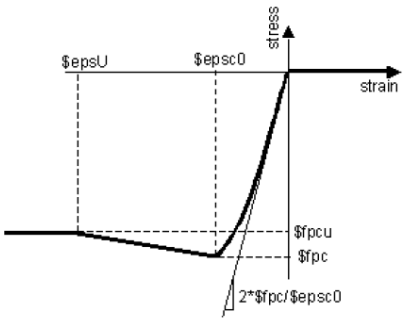

Figure 6.23 OpenSEES Concrete01 material definitions

The following dependencies were defined between all *Concrete01* parameters:

$$f_{pc} = identified \qquad \varepsilon_{c0} = -0.002 \qquad E_0 = \frac{2 \cdot f_{pc}}{\varepsilon_0}$$

$$f_{pcu} = 0.88 \cdot f_{pc} \qquad \varepsilon_{cu} = -0.006$$

A penalty function was defined as the NRMSE between the measured -$\mathbf{r}_{\text{mes}}$- and calculated -$\mathbf{r}_{\text{num}}$- restoring forces for a generic PDT run i-th:

$$\hat{f}_{cp,i} = \min_{f_{cp,i}} NRMSE\left(\mathbf{r}_{mes,i}, \mathbf{r}_{num,i}\left(\mathbf{x}_{mes,i}, f_{cp,i}\right)\right) \tag{6.9}$$

where:

- $\mathbf{x}_{mes,i}$: measured displacement history at the cap beam level;
- $\mathbf{r}_{mes,i}$: measured restoring force history at the cap beam level;
- $\mathbf{r}_{num,i}$: calculated restoring force history via OpenSEES;
- $f_{cp,i}$: maximum compressive strength of the *Concrete01* OpenSEES material;

In order to calculate $\mathbf{r}_{num,i}$, measured displacement histories $\mathbf{x}_{mes,i}$ were imposed to the relevant OpenSEES 2D model through nonlinear static analyses. For this purpose, measured signals were magnified to the model scale. Then, maximum compressive strengths of *Concrete01* material characterizing piers were propagated to the overall OpenSEES 3D RM -Step #3-. In detail, the maximum compressive strength identified on Pier 9 was applied to hollow section piers, whilst the one relevant to Pier 11 was applied to solid section piers. Pier cross-section types and localization are reported in Figure 6.24.

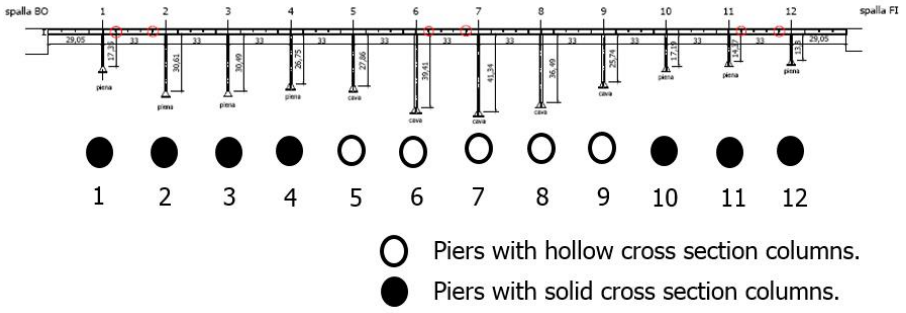

Figure 6.24 Pier cross section types and distribution

A time history analysis of the OpenSEES 3D RM was then conducted at the PGA level of the next PsD test run (i+1)-th -Step #4-. Finally, reduced S-DoF piers were tuned to match the dynamic response of the updated OpenSEES 3D RM and were implemented as numerical substructures for the purpose of hybrid simulation -Step #5-. The procedure was repeated until the end of the testing campaign. Table 6.7 summarizes OpenSEES Identification Sessions (ISs) and tests concerning the model updating of numerical piers.

Table 6.7. Scheduling of OpenSEES ISs and tests with updated piers.

Test	Description	Date
f03	Short pier, cyclic 1.5 mm. P=0.5,2 I=600	08/10/2013
f04	Tall pier, cyclic 2.0 mm. P=2 I=600	09/10/2013
IS #1		
k05	non-isolated bridge, 0.1SLS 25s	06/11/2013
IS #2		
k07	non-isolated bridge, 1.0 SLS 6.6s	08/11/2013
IS #3		
l01	isolated bridge, 1.0 SLS	12/11/2013
l02	isolated bridge, 1.0 ULS	13/11/2013
k09	non-isolated bridge, 1.0 ULS	19/11/2013
k10	non-isolated bridge, 1.0 ULS – A.S.	21/11/2013
k12	non-isolated bridge, 2.0 ULS	21/11/2013

Preliminary cyclic tests f03 and f04 were conducted in order to characterize the initial model. Further ISs were based on PDT results. Table 6.8 summarizes results of OpenSEES ISs.

Table 6.8 .Maximum compressive strengths of the OpenSEES*Concrete01* material.

Pier	IS #1 [MPa]	IS #2 [MPa]	IS #3 [MPa]
9	33.26	31.26	17.16
11	22.27	20.80	11.47

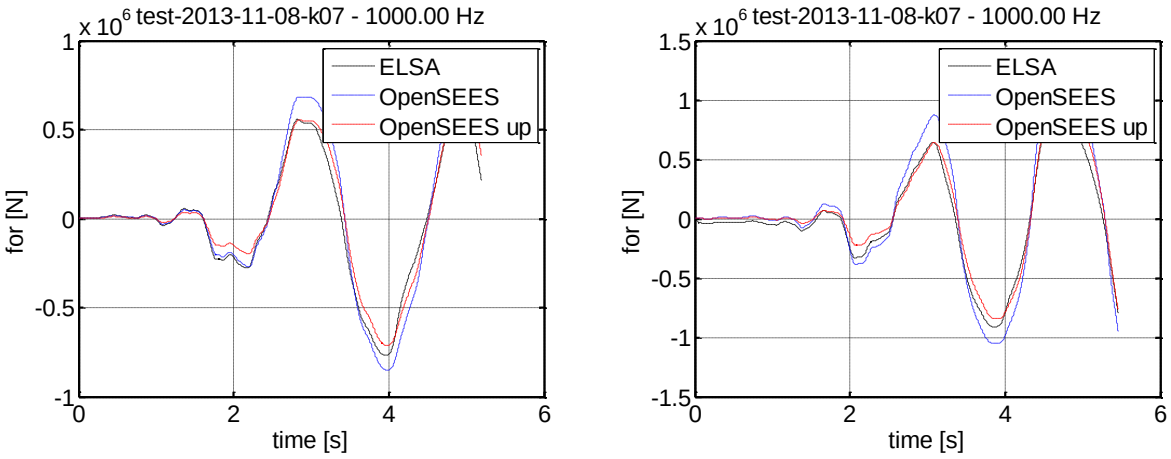

(a) (b)

Figure 6.25 Cap beam level restoring force responses of OpenSEES 2D models of a) Pier 9 and b) Pier 11 of Testk07

Further ISs confirmed that *Concrete01* parameters remained stable until the end of the testing campaign. Fig. 6.25 compares restoring force histories of updated OpenSEES 2D models of both piers to measured values of Test k07.

As can be appreciated, OpenSEES 2D models reproduced very well static responses of both specimens. Parameters of reduced nonlinear S-DoF piers are reported in the following Tables 6.9 through Table 6.15.

Table 6.9.Nonlinear parameters of S-DoF reduced piers for Test k05.

Pier	α	β	ρ
1	0,00	0,00	0,80
2	0,00	0,00	0,95
3	0,00	0,00	0,95
4	0,00	0,00	0,73
5	0,00	0,00	0,80
6	0,00	0,00	0,84
7	0,00	0,00	0,85
8	0,00	0,00	0,84
9	0,00	0,00	0,83
10	0,00	0,00	0,83
11	0,00	0,00	0,83
12	0,00	0,00	0,83

Table 6.10.Nonlinear parameters of S-DoF reduced piers for Test k07.

Pier	α	β	ρ
1	1208,99	0,19	0,68
2	169,74	0,06	0,75
3	76,08	1,14	0,66
4	85,71	0,93	0,51
5	87,58	1,88	0,50
6	32,50	1,18	0,60
7	6,43	2,00	0,50
8	61,66	0,69	0,61
9	252,93	0,80	0,67
10	596,65	0,00	0,71
11	490,83	1,82	0,57
12	1010,25	0,42	0,70

Table 6.11.Nonlinear parameters of S-DoF reduced piers for Test l01.

Pier	α	β	ρ
1	0,00	0,00	0,45
2	0,00	0,00	0,70
3	0,00	0,00	0,60
4	0,00	0,00	0,45
5	0,00	0,00	0,51
6	0,00	0,00	0,51
7	0,00	0,00	0,51
8	0,00	0,00	0,51
9	0,00	0,00	0,49
10	0,00	0,00	0,45
11	0,00	0,00	0,50
12	0,00	0,00	0,51

Table 6.12.Nonlinear parameters of S-DoF reduced piers for Test l02.

Pier	α	β	ρ
1	989,73	0,03	0,42
2	289,11	0,03	0,63
3	67,34	0,57	0,54
4	48,68	1,81	0,39
5	133,30	0,22	0,51
6	0,97	0,88	0,45
7	0,69	0,00	0,47
8	10,83	1,44	0,44
9	736,95	0,01	0,59
10	534,75	0,01	0,49
11	549,39	0,14	0,52
12	987,34	1,28	0,53

Table 6.13.Nonlinear parameters of S-DoF reduced piers for Test k09.

Pier	α	β	ρ
1	1,46	1,90	0,11
2	124,91	0,56	0,61
3	162,43	0,02	0,67
4	20,30	0,87	0,29
5	1,90	1,33	0,25
6	7,66	1,17	0,39
7	0,99	1,50	0,37
8	21,38	1,17	0,40
9	3,77	2,17	0,24
10	28,91	2,59	0,21
11	0,24	3,45	0,13
12	157,20	2,65	0,25

Table 6.14.Nonlinear parameters of S-DoF reduced piers for Test k10.

Pier	α	β	ρ
1	1,46	1,90	0,11
2	124,91	0,56	0,61
3	162,43	0,02	0,67
4	20,30	0,87	0,29
5	1,90	1,33	0,25
6	7,66	1,17	0,39
7	0,99	1,50	0,37
8	21,38	1,17	0,40
9	3,77	2,17	0,24
10	28,91	2,59	0,21
11	0,24	3,45	0,13
12	157,20	2,65	0,25

Table 6.15.Nonlinear parameters of S-DoF reduced piers for Test k12.

Pier	α	β	ρ
1	312.17	0.65	0.16
2	15.82	1.22	0.33
3	7.98	1.19	0.31
4	1.00	0.75	0.17
5	0.00	0.70	0.16
6	1.00	0.81	0.33
7	252.39	0.64	0.89
8	9.50	0.50	0.30
9	246.74	0.65	0.45
10	1.88	1.84	0.10
11	27.83	1.63	0.10
12	29.29	2.29	0.11

With reference to the non-isolated bridge, eigenfrequency trends of the first four modes are reported in Fig. 6.26. Initial tangent stiffness depending on updated parameters were considered for modal analyses.

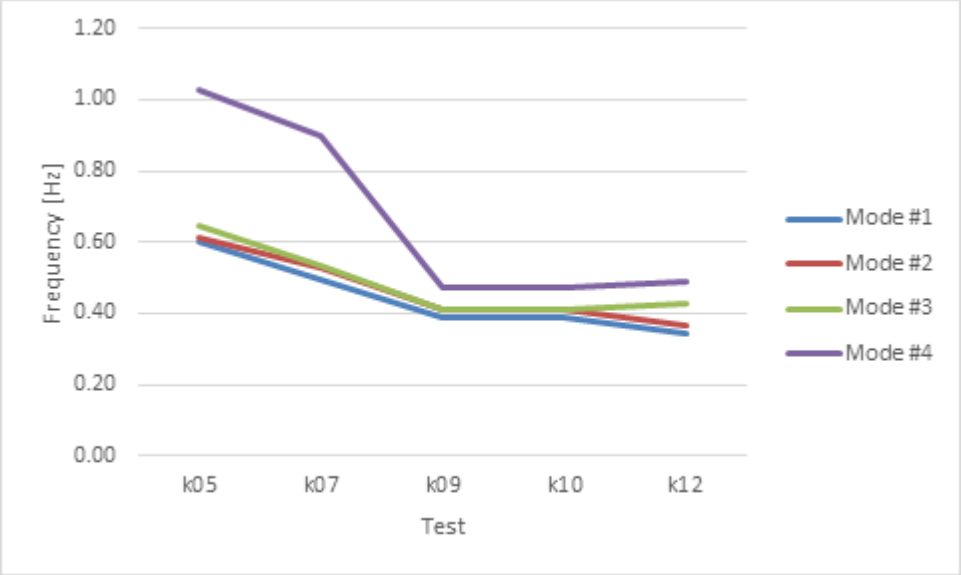

Figure 6.26.Trends of eigenfrequencies of the first four modes of the bridge in the non-isolated case

As can be appreciated in Fig. 6.26, all four modes experienced decreasing frequencies during the testing campaign. Table 6.16 summarizes the same data:

Table 6.16. Eigenfrequencies of the bridge in the non-isolated case at different testing phases.

	Frequency [Hz]				
Mode	Test k05	Test k07	Test k09	Test k10	Test k12
1	0,60	0,49	0,38	0,38	0,34
2	0,61	0,53	0,40	0,40	0,36
3	0,64	0,53	0,41	0,41	0,42
4	1,02	0,90	0,47	0,47	0,49

Damage affecting piers produced an appreciable degradation of the global transversal stiffness of the structure. Conversely, piers did not experience damage during the isolated tests.

7. SETUP AND INSTRUMENTATION

7.1. Testing rig

To load the piers model in the laboratory a steel frame was designed to simulate the effect and load transfer of the bridge deck. At the same time the loading frame provided anchorage points for actuators, two for horizontal and two for vertical loading at each pier.

Fig.7.1 shows the two piers as they were installed at ELSA. At the top of each of the piers the loading frame is secured with bolts anchored in the piers' concrete beams. The loading frame (Fig. 7.2 and Fig. 7.3) provides a 0.80 m lever arm for the horizontal actuators applying horizontal displacements and measuring forces during testing.

Actuators installed (rendered blue in Fig. 7.1) at the top of every pier's column applied vertical load by tensioning a Dywidag bar passing through piers and being anchored at the footing. Vertical load was applied to the piers before the start of the PsD test.

For each of the two piers there was also a seismic isolator set-up installed. It was positioned on the strong floor in front of the piers using their footing as a support for the horizontal actuators. Seismic actuators were mounted on a strong steel plate with a middle plate on top of them. Then another set of isolators, turned upside down, was mounted on the middle plate with another steel plate on top of them. The bottom steel plate was bolted to the strong floor of the laboratory. The middle steel plate was connected to an actuator which applied horizontal displacements during the tests. The top steel plate was braced with two beams that blocked horizontal displacements while allowing vertical displacements so that the isolators could work properly. The vertical load was applied by four actuators installed on the top plate by pulling a bar fixed at the bottom plate. Drawings of the isolator set-up are shown in Fig. 7.4 and Fig. 7.5.

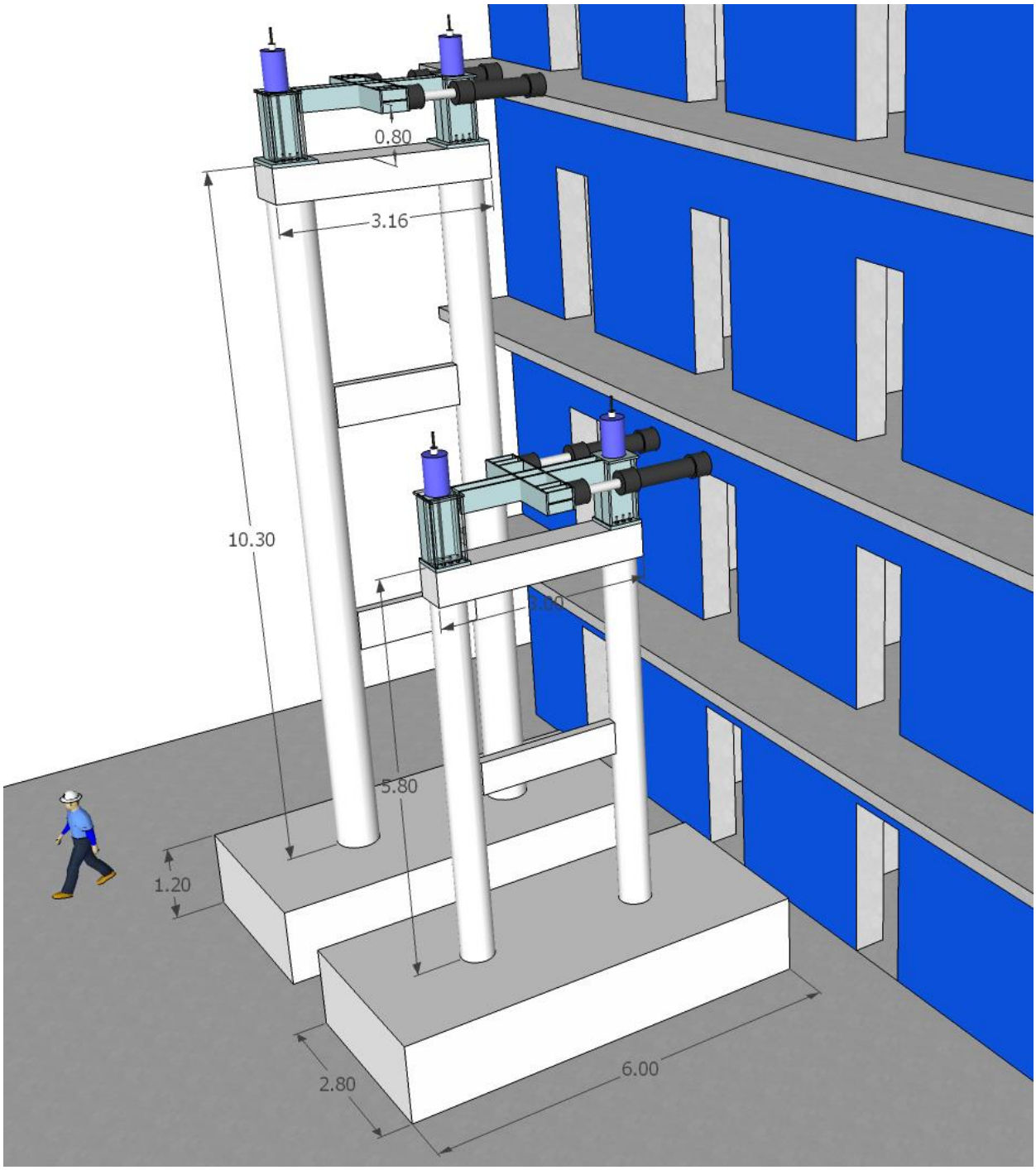

Figure7.1 Mock-up of the RETRO piers in ELSA

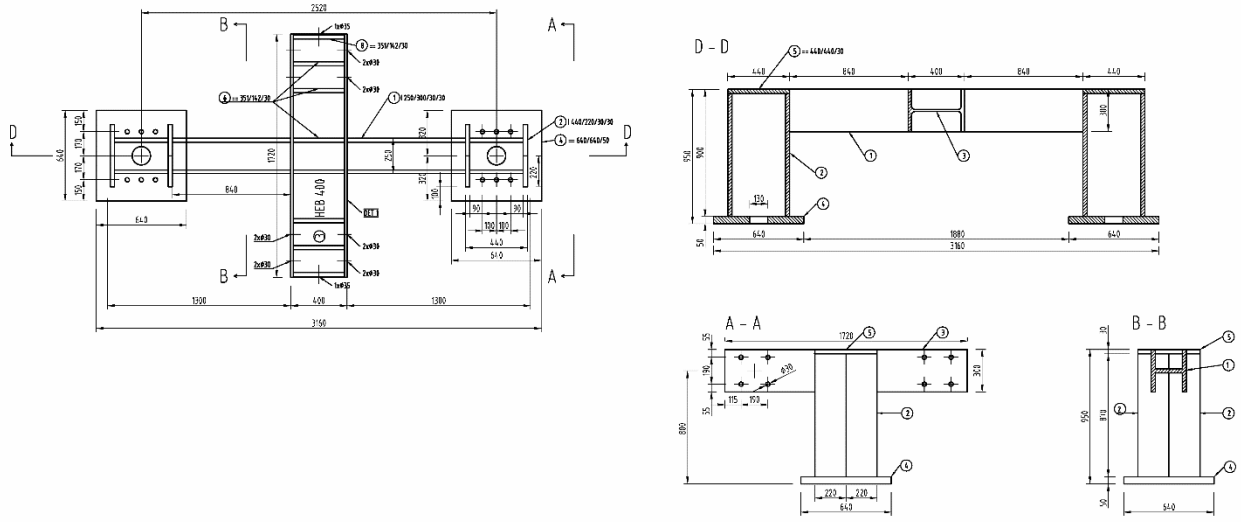

Figure7.2 Loading frame of Pier 9

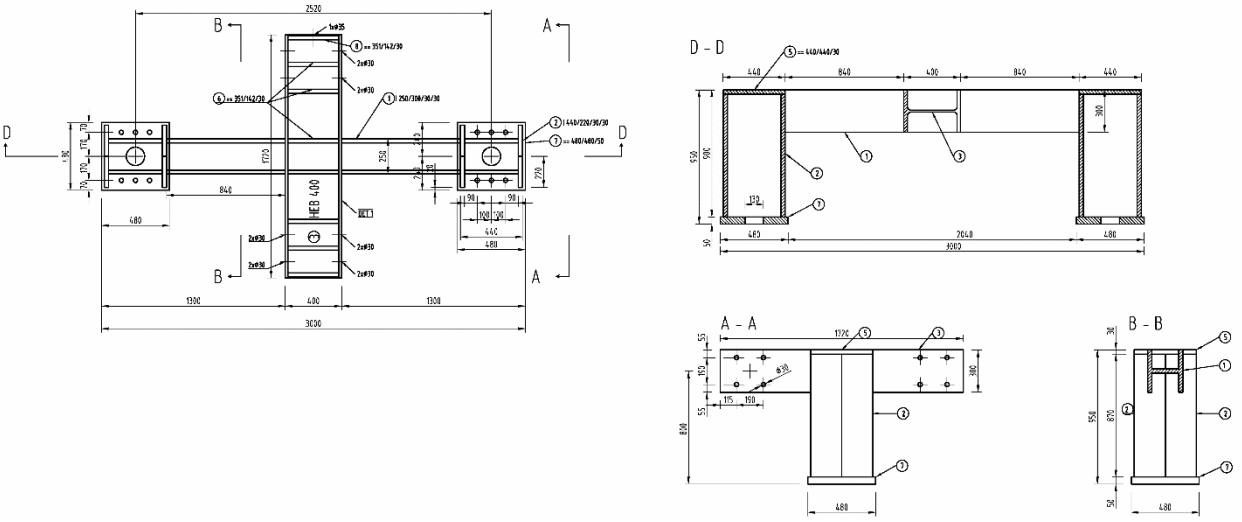

Figure7.3 Loading frame of Pier 11

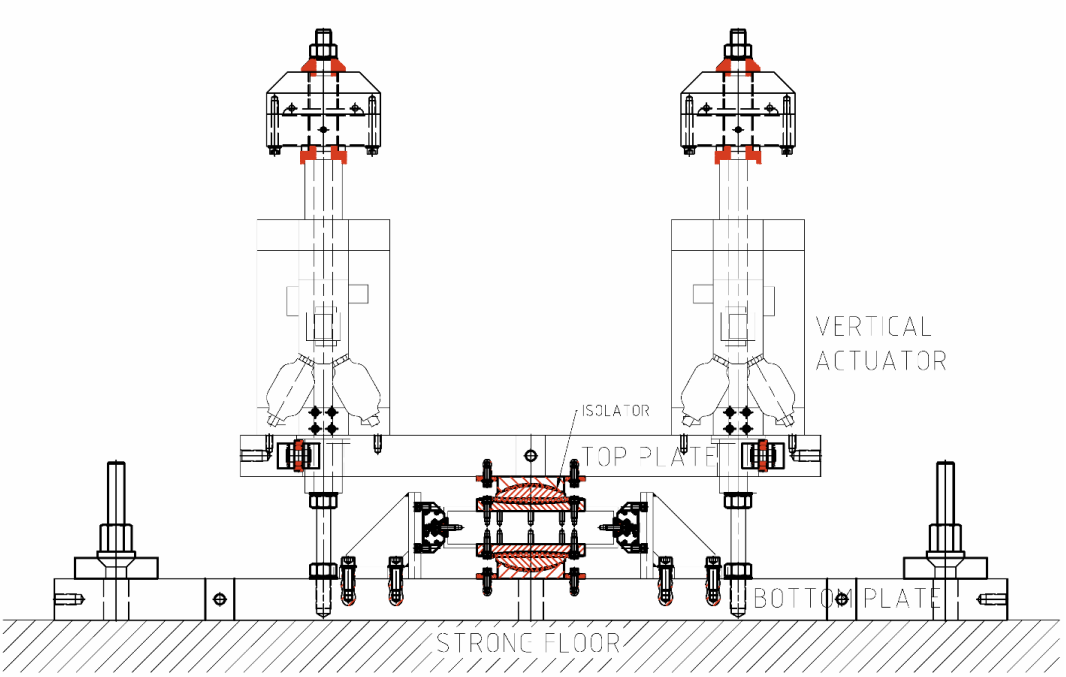

Figure 7.4 Cross section of the isolator set-up

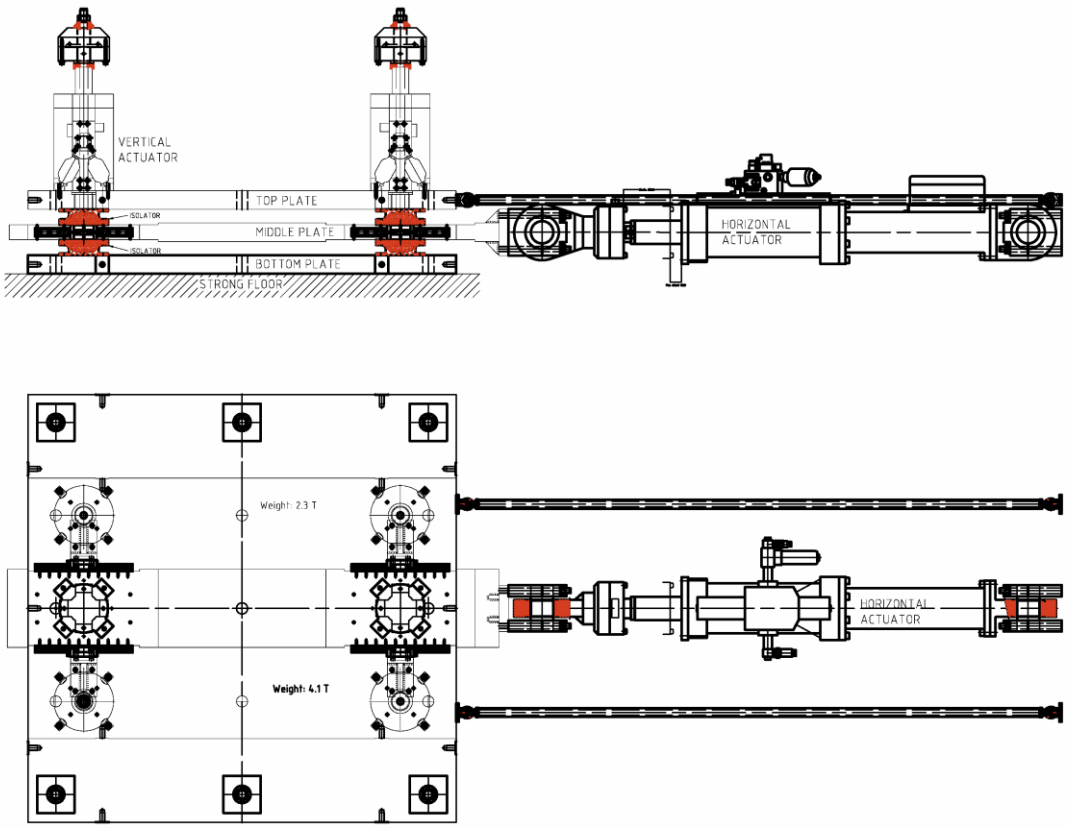

Figure 7.5 Top and side view of the isolator set-up

7.2. Control Strategy

The test setup consisted of 18 actuators (see Fig. 7.6). At ELSA, every actuator has associated typically a TEMPOSONICS displacement transducer, measuring the displacement of the piston with respect to the cylinder, a load cell, measuring its applied axial force and some other sensors for the oil pressure at the chambers and for the servo-valve spool displacement. For this setup, the horizontal actuators also had a HEIDENHAIN displacement transducer measuring the displacement at a point of the specimen with respect to a fixed reference frame. These measurements, as well as the reference target and the servo-valve command are dealt, for every actuator, by a SLAVE controller, which is also in charge of the PID algorithm to compute the servo-valve command. A number of up to four SLAVE controllers are connected to a MASTER controller that exchanges all signals at the controller with a sampling period of 2ms within the ELSA testing system [61]. The MASTER controller uses a DLL program that, by interacting with all those signals relative to the SLAVE controllers, is able to manage different kinds of tests, such as cyclic, monolithic PsD (with all the analytical substructure inside of the MASTER DLL) or distributed PsD (with the analytical substructure running in a separate computer network).

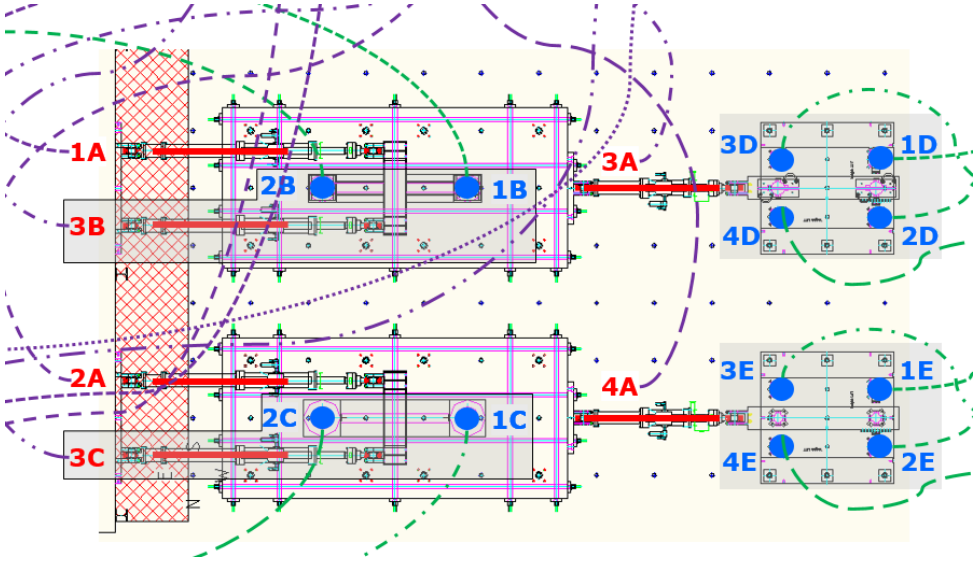

Figure 7.6 Actuator set-up

7.2.1. Short and tall piers control

In order to introduce the gravity load coming from the deck, not present physically in the laboratory, every pier was loaded by two vertical actuators, one at the West column and one at the East column of the pier. The East column of the pier was the closest one to the reaction wall. These vertical actuators were always used in force control with a constant specified target force of -450 kN during the tests in which they were used. The force was measured by a load cell between the piston and the end nut of the DIWIDAG bar. This steel bar was passing through the load cell and the piston, going inside of the column and fixed at the bottom of the foundation. At the beginning of the test, the target force was increased by a cosine function growing from zero up to the specified value. In the case of the seismic tests, the initial phase of gradual increase of the vertical load has negative time abscissa and the earthquake excitation starts at zero time.

Once the pier had the constant vertical load applied by the vertical actuators, two horizontal actuators working in displacement control imposed the cyclic or PsD target, so that the translation was imposed without any torsion. The transducer used as feedback for these actuators was a digital optical HEIDENHAIN encoder measuring the movement of the upper steel loading rig in the axis of the actuator and with respect to the reference frame resting on the strong floor. For every pier, the SLAVE controller for the South (closer to the controllers) horizontal actuator received its digital target from MASTER A, which was the only MASTER used for running a PsD method through its DLL, whereas the North horizontal actuator had its SLAVE belonging to a different MASTER. The signal of the target for the North actuator was communicated in analogue form between the affected MASTER controllers. In a similar manner, for the PsD tests, the force applied by the North actuator was communicated back to MASTER A as an analogue signal so that it could be computed in the restoring force within the equation of motion together with the force applied by the South actuator.

7.2.2. Short and tall piers control

Every isolator setup had four vertical actuators positioned at the corners of the upper rectangular plate and numbered 1…4. Actuators 1 (South-West) and 2 (North-West) applied a total specified force:

$$F_{WEST} = F_1 + F_2 \tag{7.1}$$

With centre on the West column of isolators. Actuators 3 (South-East) and 4 (North-East) applied a total specified force

$$F_{EAST} = F_3 + F_4 \tag{7.2}$$

With centre on the East column of isolators, the control of the four actuators was based on the imposition of Eq. 7.1 and Eq. 7.2 plus two additional constraints. The rolling rotation was imposed to be null, or equivalently, by using the TEMPOSONICS displacements of the four pistons with respect to the cylinders:

$$T_1 - T_2 + T_3 - T_4 = 0 \tag{7.3}$$

And, finally, the warping was controlled by imposing null warping moment, $M_\omega = 0$, or equivalently:

$$F_1 - F_2 - F_3 + F_4 = 0 \tag{7.4}$$

Equations 7.1 through 7.4 are equivalent to the set of constraints:

$$\begin{aligned} F_1 &= F_{WEST} - F_2 \\ F_2 &= F_1 - F_3 + F_4 \\ F_3 &= F_{EAST} - F_4 \\ T_4 &= T_1 - T_2 + T_3 \end{aligned} \tag{7.5}$$

In practice, the constraints were imposed by controlling three actuators with feedback in force (F_1, F_2 and F_3) and the last one with feedback in displacement (T_4). The standard formula for the control error as input to the PID control algorithm

$$e=\{Target\}-\{Feedback\} \tag{7.6}$$

$$\begin{aligned} e_1&=\{F_{WEST}-F_2\}-\{F_1\} \\ e_2&=\{F_1-F_3+F_4\}-\{F_2\} \\ e_3&=\{F_{EAST}-F_4\}-\{F_3\} \\ e_4&=\{T_1-T_2+T_3\}-\{T_4\} \end{aligned} \tag{7.7}$$

For the four vertical actuators, the value of the four targets, as defined by Eq. 7.7, was computed by the MASTER controller associated to these four actuators. Depending on the kind of test, F_{WEST} and F_{EAST} had a constant value of -450 kN or varied with an addition term, according to either a specified random history or a proportion of the pitching moment introduced by the horizontal actuators of the respective pier. In fact, the value of the force

applied by the horizontal actuators of the respective pier was communicated to this MASTER by analogue signals. The initial phase of gradual increase of the vertical forces from zero to -450 kN was done with a cosine history and simultaneously for the piers and isolators.
Every isolator setup had a horizontal actuator for imposing the same deformation on the four isolators through the guided medial beam. This actuator was used in displacement control by using a HEIDENHAIN encoder measuring the displacement of that beam with respect to the strong floor. The SLAVE of this actuator belonged to MASTER A, which was communicating the target to it as computed from the equation of motion in the PsD tests, including the isolator specimens.

7.3. Sensors and acquisition system

In the transverse section of the pier, a number of extensometers were installed in order to measure local deformation and global displacements. Fig. 7.8 shows three ‘wire’ analogue Temposonics sensors on pier 9 to measure global displacement at each level of the transverse beams, together with 74 potentiometer Gefran sensors installed in different levels above the column base, lower and upper beam-column joints and in the transverse beams. Each transverse beam was divided into four parts, each part with one diagonal, right, left, upper and lower sensors, as shown in the Fig. 7.7

Figure 7.7 Extensimeter sensors on the transverse beam

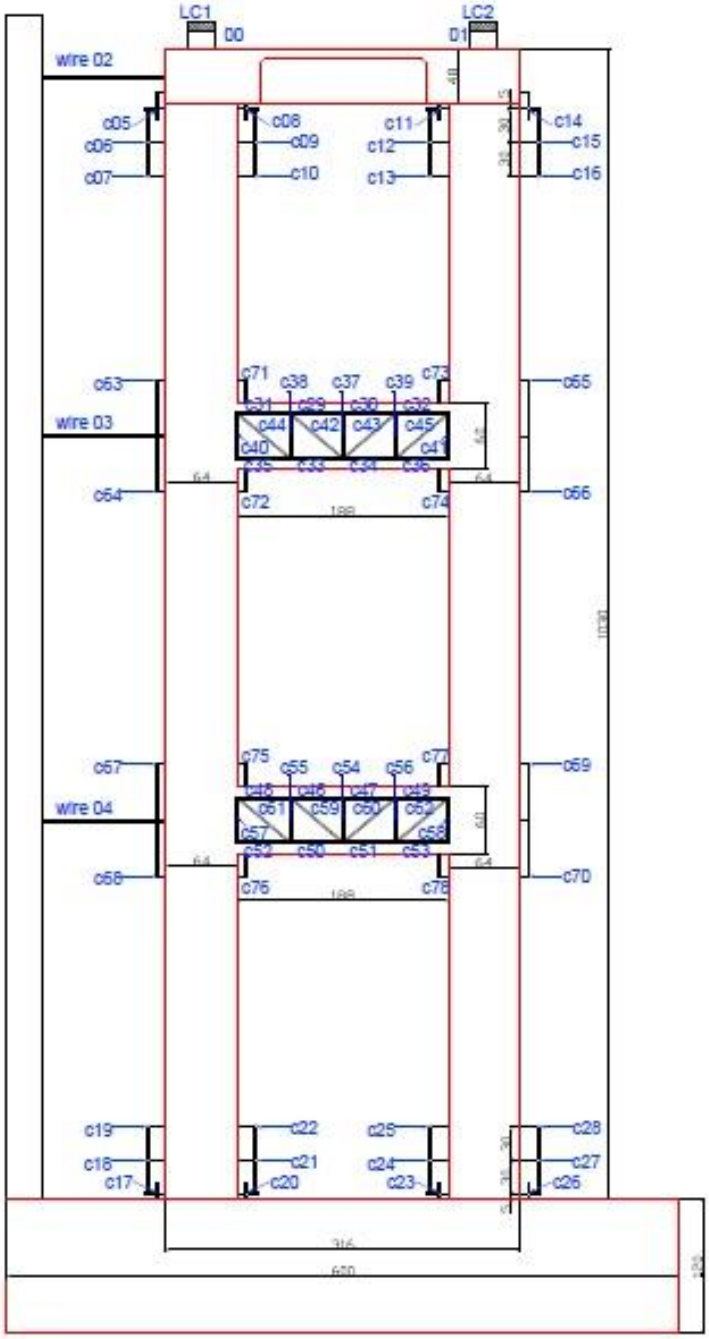

Figure 7.8 Extensimeter sensors map of pier 9

Table 7.1 shows the number, position, length and name of each sensor on pier 9

Table 7.1 Extensimeter sensors table for pier 9

Transducers Table - Pier 9

Channel #	Length	Typology	Name
00		LC 1	cover A
01		LC 2	cover B
02		Wire s.	lev3. wire
03		Wire s.	lev2. wire
04		Wire s.	lev1. wire
05	15,00	LVDT 50 mm	L3_lx_lx1
06	30,00	LVDT 50 mm	L3_lx_lx2
07	30,00	LVDT 50 mm	L3_lx_lx3
08	05,00	LVDT 50 mm	L3_lx_rx1
09	30,00	LVDT 50 mm	L3_lx_rx2
10	30,00	LVDT 50 mm	L3_lx_rx3
11	05,00	LVDT 50 mm	L3_rx_lx1
12	30,00	LVDT 50 mm	L3_rx_lx2
13	30,00	LVDT 50 mm	L3_rx_lx3
14	15,00	LVDT 50 mm	L3_rx_rx1
15	30,00	LVDT 50 mm	L3_rx_rx2
16	30,00	LVDT 50 mm	L3_rx_rx3
17	05,00	LVDT 50 mm	Lo_lx_lx1
18	30,00	LVDT 50 mm	Lo_lx_lx2
19	30,00	LVDT 50 mm	Lo_lx_lx3
20	05,00	LVDT 50 mm	Lo_lx_rx1
21	30,00	LVDT 50 mm	Lo_lx_rx2
22	30,00	LVDT 50 mm	Lo_lx_rx3
23	05,00	LVDT 50 mm	Lo_rx_lx1
24	30,00	LVDT 50 mm	Lo_rx_lx2
25	30,00	LVDT 50 mm	Lo_rx_lx3
26	05,00	LVDT 50 mm	Lo_rx_rx1
27	30,00	LVDT 50 mm	Lo_rx_rx2
28	30,00	LVDT 50 mm	Lo_rx_rx3
29	47,00	LVDT 50 mm	L2_tp_lx1
30	47,00	LVDT 50 mm	L2_tp_rx1
31	47,00	LVDT 50 mm	L2_tp_lx2
32	47,00	LVDT 50 mm	L2_tp_rx2
33	47,00	LVDT 50 mm	L2_bt_lx1
34	47,00	LVDT 50 mm	L2_bt_rx1
35	47,00	LVDT 50 mm	L2_bt_lx2
36	47,00	LVDT 50 mm	L2_bt_rx2
37	40,00	LVDT 50 mm	L2_co_m
38	40,00	LVDT 50 mm	L2_co_lx1
39	40,00	LVDT 50 mm	L2_co_rx1
40	40,00	LVDT 50 mm	L2_co_lx2
41	40,00	LVDT 50 mm	L2_co_rx2
42	61,70	LVDT 50 mm	L2_di_lx1
43	61,70	LVDT 50 mm	L2_di_rx1
44	61,70	LVDT 50 mm	L2_di_lx2
45	61,70	LVDT 50 mm	L2_di_rx2
46	47,00	LVDT 50 mm	L1_tp_lx1
47	47,00	LVDT 50 mm	L1_tp_rx1
48	47,00	LVDT 50 mm	L1_tp_lx2
49	47,00	LVDT 50 mm	L1_tp_rx2
50	47,00	LVDT 50 mm	L1_bt_lx1
51	47,00	LVDT 50 mm	L1_bt_rx1
52	47,00	LVDT 50 mm	L1_bt_lx2
53	47,00	LVDT 50 mm	L1_bt_rx2
54	40,00	LVDT 50 mm	L1_co_m
55	40,00	LVDT 50 mm	L1_co_lx1
56	40,00	LVDT 50 mm	L1_co_rx1
57	40,00	LVDT 50 mm	L1_co_lx2
58	40,00	LVDT 50 mm	L1_co_rx2
59	61,70	LVDT 50 mm	L1_di_lx1
60	61,70	LVDT 50 mm	L1_di_rx1
61	61,70	LVDT 50 mm	L1_di_lx2
62	61,70	LVDT 50 mm	L1_di_rx2
63	44,00	LVDT 50 mm	L1_ou_lt
64	44,00	LVDT 50 mm	L1_ou_lb
65	44,00	LVDT 50 mm	L1_ou_rt
66	44,00	LVDT 50 mm	L1_ou_rb
67	20,00	LVDT 50 mm	L1_in_lt
68	20,00	LVDT 50 mm	L1_in_lb
69	20,00	LVDT 50 mm	L1_in_rt
70	20,00	LVDT 50 mm	L1_in_rb
71	44,00	LVDT 50 mm	L1_di_lx2
72	44,00	LVDT 50 mm	L1_ou_lb
73	44,00	LVDT 50 mm	L1_ou_rt
74	44,00	LVDT 50 mm	L1_ou_rb
75	20,00	LVDT 50 mm	L1_in_lt
76	20,00	LVDT 50 mm	L1_in_lb
77	20,00	LVDT 50 mm	L1_in_rt
78	20,00	LVDT 50 mm	L1_in_rb

A similar sensor map was prepared for Pier 11. Fig. 7.9 shows two ‘wire’ sensors to measure the global displacement at each level corresponding to the transverse beams, and 49 sensors installed in different locations to measure local deformations. Table 7.2 shows the sensors map of pier 11.

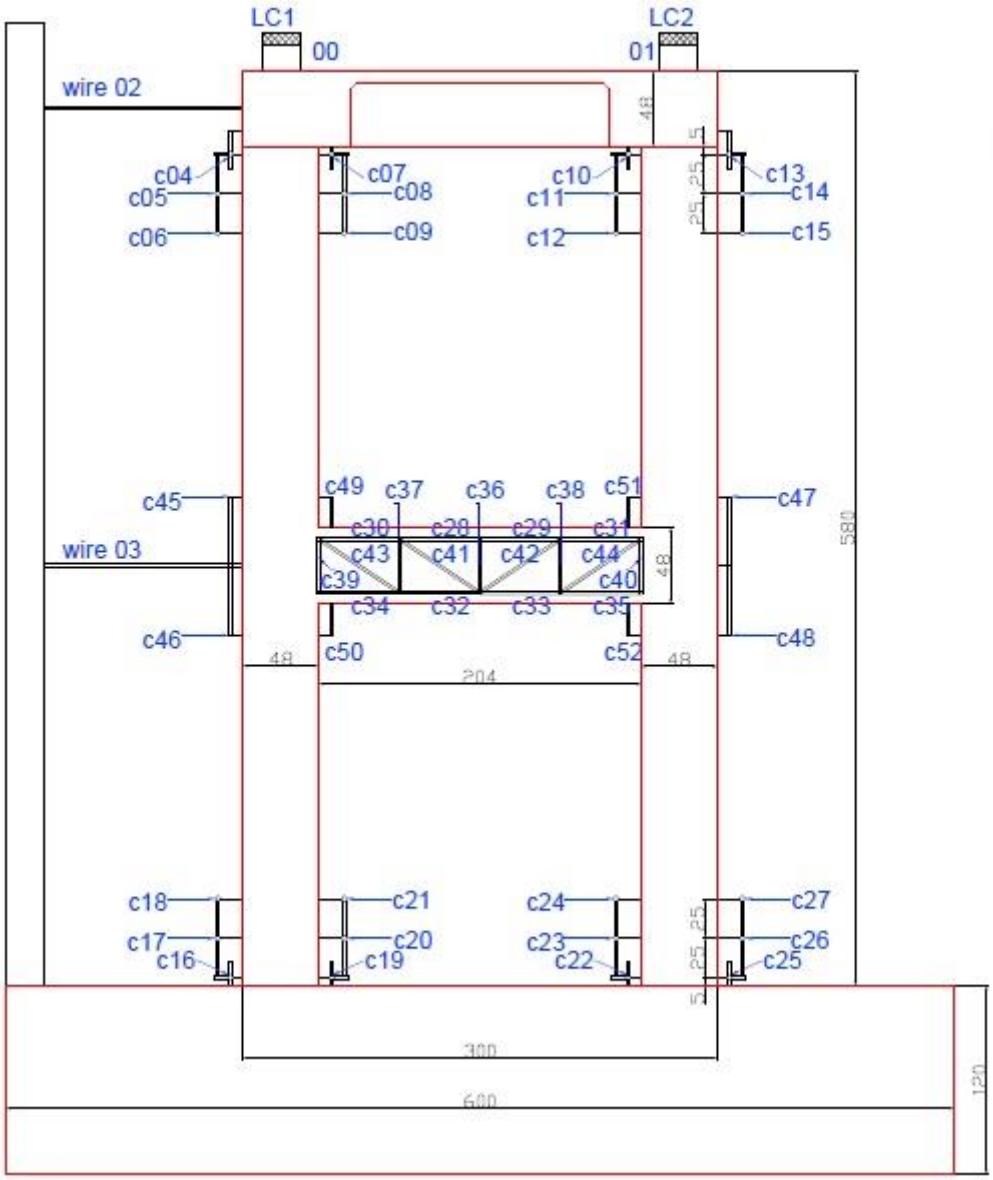

Figure 7.9 Extensimeter sensors map of pier 11

Table 7.2 Extensimeter **sensors table for pier 11**

Transducers Table - Pier 11

Channel #	Length	Typology	Name
00		LC 1	cover A
01		LC 2	cover B
02		Wire s.	top. wire
03		Wire s.	mid. wire
04	15,00	LVDT 50 mm	L2_lx_lx1
05	25,00	LVDT 50 mm	L2_lx_lx2
06	25,00	LVDT 50 mm	L2_lx_lx3
07	05,00	LVDT 50 mm	L2_lx_rx1
08	25,00	LVDT 50 mm	L2_lx_rx2
09	25,00	LVDT 50 mm	L2_lx_rx3
10	05,00	LVDT 50 mm	L2_rx_lx1
11	25,00	LVDT 50 mm	L2_rx_lx2
12	25,00	LVDT 50 mm	L2_rx_lx3
13	15,00	LVDT 50 mm	L2_rx_rx1
14	25,00	LVDT 50 mm	L2_rx_rx2
15	25,00	LVDT 50 mm	L2_rx_rx3
16	05,00	LVDT 50 mm	Lo_lx_lx1
17	25,00	LVDT 50 mm	Lo_lx_lx2
18	25,00	LVDT 50 mm	Lo_lx_lx3
19	05,00	LVDT 50 mm	Lo_lx_rx1
20	25,00	LVDT 50 mm	Lo_lx_rx2
21	25,00	LVDT 50 mm	Lo_lx_rx3
22	05,00	LVDT 50 mm	Lo_rx_lx1
23	25,00	LVDT 50 mm	Lo_rx_lx2
24	25,00	LVDT 50 mm	Lo_rx_lx3
25	05,00	LVDT 50 mm	Lo_rx_rx1
26	25,00	LVDT 50 mm	Lo_rx_rx2
27	25,00	LVDT 50 mm	Lo_rx_rx3
28	51,00	LVDT 50 mm	L1_tp_lx1
29	51,00	LVDT 50 mm	L1_tp_rx1
30	51,00	LVDT 50 mm	L1_tp_lx2
31	51,00	LVDT 50 mm	L1_tp_rx2
32	51,00	LVDT 50 mm	L1_bt_lx1
33	51,00	LVDT 50 mm	L1_bt_rx1
34	51,00	LVDT 50 mm	L1_bt_lx2
35	51,00	LVDT 50 mm	L1_bt_rx2
36	34,00	LVDT 50 mm	L1_co_m
37	34,00	LVDT 50 mm	L1_co_lx1
38	34,00	LVDT 50 mm	L1_co_rx1
39	34,00	LVDT 50 mm	L1_co_lx2
40	34,00	LVDT 50 mm	L1_co_rx2
41	61,30	LVDT 50 mm	L1_di_lx1
42	61,30	LVDT 50 mm	L1_di_rx1
43	61,30	LVDT 50 mm	L1_di_lx2
44	61,30	LVDT 50 mm	L1_di_rx2
45	44,00	LVDT 50 mm	L1_ou_lt
46	44,00	LVDT 50 mm	L1_ou_lb
47	44,00	LVDT 50 mm	L1_ou_rt
48	44,00	LVDT 50 mm	L1_ou_rb
49	20,00	LVDT 50 mm	L1_in_lt
50	20,00	LVDT 50 mm	L1_in_lb
51	20,00	LVDT 50 mm	L1_in_rt
52	20,00	LVDT 50 mm	L1_in_rb

7.4. Photogrammetry

Two pairs of high resolution PCO.Edge cameras were deployed to monitor the short pier during the test campaign (Fig. 7.10). Each pair of cameras provides data, synchronized with the test controller, which enabled to create a 3D displacement field, crack propagation and degradation of a monitored surface during a test for all points of the input accelerogram. The monitored surface was painted with an artificially created random speckled pattern enabling a reliable pattern recognition in post processing.

The first pair of cameras was focused on a column section of the short pier in the bottom area (Fig. 7.10). To register also the back side of the column two astronomical mirrors were installed to reflect the back side image in the cameras' view.

The first cross beam of the short pier and a part of columns was monitored with the second pair of cameras as seen in Fig. 7.11. As an example of preliminary results, a sequence of plots showing the crack pattern of the transverse beam of pier 11 is shown in Fig. 7.13 through 7.17.

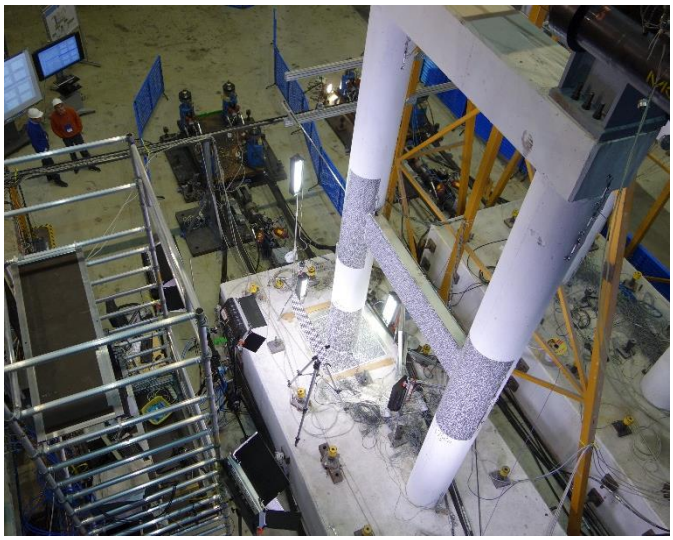

Figure 7.10 Camera setup

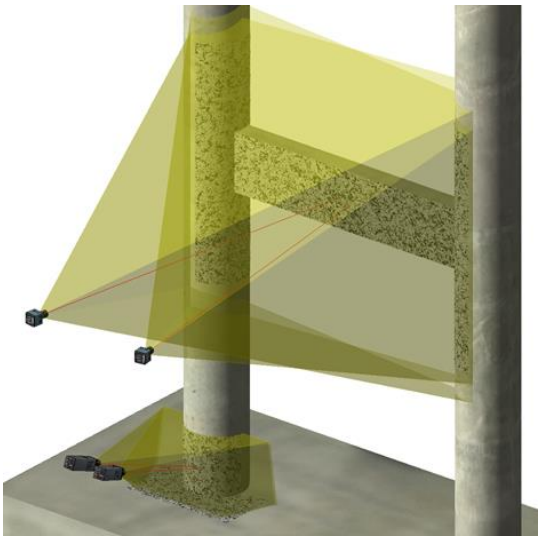

Figure 7.11 Mock up of the camera view

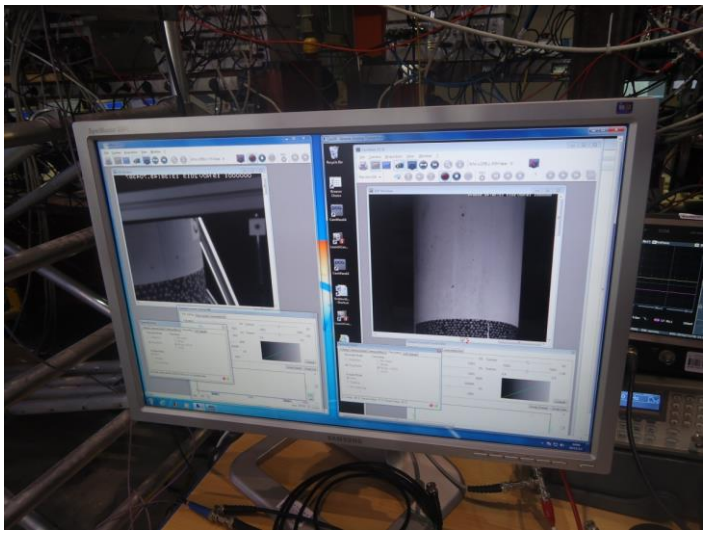

Figure 7.12 Photogrammetry camera pictures shown directly on computers

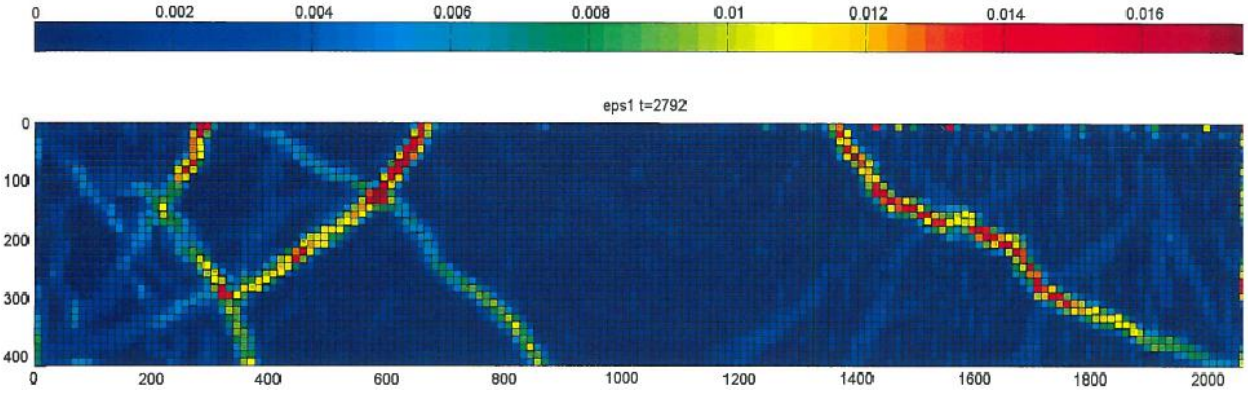

Figure 7.13 Photogrammetry x-y view on transversal beam for pier 11

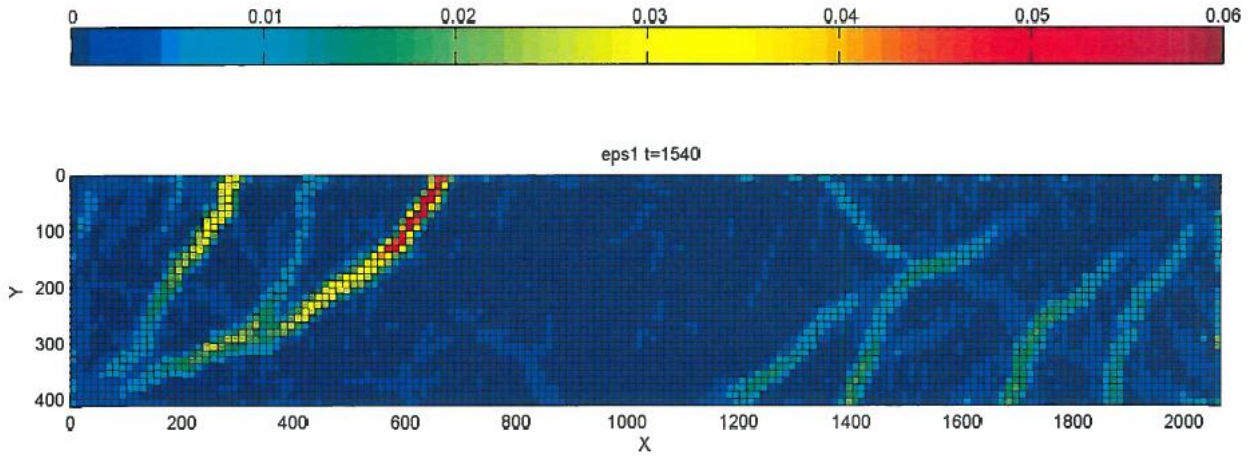

Figure 7.14 Photogrammetry x-y view on transversal beam for pier 11

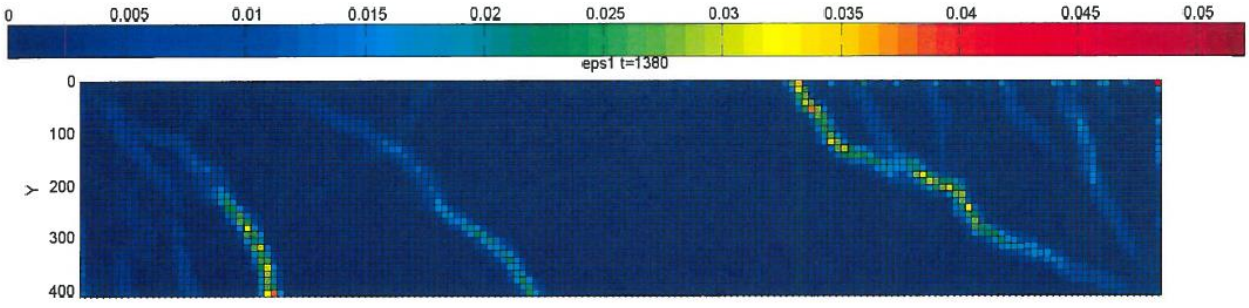

Figure 7.15 Photogrammetry x-y view on transversal beam for pier 11

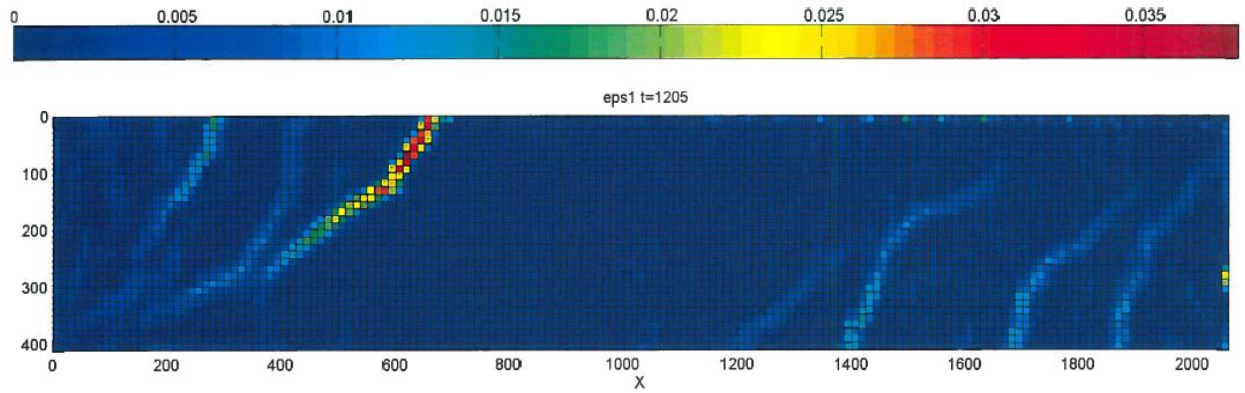

Figure 7.16 Photogrammetry x-y view on transversal beam for pier 11

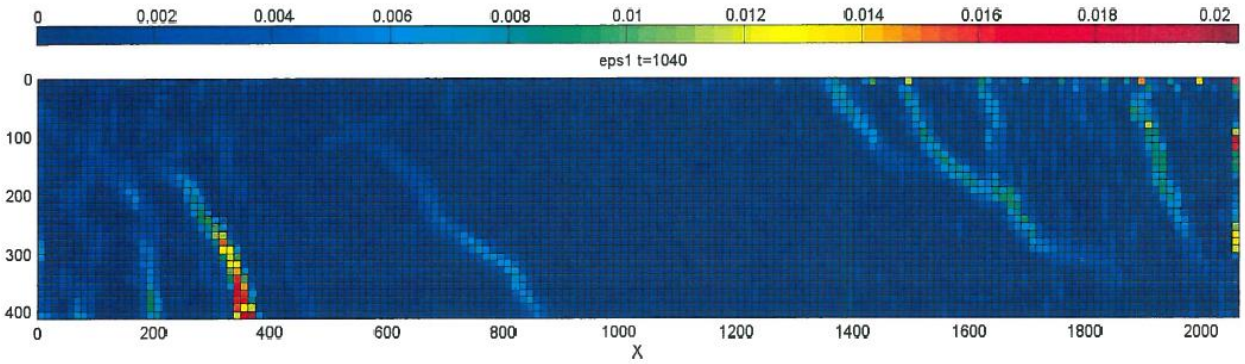

Figure 7.17 Photogrammetry x-y view on transversal beam for pier 11

8. SEISMIC INPUT

Two limit states are considered for the seismic performance assessment of the "as built" Rio-Torto bridge: Serviceability Limit State (SLS) and Ultimate Limit State (ULS), respectively. Given the geographical position of the bridge and the recent earthquake swarms occurred in the region (especially the earthquake records of the 20th and 29th May 2012), it was decided to use the seismic records of the 2012 Emilia (Italy) earthquakes. The Mirandola records (MRN station) were utilized because of their seismological characteristics, i.e. PGAs and duration of the accelerograms. The record of May 29th East-West event was used for the SLS and the North-South component was used to assess the seismic performance at the ULS.

8.1. Ultimate limit state (ULS)

The earthquake record relative to the North-South component of the 29th May seismic event, as recorded in Mirandola, is shown in Fig. 8.1, along with the velocity and displacement response history.

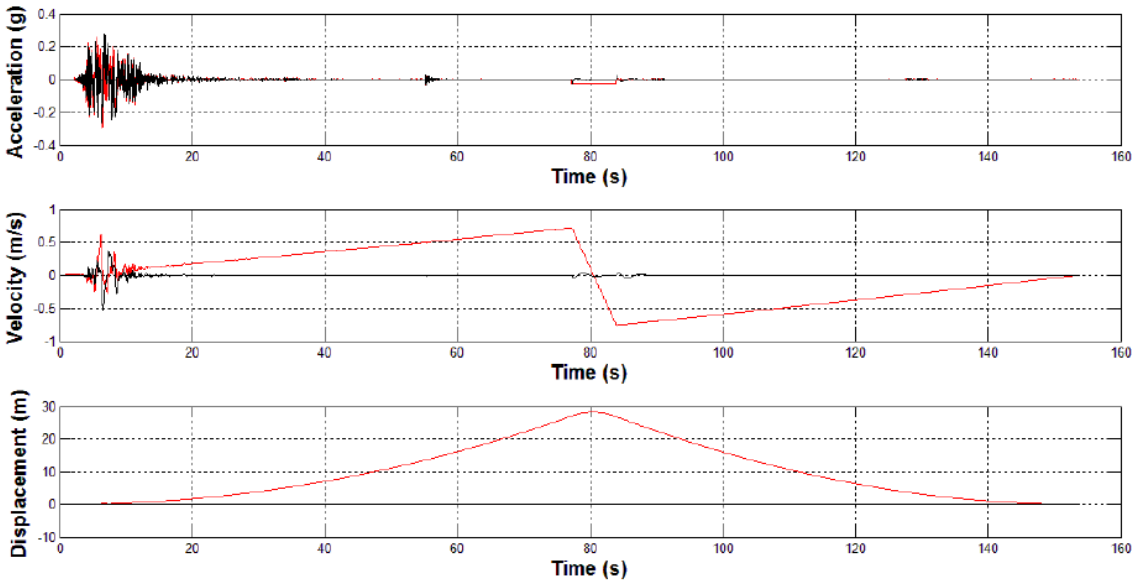

Figure 8.1 Record of the 29th May 2012 (N-S Component): acceleration (top), velocity (middle) and displacement (bottom) response histories

The red line in the above figure are the uncorrected signals, the black lines are the correct ones. The correction is achieved with a baseline correction on the acceleration profile and then it is applied a pass-band Butterworth filter in the interval [0.25 Hz - 25.0 Hz].

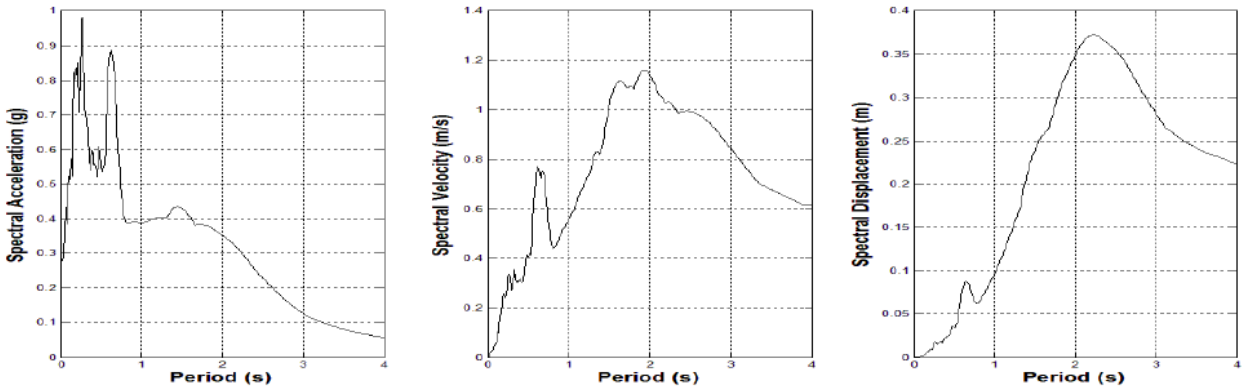

Figure 8.2 Response spectra of the record of the 29th May 2012 (N-S Component): acceleration (left), velocity (middle) and displacement (right) spectra

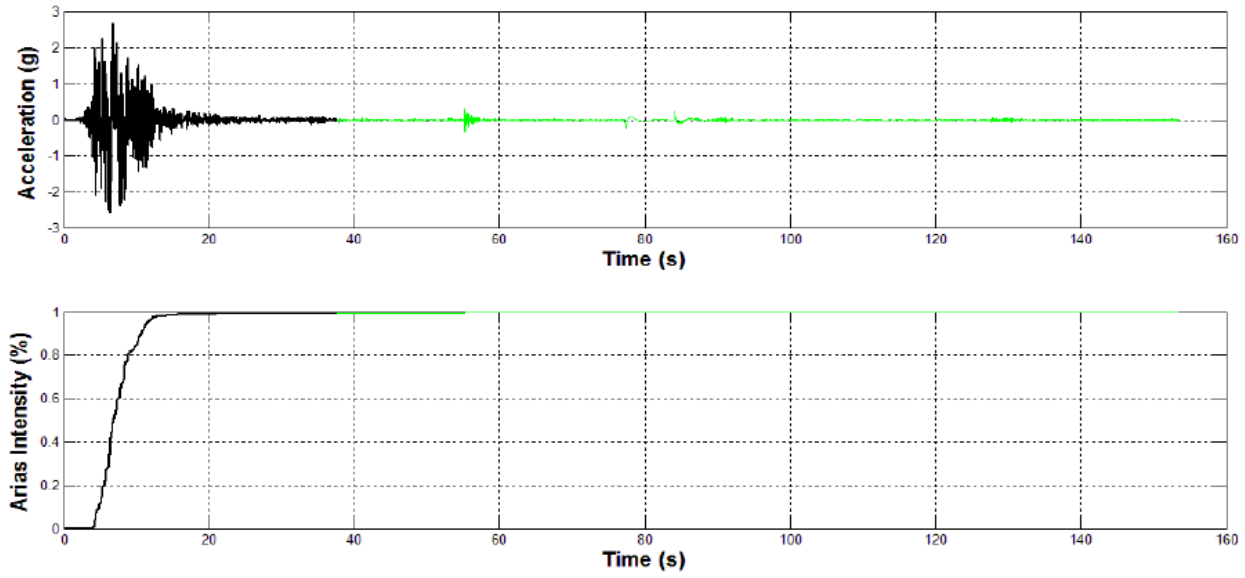

Figure 8.3 Reduction of the signal length

The response spectra of the sample record are provided in Fig. 8.2. It is observed a significant amplification for low-periods (between 0.5 and 1.0 seconds); values of spectral accelerations around 0.40g are also found in a period range 1-1.5 seconds, i.e. similar to the important natural periods of the part of the "as built bridge" in which pier 9 and 11 are located. The length of the signal was reduced assuming to a significant length which the Arias intensity is up to 99,4% (Fig. 8.3). The input was selected in order to respond to the compatibility criteria

with the ULS design spectra dictated by EN1998:1. The signal used in the analysis is shown in Fig. 8.4.

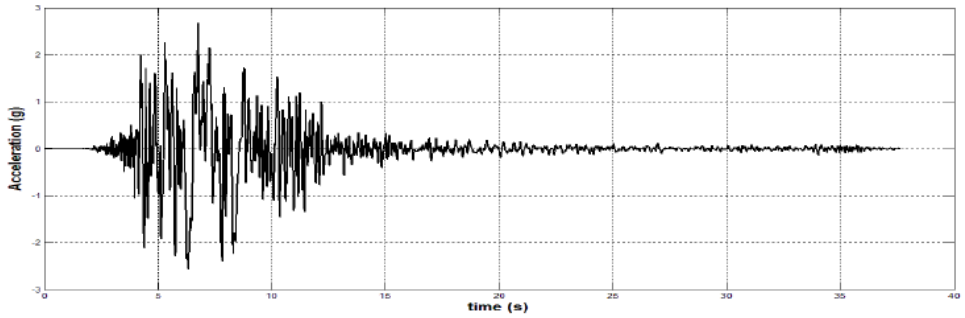

Figure 8.4 Final signal used for ULS

8.2. Serviceability Limit State (SLS)

The earthquake record and the velocity and displacement time histories for the 29th May 2012 East-West component are shown in Fig. 8.5.

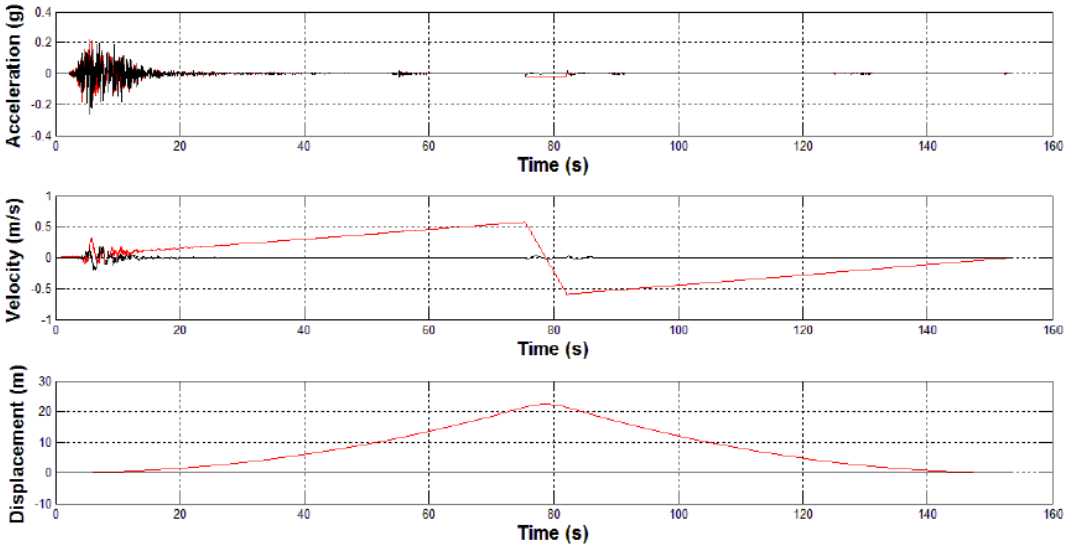

Figure 8.5 Final Record of the 29th May 2012 (W-E Component): acceleration (top), velocity (middle) and displacement (bottom) response histories

In the figure, the red line are the uncorrected signals, the black lines are the correct ones. The correction is achieved with a baseline correction on the acceleration profile and then it is applied a pass-band Butterworth filter in the interval [0.25 Hz - 25.0 Hz].

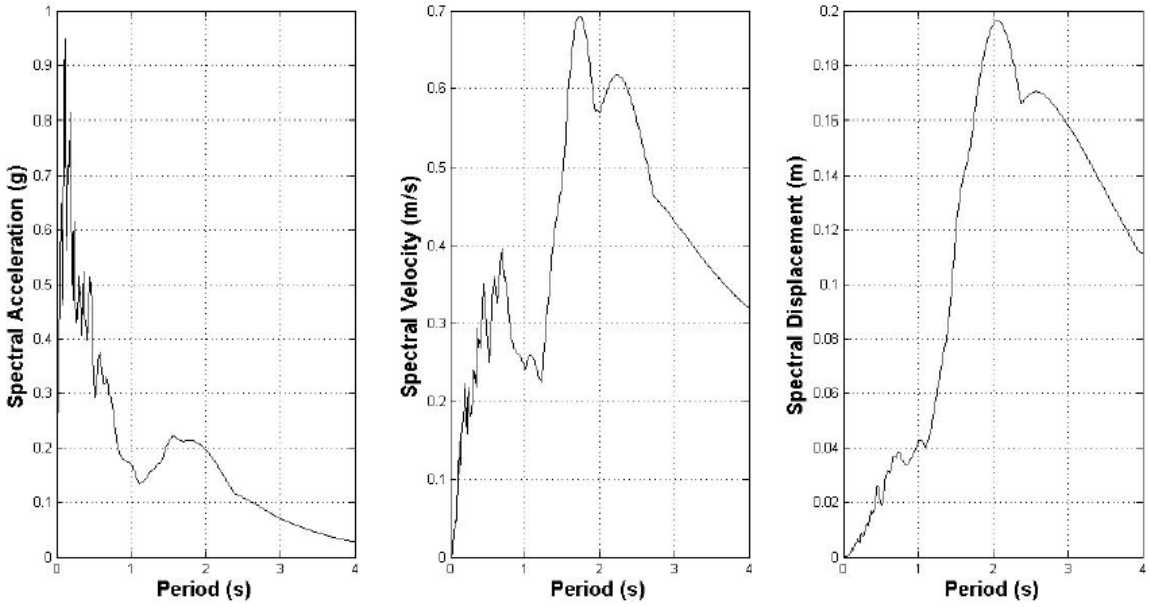

Figure 8.6 Response spectra of the record of the 29th May 2012 (East-West Component): acceleration (left), velocity (middle) and displacement (right) spectra

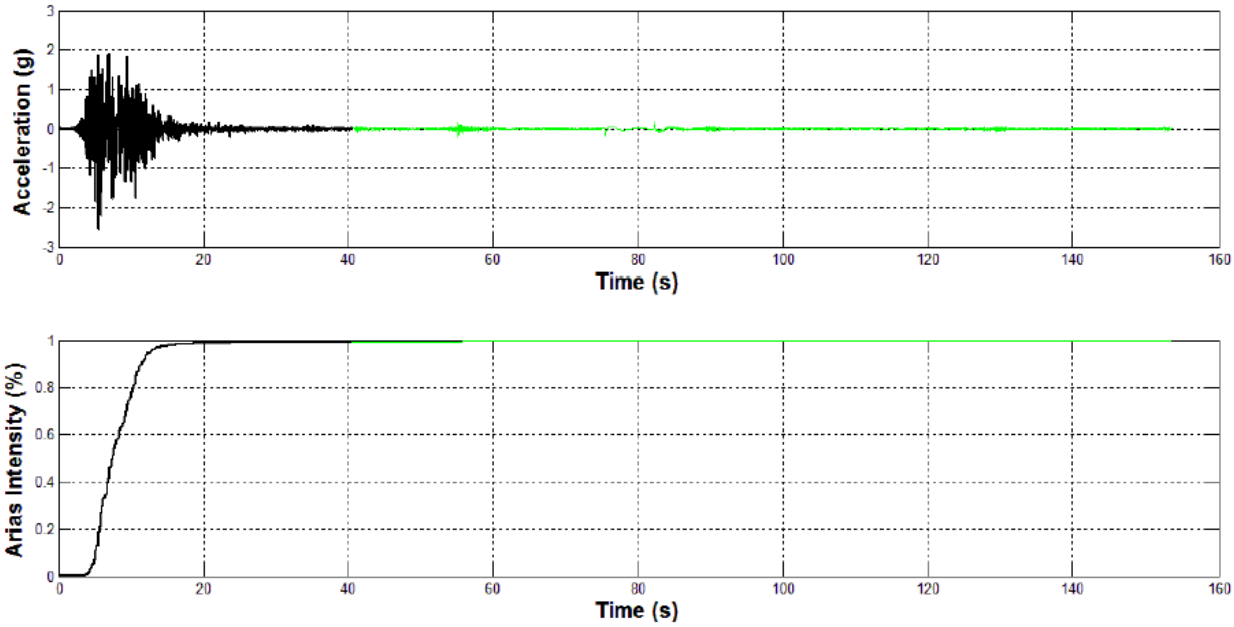

Figure 8.7 Reduction of the signal length

The response spectra of the sample record are provided in Fig. 8.6. It is observed a significant amplification for low-periods (between 0.5 and 1.0 seconds); values of spectral accelerations around 0.20g are also found in a period range 1-1.5 seconds, i.e. similar to the important natural periods of the part of the "as built bridge" in which pier 9 and 11 are located. The length of the signal was reduced to a significant length for which the Arias intensity is up to 99,4% (Fig. 8.7). The filtered signal is shown in Fig. 8.8.

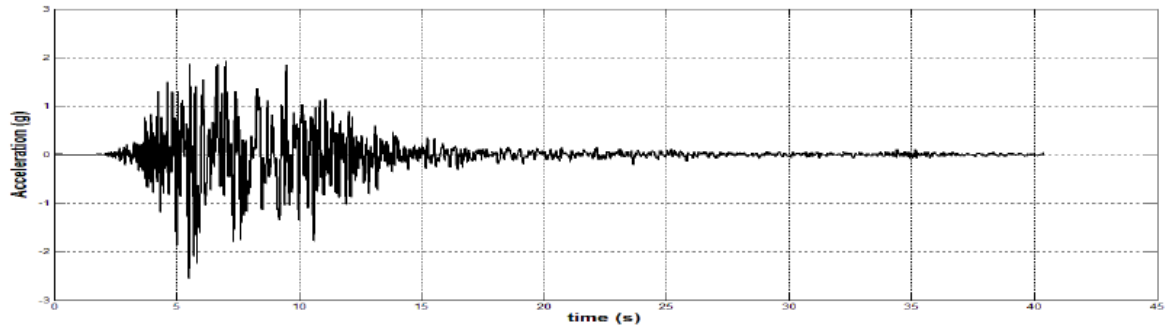

Figure 8.8 Final signal used for SLS

9. TESTING PROGRAM

Along the line of the PsD testing at JRC, the program was consequently subdivided in two groups of tests, one for the assessment of the seismic behaviour of the Rio-Torto viaduct as it is and the other one for the assessment of the effectiveness of FP bearings for its seismic protection. Table 9.1 shows the most significant tests performed during the PsD test campaign.

At the first phase of testing the entire control system is checked and a first characterization of the system is carried out, including the evaluation of the fundamental frequencies and the damping of the viaduct.

Following the check of the control system, a set of characterization tests of the cyclic behaviour of the FP bearings provided by ALGA S.p.A. was executed (*tests d03, m01*). The tests consist of harmonic displacements with different amplitudes, frequencies and axial forces. A minimum of three values of axial forces, frequencies and amplitudes were considered, for a total of 27 tests.

A static characterization of the two piers (initial stiffness) followed with an application of cyclic displacements at the top of the models (*tests f03, f04*). This phase aimed at providing the elastic stiffness of the two piers. In particular, a monotonic static displacement, including the corresponding unloading phase, was applied to each pier and the restoring force was measured. The maximum displacements applied to piers 9 and 11 were equal to 2 mm and 1.5 mm, respectively.

Subsequently, a dynamic characterization of the bridge using the SLS accelerogram with a low intensity level was performed (*test k06*). The goal of this phase was to define the dynamic characteristics of the bridge (fundamental frequency and damping). The excitation used was the East-West record of May 29th with an intensity level scaled to 0.01 g.

The first PsD test was performed on the entire bridge on the non-isolated condition, using the 100% East-West record of May 29th (PGA=0.25g). This test (*k07*) was planned to induce slight damage on the non-isolated piers (hairline cracks on the transverse beams and at the bottom section of columns), representative of low return period earthquakes.

Table 9.1 – List of significant tests performed during the RETRO test campaign

Name	Description	Parameters	Type of test	Physical Part
d03	Test on Isolator_P9	V = 450 kN D = 50,40,30,20,10mm	Cyclic displacements	Isolator_P9
f03	Preliminary test for the stiffness of pier 11	V = 450 kN D=1.5 mm	Cyclic displacements	Pier 11
f04	Preliminary test for the stiffness of pier 9	V = 450 kN D=2 mm	Cyclic displacements	Pier 9
k06	Non Isolated Bridge 10% SLS	PGA=10% SLS	PsD test	Pier 9 & 11
k07	Non Isolated Bridge 100% SLS	PGA=100% SLS	PsD test	Pier 9 & 11
m01	Only physical isolators	V = 450,225,175 kN, H = 30 mm, 1.88 mm/s,	Cyclic displacements	Isolator_P9 & P11
l01	Isolated Bridge case 100% SLS	PGA=100% SLS, μ=4% (design value)	PsD test	Pier 9 & 11
l02	Isolated Bridge case 100% ULS	PGA=100% ULS, μ=4% (design value)	PsD test	Pier 9 & 11
p01	Isolated Bridge case 100% SLS	PGA=100% SLS, μ=4% (design value)	PsD test	Pier 9 & 11 +Isolator_P9
p02	Isolated Bridge case 70% ULS	PGA=70% ULS, μ=4% (design value)	PsD test	Pier 9 & 11 +Isolator_P9 & P11
q01	Isolated Bridge case 100% SLS	PGA=100% SLS, μ=4% (design value)	PsD test	Pier 9 +Isolator_P9
q02	Isolated Bridge case 65% ULS	PGA=65% ULS, μ=4% (design value)	PsD test	Pier 9 +Isolator_P9
q03	Isolated Bridge case 2nd 65% ULS	PGA=65% ULS, μ=4% (design value)	PsD test	Pier 9 +Isolator_P9
k09	Not Isolated Bridge 100% ULS	PGA=100% ULS	PsD test	Pier9&11
r01	Isolated Bridge case 65% ULS	PGA=65% ULS μ=7% (actual value)	PsD test	Isolator_P9
r02	Isolated Bridge case 80% ULS	PGA=80% ULS μ=7% (actual value)	PsD test	Isolator_P9
r03	Isolated Bridge case 90% ULS	PGA=90% ULS μ=7% (actual value)	PsD test	Isolator_P9
k10	Aftershock - Non Isolated 100% ULS after test k09	PGA=100% ULS after a first run of 100%ULS (k09)	PsD test	Pier 9 & 11
k12	Aftershock - Non Isolated 200% ULS after test k10	PGA=200% ULS	PsD test	Pier 9 & 11

Afterwards, seismic tests of the isolated bridge in SLS and ULS conditions were performed, either with physical piers only (*tests l01 and l02) or with physical piers and isolators (tests p01 and p02*). Given that the cyclic tests on the FP bearings showed a friction coefficient of 7%, greater than the designed one of 4%, and that the isolators of pier 11 were working improperly, the tests were executed simulating in the numerical piers the presence of μ=4% and using only the physical isolators of pier 9 with a reduced vertical load to obtain a friction

force equivalent to μ=4%; for pier 11 the isolator was numerically simulated (tests q01, q02, q03). The effectiveness of the FP bearings in protecting the bridge was demonstrated with the presence of (almost) a linear behaviour of physical as well as numerical piers for the SLS condition and with the presence of a limited damage condition experienced both by the physical as well as the numerical piers for the ULS condition. Since the isolator shows different behaviour than the designed one, three reduced signal tests on just the physical isolator of the pier 9 configuration with full vertical load were carried out. The three tests consider 65%, 80% and 90% reduction of the ULS signal, respectively. The effectiveness of the physical FP bearings in protecting the bridge were evaluated in the different cases of reduction signals (*tests r01, r02, r03*).

Finally, to ascertain the seismic vulnerability of the non-isolated bridge a seismic test of the non-isolated bridge using the North-East record of May 29 with PGA=0.27g (ULS) was carried out (*tests k09*). In this phase, piers 9 and 11 experienced significant levels of damage (extensive crack pattern in the beams, crack opening at the base and at the top section of the columns) as already foreseen by previous numerical simulations. The seismic test of the non-isolated case for the 100% ULS accelerogram was repeated in order to demonstrate the aftershock effects on the already damaged bridge (*test k10*). Finally, a seismic test on the non-isolated bridge for beyond-design condition using a 200% ULS accelerogram was executed (*test k12*).

10. EXPERIMENTAL RESULTS

According to the testing program presented above, in what follows the main results for each test phase will be presented and commented. In particular, the main results on the characterization of the isolators and of the single pier specimens will be firstly introduced. After that the results of the PsD test on the non-isolated and isolated configurations will be presented. Given that during the characterization of the isolators a higher friction coefficient was measured, the PsD test on the isolated configuration was executed using a combination of numerical and physical isolators.

10.1. Cyclic characterization of the FPS isolator

In order to characterize the cyclic behaviour of the isolators, several tests were performed (not indicated in Table 9.1): a first group of tests taking as a guide the paper by Lomiento et al. [62], (*tests b22, b23*), and a series of cyclic test with variable velocities and amplitudes.

10.1.1. Cyclic tests following the Lomiento et al. procedure

The testing protocol used in the paper of Lomiento et al. consisted of two sinusoidal cycles of 200 mm amplitude, repeated at different velocities (peak velocity of the sinus ranged between 0.25 and 1000 mm/s) with a constant vertical load. Between every two-wave pattern and the following, a certain waiting time was imposed in order to avoid overheating of the device. The authors conclude that the friction coefficient of the isolators is mainly affected by:

1. a “load effect”: The friction coefficient diminishes with the applied vertical load. This effect exists in similar amount at all the velocities for which it can be fully described without need to perform fast tests.
2. a “cycling effect”: The friction coefficient is smaller at the second consecutive cycle due to the temperature rise and this is more visible at higher velocities (over 10mm/s).
3. a “velocity effect” that increases the friction coefficient at higher velocities. However this effect is sometimes hidden by the cycling (heating) effect that diminishes the friction.

4. a “breakaway effect” or stick-slip effect that introduces a peak of the friction at the top and bottom of the sinus wave when the velocity is null (static friction coefficient). This last effect does not affect much the energy dissipation of the force-displacement cycle, but may dangerously modify the force demand on the isolated structure.

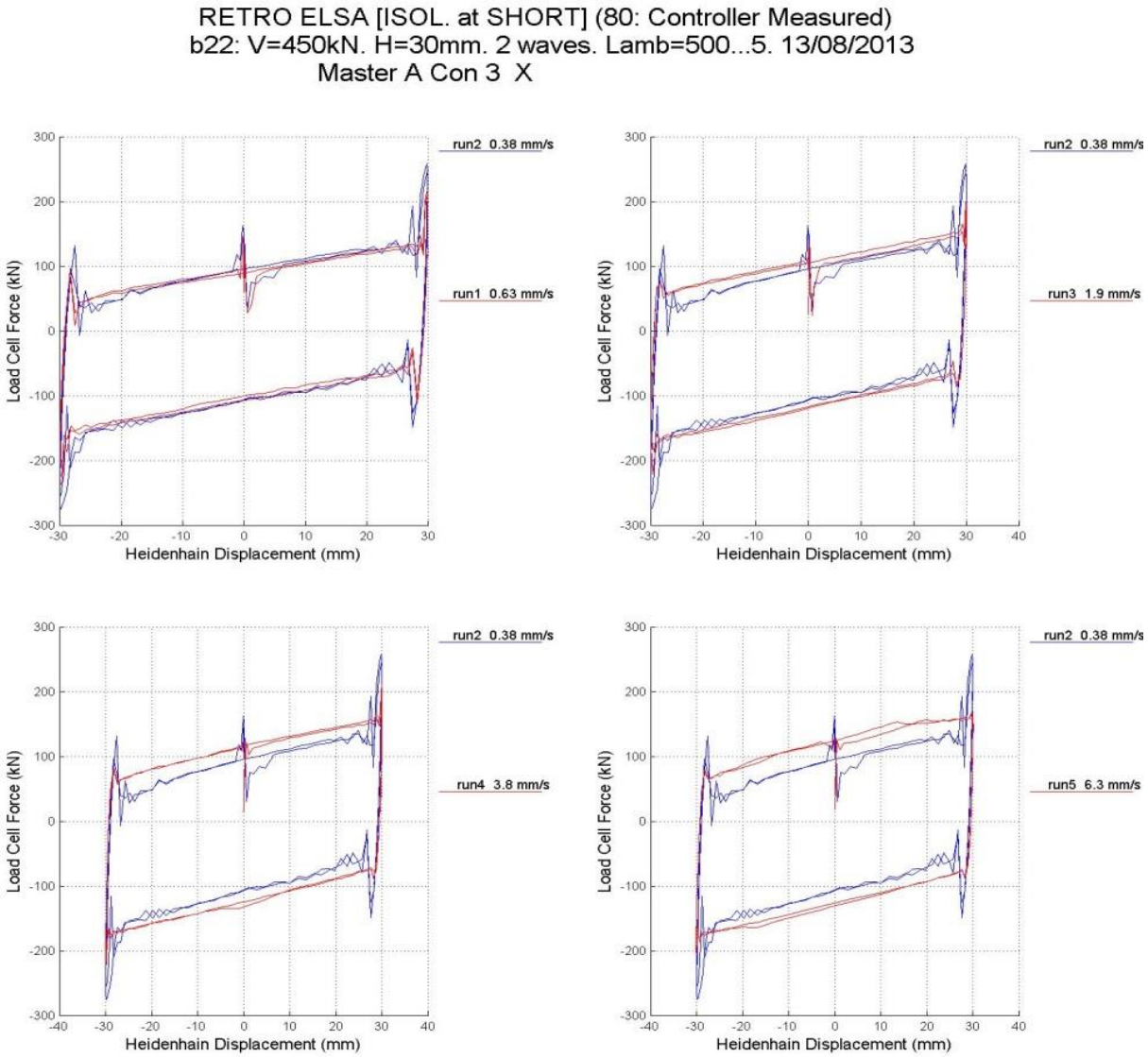

Fig. 10.1 Sinusoidal test comparisons of runs at different velocities - *Test b22*

Having in mind that in the RETRO test campaign the isolators can be different from the ones used in the paper, similar experiments were carried out within the range of the capacity of the setup.

In Fig. 10.1, the force-displacement loop at 0.38 mm/s is compared with loops at 0.63, 1.9, 3.8 and 6.3 mm/s, showing an increase of the friction at higher velocities. However, the cycling effect is not significantly observed for these velocities. Regarding the breakaway

effect, it is quite limited for 6.3 mm/s, and becomes stronger at slower speeds, even though it does not seem to affect the dissipated energy. As a difference with respect to the results shown in the mentioned paper, the breakaway effect is observed here double (not only when accelerating from zero, but also when decelerating to zero). The explanation for this may lay on the control characteristics. A similar test (test b23), with similar conclusions, was performed using as random pattern a time-history of displacement coming from a numerical simulation performed using the North-South 29 May record (ULS). An example of a random cycle is shown in Figure 10.2.

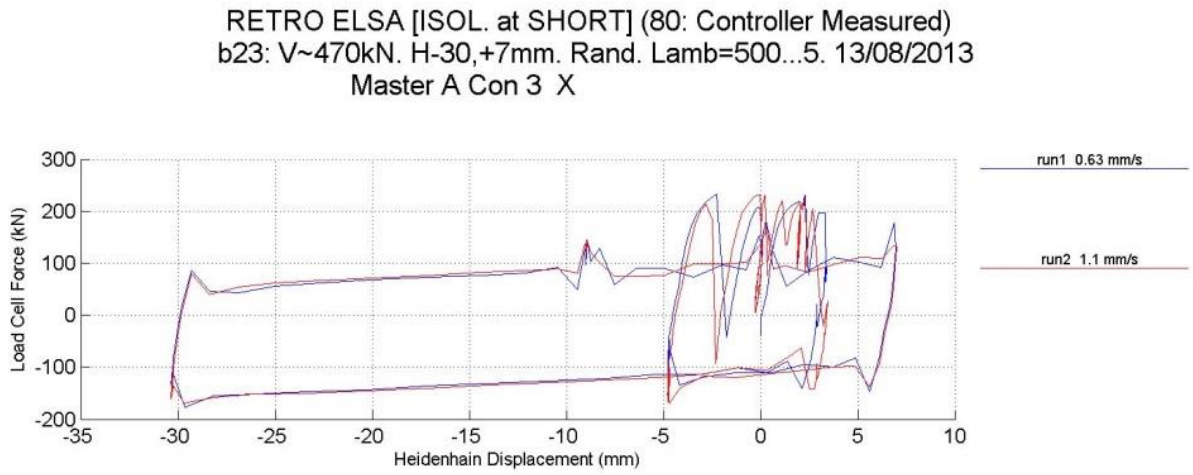

Fig. 10.2 Random test comparisons of runs at different velocities - *Test b23*

10.1.2. Tests for different cycling velocities and amplitudes

Two types of cyclic tests that were repeated in identical conditions for both isolator setups with a constant vertical load of 450 kN per isolator were performed and compared. The first comparison regards tests b16 and d03 concerning respectively the isolators at the short and tall piers, in which runs of five sine cycles at a constant frequency of 1/100 Hz were imposed with amplitudes of 50, 40, 30, 20 and 10 mm. The maximum velocity at every amplitude ranged from 3.14 to 0.63 mm/s.

The cycles for the magnitudes in the scale of the laboratory and regarding the total horizontal force applied by the horizontal actuator on four isolators with respect to the common horizontal displacement are shown in Fig. 10.3 (for the isolator setup at the short pier) and in Fig. 10.4 (for the isolator setup at the tall pier).

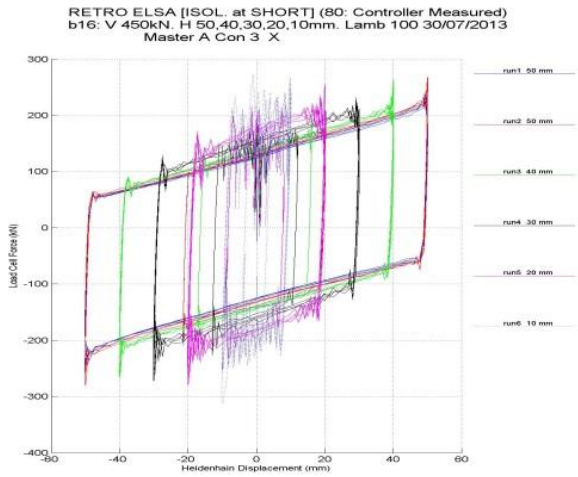

Fig. 10.3 Test at variable amplitude, Isolator setup at short pier - *Test b16*

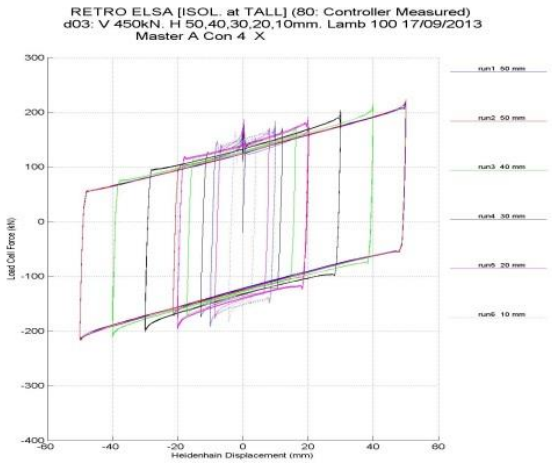

Fig. 10.4 Test at variable amplitude, Isolator setup at tall pier- *Test d03*

A second comparison regarded the tests on isolators at the short (b22) and tall piers (d02) in which trains of two sine cycles at a frequency varying between 1/500…1/5 Hz were imposed with a constant amplitude of 30 mm. The maximum velocity at every frequency ranged from 0.63 to 37.7 mm/sec. However, due to the limitations of the testing setup at higher velocities, only the first five runs with frequencies of 1/500 to 1/30 Hz can be considered as valid for the analysis. The cycles obtained are shown in Figure 10.5 and 10.6 for the isolator setup at the short and tall piers, respectively.

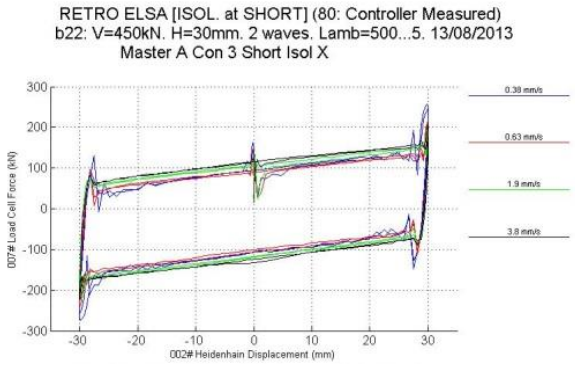

Fig. 10. 5 Test at variable frequency, Isolator setup at short pier - *Test b22*

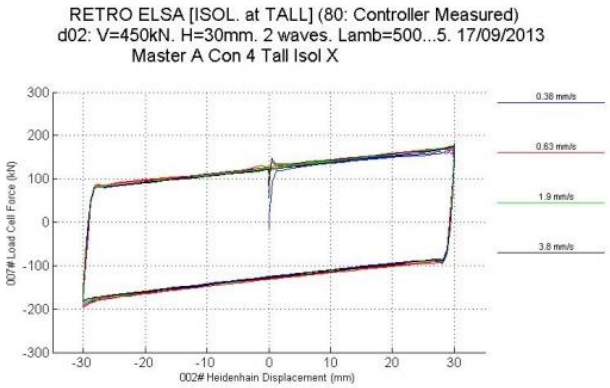

Fig. 10.6 Test at variable frequency, Isolator setup at tall pier - *Test d02*

10.2. Static characterization of the specimens

The first tests performed on the piers at ELSA served for the identification of the initial stiffness as well as for the tuning of the PID control parameters of the actuators. In test f03,

sine cycles of 1.5 mm were applied to the short pier, whereas in test f04, sine cycles of 2 mm were applied to the tall pier.

At the beginning of every test, the vertical load was gradually applied by the vertical actuators controlled in force. At every one of the two columns of the pier, the vertical actuator maintained a force of 450 kN that was constant during the imposition of the horizontal cycles. Several runs of two consecutive horizontal cycles, for the specified constant amplitude were imposed at the head rig of the pier. Eventually, the parameters of the PID controller for the horizontal actuator were changed at every run in order to show the possible effect in the quality of the control. By taking a complete single cycle of the significant runs from both tests, the equivalent linear stiffness and equivalent-viscous damping ratio were identified as shown in Table 10.1 following a standard procedure implemented at ELSA.

Tab. 10.1 Results of the static characterization of specimens

PIER	***test***	***run***	**Amplitude (mm)**	**Stiffness(kN/mm)**	**Damping ratio**
short	*f03*	*3*	1.5	11.03	0.0366
short	*f03*	*4*	1.5	11.01	0.0364
short	*f03*	*5*	1.5	11.00	0.0363
tall	*f04*	*1*	2	7.398	0.0393
tall	*f04*	*2*	2	7.341	0.0327
tall	*f04*	*3*	2	7.315	0.0286

Fig. 10.7 and 10.8 show the force-displacement loops at one of the runs of Table 10.1 for piers 9 and 11 by taking the average of the displacement along the axes of both horizontal actuators of each pier and the total force applied by them.

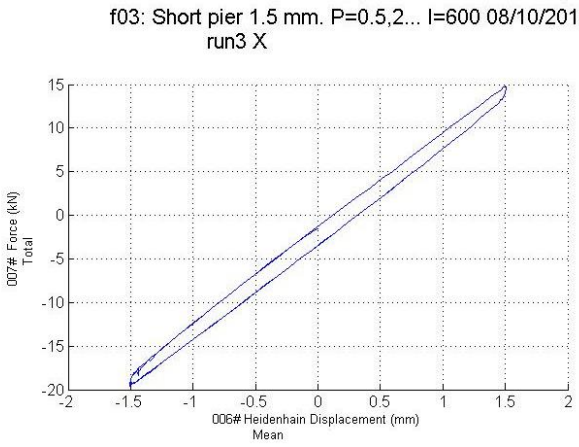

Fig. 10.7 Force-displacement loops for short pier - *Test f03*

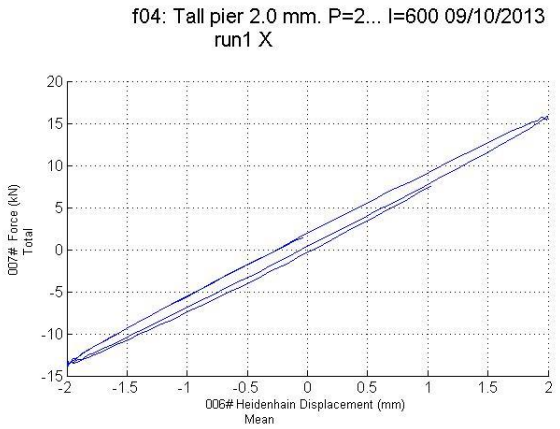

Fig. 10.8 Force-displacement loops for tall pier *Test f04*

10.3. PsD test results on the entire viaduct

In this section the results of the PsD test on the entire isolated and non-isolated bridge are presented. The results are presented in terms of global quantities as displacement at the top of each pier and base shear, or in terms of local quantities measured in the specimens during the tests (curvatures or shear deformations, level of bond slip of bars, etc.). The global displacement of the piers is the average of the two horizontal actuators of the pier at the head rig. The represented force is not exactly the total force obtained by the addition of the forces at both actuators. In fact, the figures give the net total force on the pier, which is equal to the total force after removing the recentring horizontal force given by the tensioned dywidag bars inside of the columns of the pier, i.e.,

$$F_{Total}^{Net} = F_{Total} + K_{Geom} D \tag{10.1}$$

where a geometric stiffness K_{Geom} (at the laboratory model scale), multiplies the horizontal displacement in order to provide the correction term.

For tests with large displacements k09, k10 and k12, the same kind of correction was used within the PsD algorithm before these forces were introduced as restoring forces within the equation of motion, taking the values of geometric stiffness provided in Table 10.2 (at the prototype scale in this case).

Tab 10.2 Geometric stiffness applied at piers

Laboratory model scale values		
Pier	Short (11)	Tall (9)
Height from basement bottom to vertical cylinder bottom H (m)	8	12.5
Total vertical load V (N)	9E+05	9E+05
Geometric stiffness –V/H (N/m)	-112500	-72000
Prototype scale values		
Pier	Short (11)	Tall (9)
Height from basement bottom to vertical cylinder bottom H=2.5*H (m)	20	31.25
Total vertical load V=2.5*2.5*V (N)	5625000	5625000
Geometric stiffness –V/H=–2.5*V/H (N/m)	-281250	-180000

10.3.1. PsD test results on the non-isolated viaduct

Test *k06* test was executed to check all instruments, Extensimeter sensors and hydraulic actuators, in addition to get an indication of the level of displacements and initial stiffness of the piers.

In test k07 the 100% SLS earthquake was applied on the as-built configuration; the curvature at the bottom section of one of the columns of pier 11 is shown in Figure 10.9. It demonstrates the slight amount of non-linearity in the columns during the test.

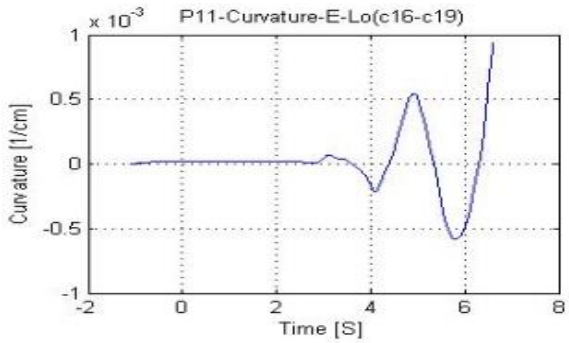

Fig. 10.9 – Curvature at the bottom section of the left column of pier 11 for *test k07*

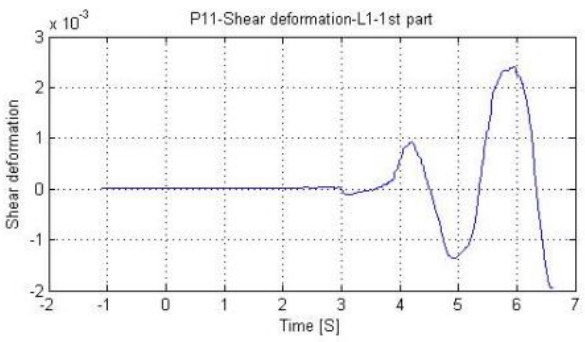

Fig. 10.10 – Shear Deformation in the transverse beam for *test k07*

In test *k07*, the global behaviour goes beyond the elastic limit, corresponding to the formation of hairline cracks due to shear damage at the transverse beam of piers 11 and 9; to avoid excessive damage in pier 11 the test was stopped at 6.6 s. In fact, the predicted level of displacement for a slight damage condition was about 3 cm for the tall pier and 1.6 cm for the

short one: during the test the short pier reached a displacement of about 3 cm. This was mainly due to the excessive deformability of pier 11 with respect to the design values. The crack pattern observed after the test was very close to that predicted using the refined model, for which the maximum expected level of shear deformation γ was about 1×10^{-3}, very close to the obtained one.

The experimental curvature χ was evaluated in the as-built configuration with the equation $\chi = (\delta_1/B_1+\delta_2/B_2)/D$ as a function of displacements δ_1, δ_2 and include the slippage effect of rebars. δ_1 and δ_2 were measured by pairs of extensometers at a distance B_1 and B_2 with respect to the base (Fig. 10.12).

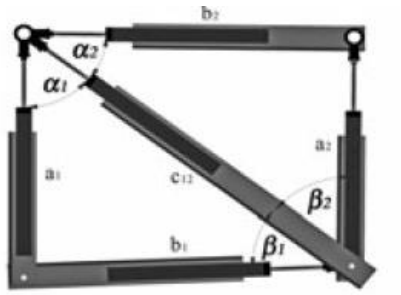

Fig. 10.11 Parameters for the evaluation of the shear deformation

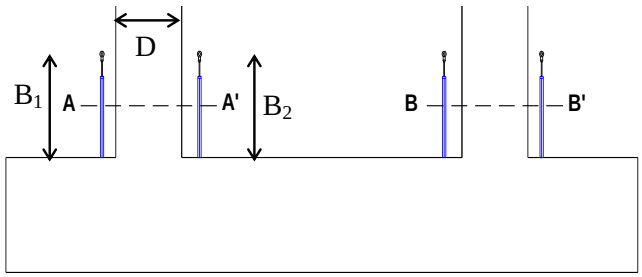

Fig. 10.12 Parameters for the evaluation of the curvature in the columns

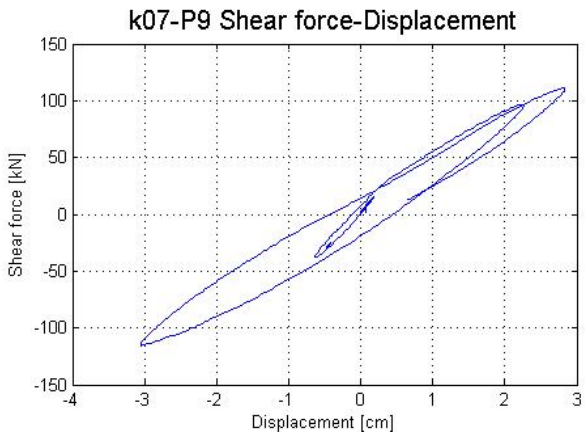

Fig. 10.13 – Force-Deflection cycle of Pier 9 (SLS PGA=100%) - *Test k07*

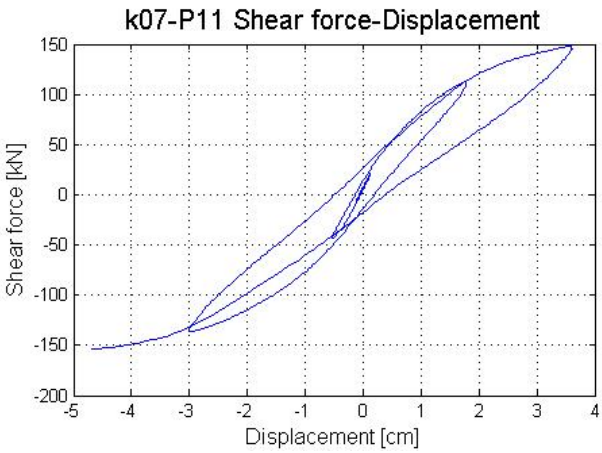

Fig. 10.14 – Force-Deflection cycle of Pier 11 (SLS PGA=100%) - *Test k07*

The evaluation of the mean value of shear deformation γ may be performed as $\gamma=(\Delta\alpha+\Delta\beta)/2$, whose symbols are indicated in Figure 10.11, where the arrangement of the sensors used is

also shown. $\Delta\alpha = \alpha_0 - (\alpha_2+\alpha_1)$ and $\Delta\beta=\beta_0 - (\beta_2 +\beta_1)$ are the variation of the angles $\alpha=\alpha_2+\alpha_1$ and $\beta=\beta_2 +\beta_1$ with respect to the initial ones α_0 and β_0.

Similarly, a slight crack at the bottom section of piers 9 and 11 was detected as evidenced by the bond slip measured by the extensimeter sensors placed at bottom of the columns. The maximum level of displacement was of the order of 0.2 mm, corresponding to a slight crack opening in the column.

The configuration of the non-isolated viaduct was tested at the *k09 test* considering the 100% ULS earthquake. In this test, a significant shear crack pattern was observed in both piers in the transverse beams, in addition to some cracks between the cap beam and the column joints. Base-column opening was also evident during the cycles. Fig. 10.15 and Fig. 10.16 show the force-deflection cycles, showing the high non-linearity developed by both piers.

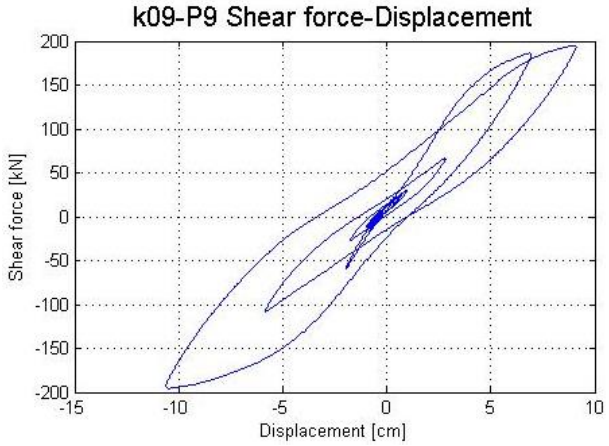

Fig. 10.15 – Force-Deflection cycle of Pier 9 (ULS PGA=100%) - *Test k09*

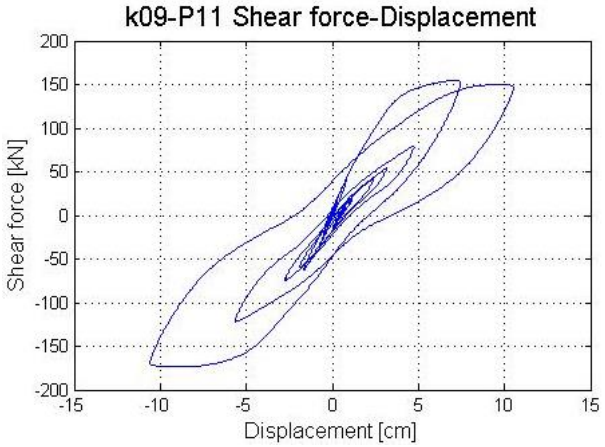

Fig. 10.16 – Force-Deflection cycle of Pier 11 (ULS PGA=100%) - *Test k09*

The shape of cycles confirm the results obtained during the test campaign carried out at University Roma Tre on 1:4 scale models of pier 12 (similar to pier 11) [17]. In fact, beyond the high deformability of both the piers, the absence of softening characterizes their cyclic behaviour, even for high levels of displacement.

A pronounced pinching phenomenon is also observed. This is mainly due to shear damage in the transverse beams and the large crack opening at the base of columns and the consequent fix-end rotation effect, which is characterized by an alternate closing and opening of cracks and, accordingly, the increase and decrease of stiffness. Similar phenomena can be noticed in the other piers, here simulated only numerically (Fig. 10.17a). The time history of displacements at the top of each pier is shown in Fig. 10.17b.

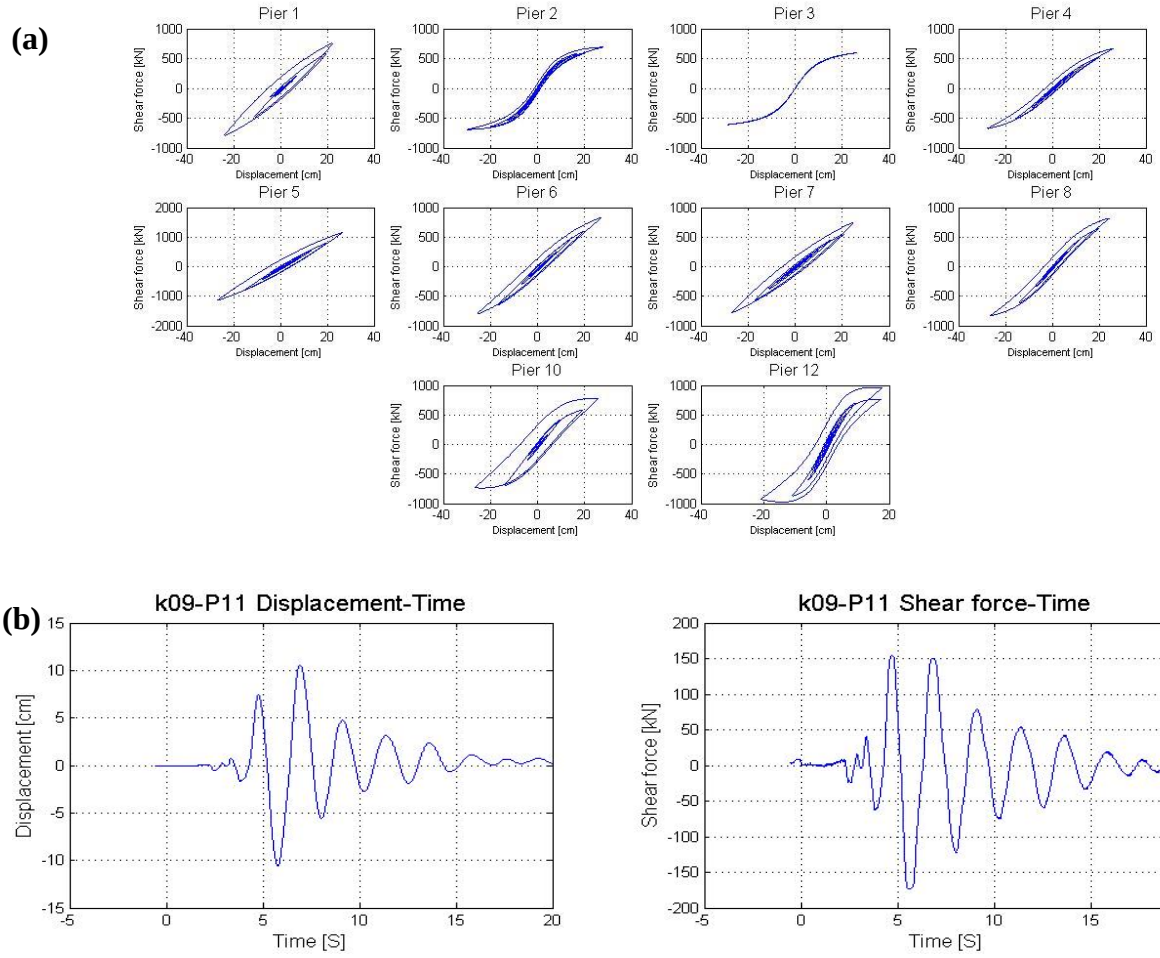

Figure 10.17 – (a) Cycles of the remaining (numerical) piers (b) Displacement T-H– *Test k09*

Fig. 10.18 Shear cracks pattern in the transverse beam of pier 11 after test k09

The high level of shear damage in the beams and the large amount of crack opening at the base and top of the column is clearly shown in Fig. 10.18 and Fig. 10.19.

In order to assess aftershock effects on the already damaged bridge an exact repetition of *test k09* was carried out (*test k10*). The test aimed at verifying the level of degradation of non-

linear behaviour and the level of damage of both piers. In addition, this will allow to verify the reliability of the adopted non-linear models in predicting the seismic behaviour of the damaged bridge under aftershocks.

Fig. 10.19 Crack opening at the top and bottom of pier 11 after test k09

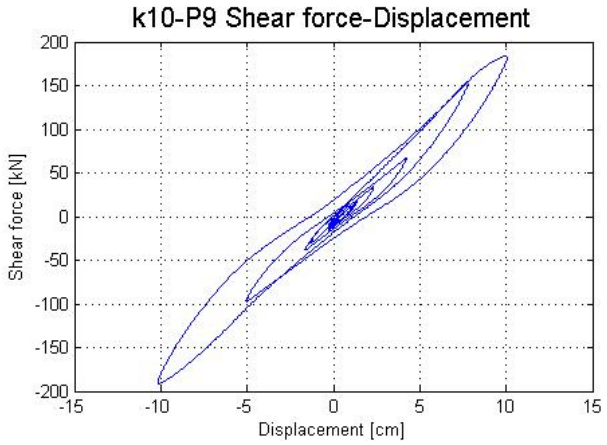

Fig. 10.20 – Force-Deflection cycle of Pier 9 - *test k10* (Aftershock PGA=100%)

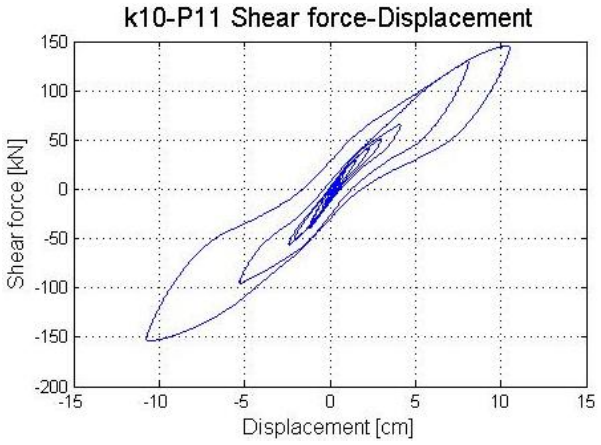

Fig. 10.21 – Force-Deflection cycle of Pier 11 - *test k10* (Aftershock PGA=100%)

From the test results (see Fig. 10.20 and Fig. 10.21), it can be noticed a general decrease of stiffness due to the increase of the fix-end rotation effect, given by the high slippage of the reinforcing bars at the top and bottom sections of columns. This effect was amplified by large openings of shear cracks in the transverse beams.

Finally, to test the piers in beyond-design conditions and quantify global failure in terms of local and global response, a test with PGA=0.54g (200% ULS) was performed. It is useful to remind that in literature [63], the drift in shear failure condition of the transverse beams is 2%.

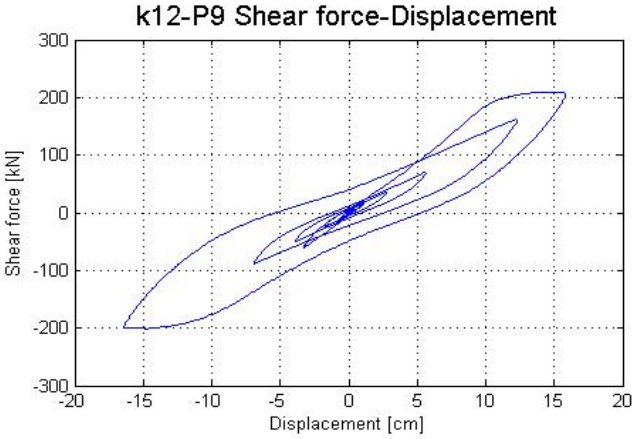

Fig. 10.22 – Force-Deflection cycle of tall Pier for *test k12* (PGA=200%)

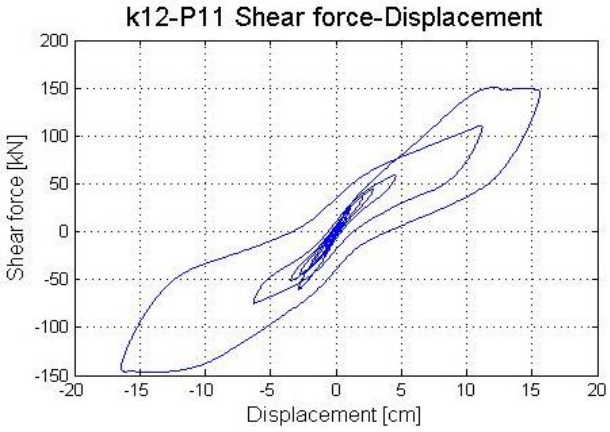

Fig. 20.23 – Force-Deflection cycle of Pier 11 for *test k12* (PGA=200%)

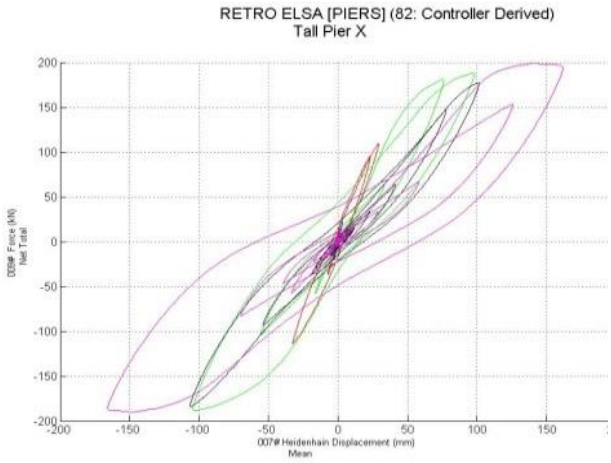

Fig. 10.24 – Force-Deflection cycles of Tall Pier for various level of testing – non-isolated bridge

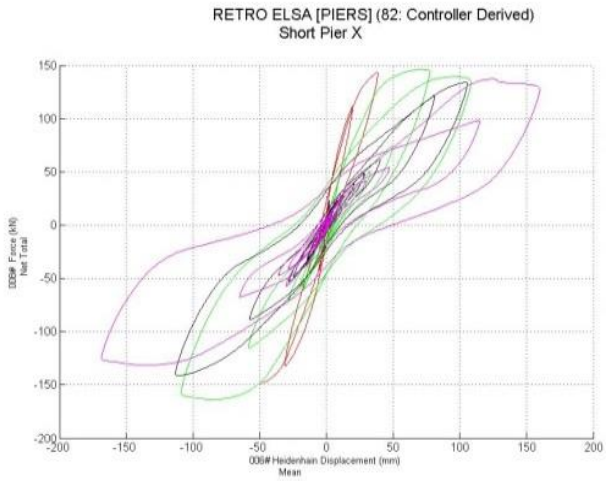

Fig. 10.25 – Force-Deflection cycles of Short Pier for various level of testing – non-isolated bridge

The hysteretic cycles are shown in Fig. 10.22 and Fig. 10.23. Failure of the pier is confirmed by the maximum drift of 2.4% reached by the short pier. In fact, from the photos shown in Fig. 10.26 through Fig. 10.30 it is possible to observe an extensive damage condition both for pier 9 and 11, even though the most important damage pattern was experienced in the short pier, especially in the transverse beam, whose typical shear cracking pattern is shown in Fig. 10.26. A wide zone of cover spalling, characterized by an important buckling effect of the steel bars in the transverse beam of short pier is shown in Fig. 10.28. A similar effect, even though less important, was present in the transverse beam at the first transverse beam of the tall pier (Fig. 10.29). In fact, only a drift of 1.2% was imposed, corresponding to a severe

framework of damage in the transverse beam but far from the ultimate condition. The time-history of shear deformation is shown in Fig. 10.31, which confirms the above assertions.

This test has also been useful to better appreciate the presence of the fix-end rotation phenomenon. In fact, a very large crack opening at the bottom section of all columns was noticed (Fig. 10.30 b,c). In addition, given the high level of imposed displacements, a slight buckling effect at the left column base of the short pier also took place (Fig. 10.30a). The curvature history of the left column of both piers is shown in Fig. 10.31. There it can be noticed the high level of non-linearity given a level of curvature higher than the yielding limit.

Fig. 10.26 Transverse beam damage on pier 11 after *test k12*

Fig. 10.27 Crack opening at the top of a column in the Short pier after *test k12*

Fig. 10.28 Blow up of the transverse beam damage on short pier after *test k12*

Fig. 10.29 Crack pattern in the first transverse beam of tall pier after *test k12*

All previous cycles are superimposed in Fig. 10.24 and Fig. 10.25; they demonstrate the global stiffness decreasing effect due to the slippage of plain bars and the consequent fix-end

rotation phenomenon. The large non-linear deformations experienced by the other piers are shown in Fig. 10.32.

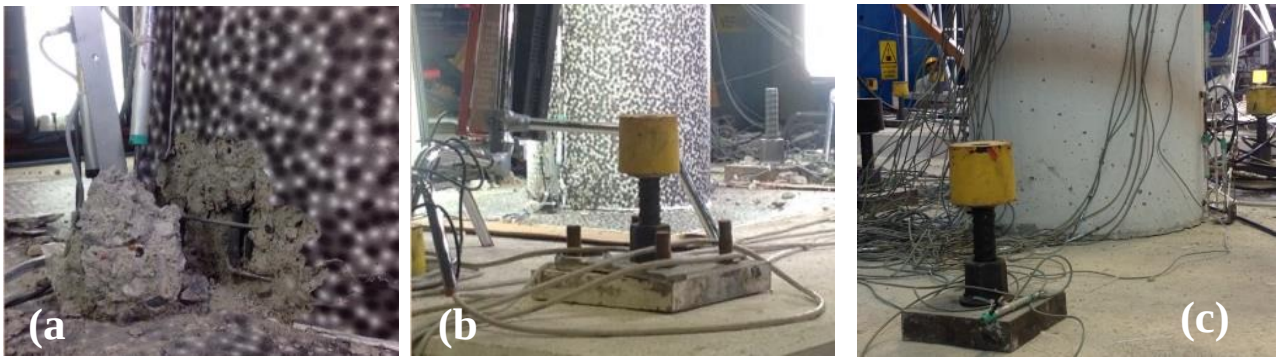

Fig. 10.30 Crack opening and buckling phenomena at the bottom section of columns in the Short (a,b) and Tall pier (c) after *test k12*

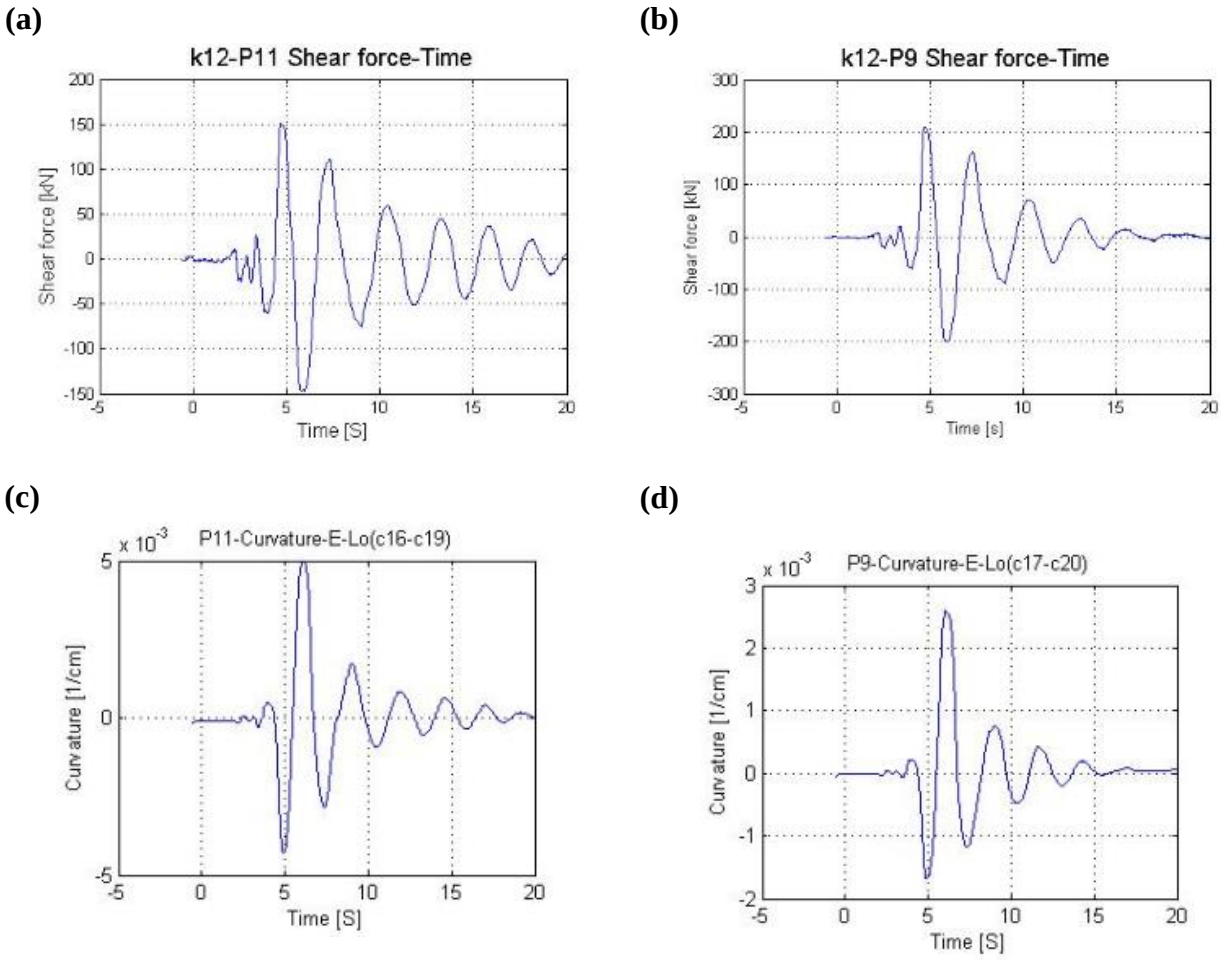

Fig. 10.31 Time-History of the shear deformation at transverse beam of Tall (a) and Short pier (b), curvature at bottom section of left column of Tall (c) and Short pier – 200% ULS

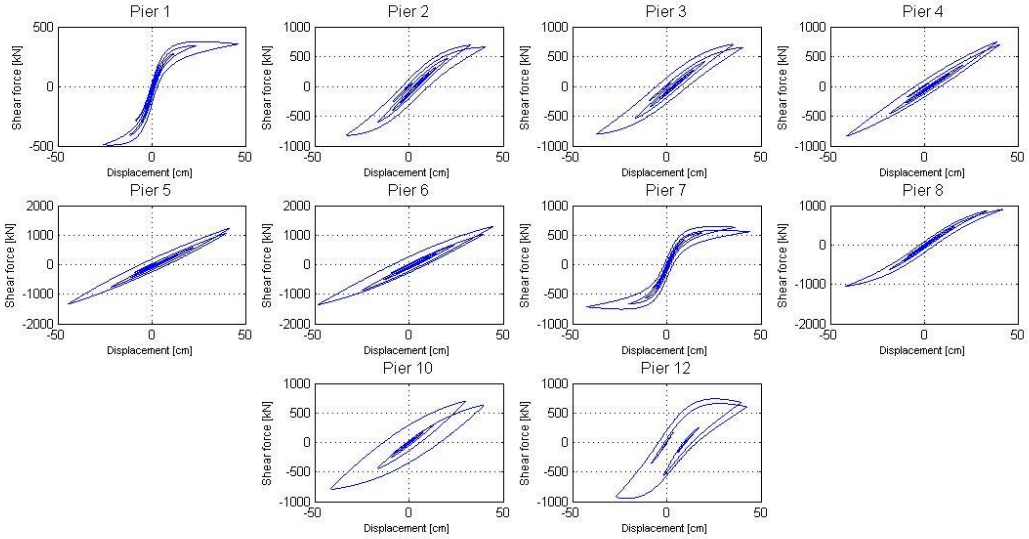

Fig. 10.32 Hysteretic cycles of numerical piers – 200% ULS

10.3.2. PsD test results on the isolated viaduct

Several PsD tests were carried out on the isolated viaduct at SLS and ULS. Design and actual values of friction μ for the friction pendulum devices, namely μ = 4% and μ = 7%, were considered along with the numerical and physical piers, respectively. During some of the tests with physical isolators (tests q01, q02 and q03), only the isolators connected to pier 9 (tall pier) were used as physical devices (with a reduced vertical load), as the set of devices connected to pier 11 exhibited an irregular hysteretic response, as discussed in Section 10.1. Both physical piers and both physical isolators (with a reduced vertical load) were considered only for tests *p01* and *p02*, corresponding to the 100% SLS and 70% ULS, respectively. Additionally, only the physical piers were tested for the experiments l01 and l02, corresponding to the 100% SLS and 100% ULS, respectively. These latter tests employ the design value of friction, i.e. 4%, for the numerical isolators. The bridge deck was assumed continuous, i.e. the saddles were eliminated when the isolation system was introduced at the base of the RC deck.

The bridge piers respond elastically when considering the 100%SLS as earthquake input. For example, Fig. 10.33 and Fig. 10.34 compare the force-deflection cycles of piers 9 and 11 during tests *l01* and *k07*, i.e. considering the bridge system with and without friction isolators,

respectively, having only two physical piers in the experiment. The effectiveness of the FP bearings in protecting the bridge was proved by (almost) linear behaviour of the physical as well as of the numerical piers at SLS. Transverse beams also exhibited an elastic response at serviceability limit state, as shown by the shear deformation in the lower transverse beam of pier 11 during test l01. The outcomes of the non-isolated bridge, i.e. test *k07*, have also been included as a benchmark. The initial stiffness shown in test k07 is larger because it was performed before test l01 . The linear elastic response of the piers stems also from the curvature at the bottom section of left column of pier 11 during test *l01*, and from the shear deformation, as depicted in Fig. 10.35 and Fig. 10.36. The hairline cracks on the transverse beams and at the bottom section of columns which appeared in the non-isolated configuration, namely in test *k07*, were not visible when base isolation devices were employed, i.e. for test *l01*.

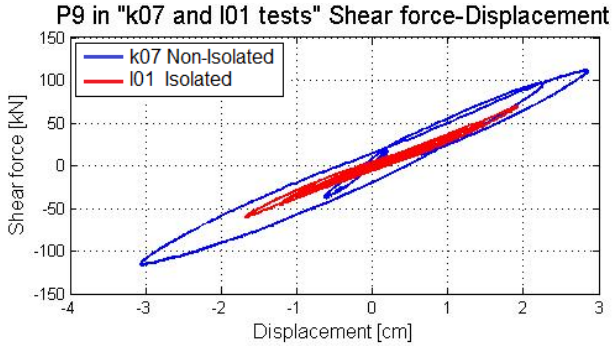

Fig. 10.33 – Force-Deflection cycle of Pier 9 during tests k07 and l01 (SLS PGA=100%)

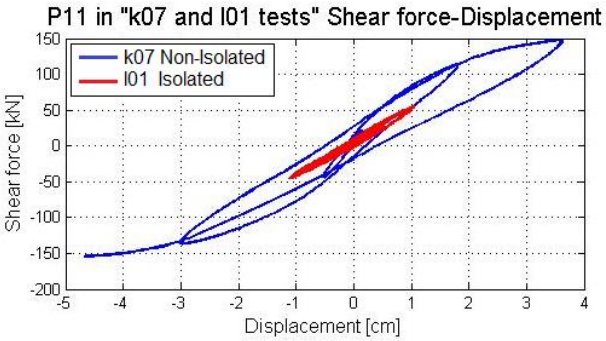

Fig. 10.34 – Force-Deflection cycle of Pier 11 during tests k07 and l01 (SLS PGA=100%)

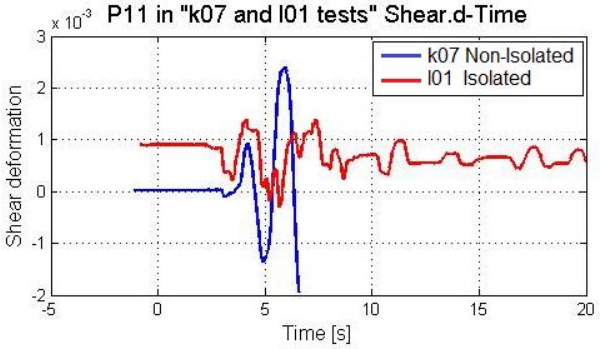

Fig. 10.35 – Shear Deformation in the lower transverse beam of pier 11 during tests k07 and l01 (SLS PGA=100%)

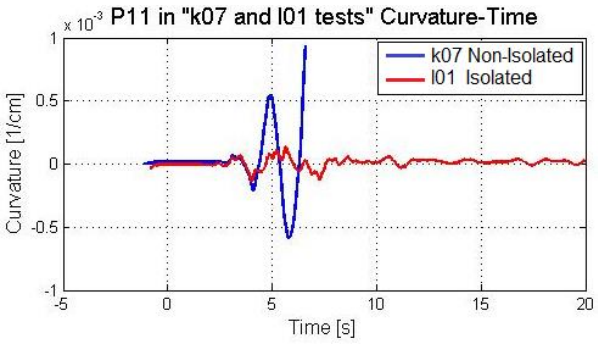

Fig. 10.36 – Curvature at the bottom section of left column of pier 11 during tests k07 and l01 (SLS PGA=100%)

The bridge configuration comprising physical piers (9 and 11) and physical isolators for piers 9 and 11 with emulated μ=4% was tested firstly under 70% ULS. The retrofitting system was implemented on a bridge possessing slight damage (100% SLS previous event). The response is nearly elastic, as shown in Fig. 10.37 and Fig. 10.38, where the force-deformation curves are plotted for the short and tall piers, respectively. The response of the transverse lower beam, measured through the shear deformations provided in Fig. 10.39, is also linear. The flexural curvature computed at the bottom section of the left column of pier 11 during test *p02* is also linear, as shown in Fig. 10.40.

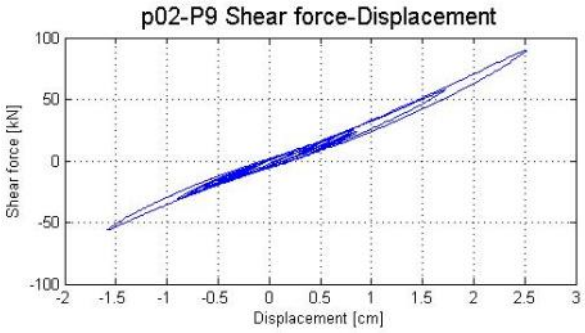

Fig. 10.37 – Force-Deflection cycle of Pier 9 during test p02 (ULS PGA=70%)

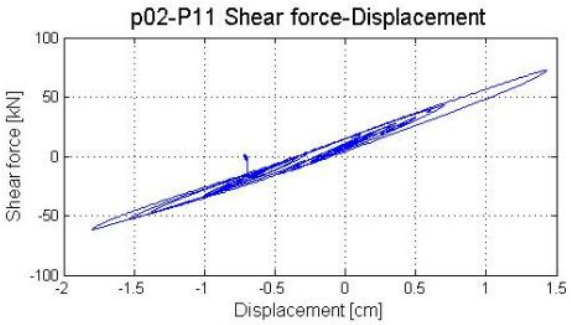

Fig. 10.38 – Force-Deflection cycle of Pier 11 during test p02 (ULS PGA=70%)

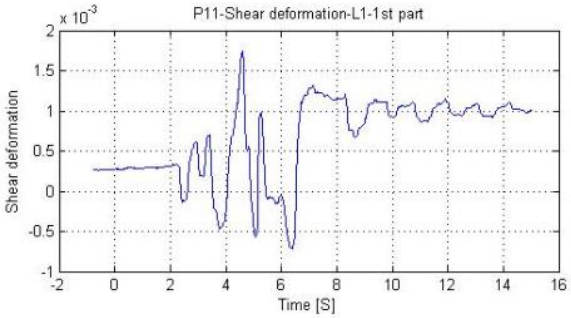

Fig. 10.39 – Shear Deformation in the lower transverse beam of pier 11 during test p02 (ULS PGA=70%)

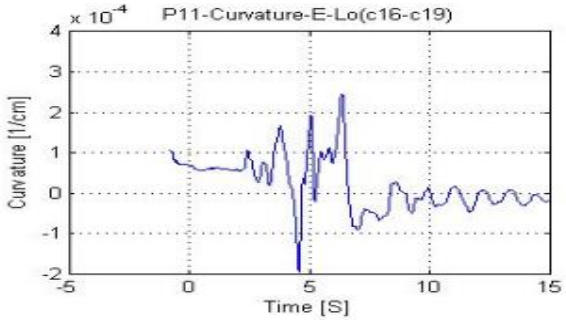

Fig. 10.40 – Curvature at the bottom section of left column of pier 11 during test p02 (ULS PGA=70%)

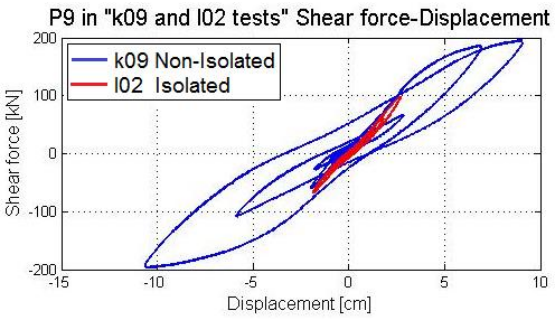

Fig. 10.41a – Force-Deflection cycle of Pier 9 during test k09 and l02 (ULS 100%)

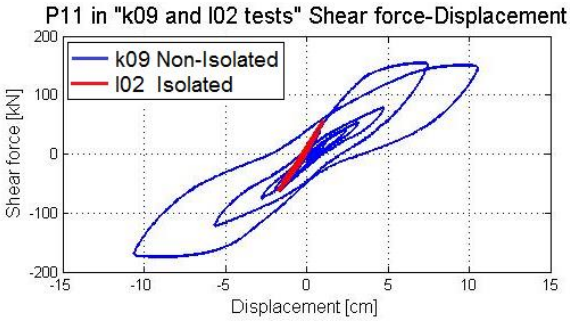

Fig. 10.41b – Force-Deflection cycle of Pier 11 during test k09 and l02 (ULS 100%)

The effectiveness of the FPS isolators can be fully observed by comparing the isolated and non-isolated case at 100% ULS (*k09* in the as-built and *l02* in the isolated case); Fig. 10.41 show the experimental force-deflection curves of Pier 9 and 11. It is also clear in these figures the effectiveness of the isolators in reducing the high vulnerability of the bridge.

The high effectiveness of the FP isolators along the entire bridge can be well appreciated in Figure 10.42, where the force-deflection cycles for the 100% ULS condition are shown for all the remaining piers in isolated and non-isolated condition in *k09* and *l02* tests. The quite linear behaviour of all piers for the bridge in the isolated condition demonstrates the effectiveness of the isolation system in reducing the high vulnerability of this kind of bridges.

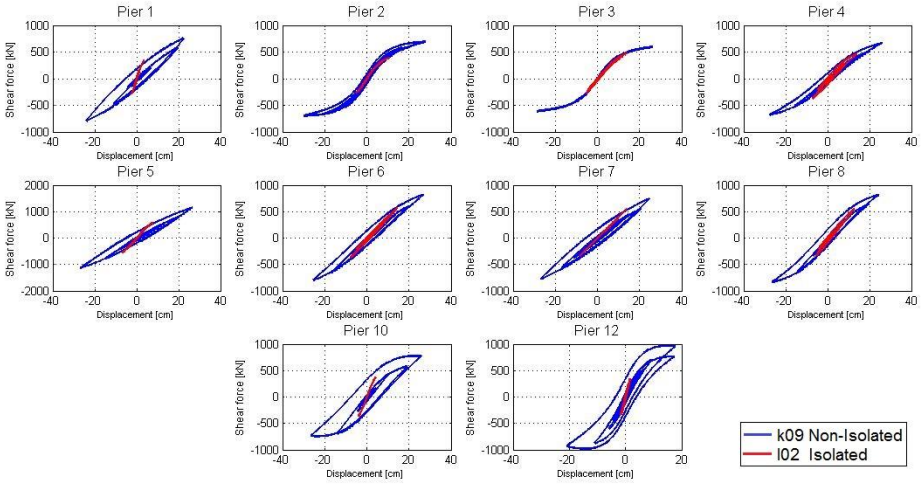

Fig. 10.42 Hysteretic cycles of all piers for isolated and non-isolated bridge 100% ULS

Finally, the effectiveness of the isolation system has been also tested using a different configuration, where the physical components of the sample model comprise only the isolator of pier 9 connected to that pier, whereas pier 9 and all other piers and isolators, are simulated numerically. For this configuration Tests r01, r02, r03 where performed, which correspond to acceleration equal to 65%, 80% and 90% of ULS, i.e. 0.25g. For such tests, the friction of the isolators is around μ=7%; the latter friction value, which is derived experimentally, is significantly higher than the design value, i.e. 4%. From a practical standpoint, it is assumed that the use of higher friction may be caused, for instance, by inadequate selection of the devices, ageing phenomena, defects in the production, etc. The latter are realistic conditions that can occur in several projects. The experimental response curves for tall and short piers are plotted in Figures 10.43 and 10.44. The force-deformation relationships are linear.

The overall numerical shear force-deformation of the remaining piers cycles are shown in Figure 10.45 for tests r01, r02 and r03. The figure shows that the behaviour remains linear in all the piers.

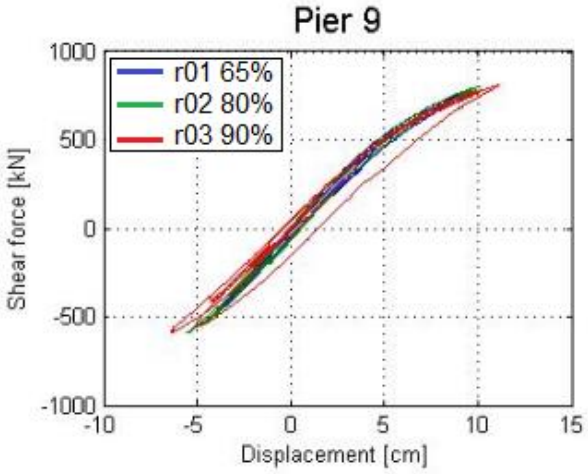

Fig. 10.43 – Force-Deflection cycle of Pier 9 during tests r01, r02 and r03 (ULS PGA=65%, 80% and 90%)

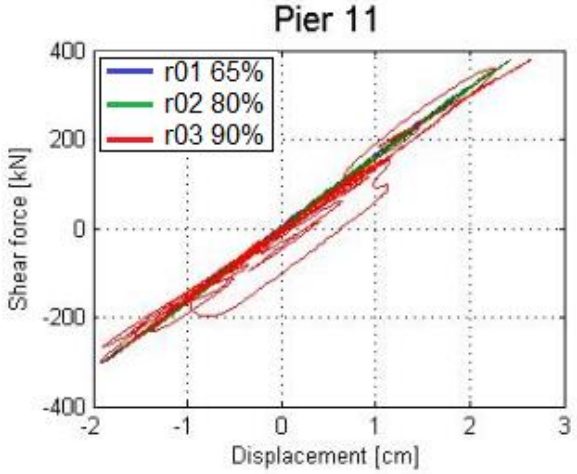

Fig. 10.44 – Force-Deflection cycle of Pier 11 during tests r01, r02 and r03 (ULS PGA=65%, 80% and 90%)

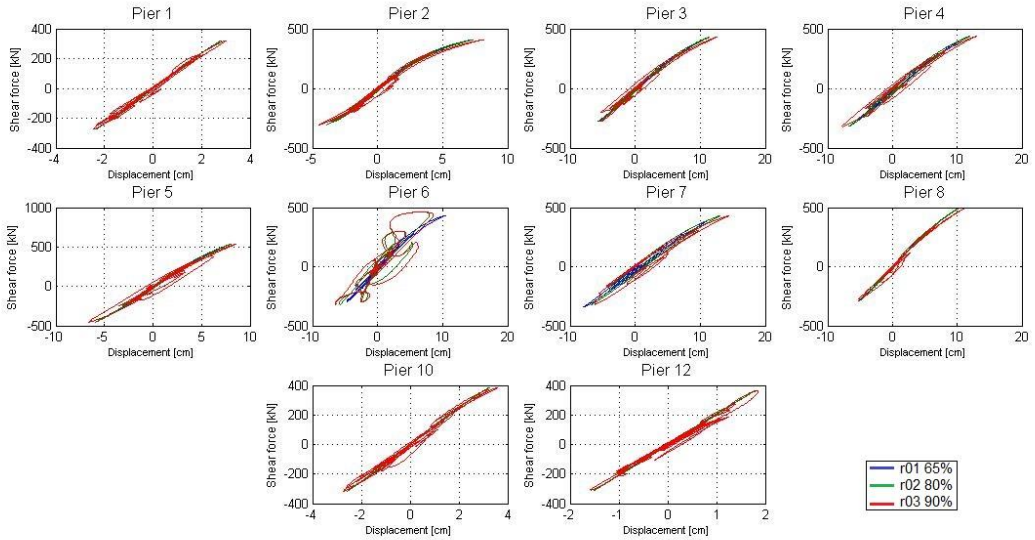

Fig. 10.45 Numerical hysteretic cycles of all piers for isolated tests r01 65%, r02 80% and r03 90% respectively, all in ULS.

11. CONCLUSIONS

The seismic vulnerability assessment of existing and new lifeline systems, especially transportation systems, is becoming of paramount importance in resilient social communities. Many transportation systems were built worldwide mainly in the late 60s and early 70s; they were designed for gravity loads and were often equipped with plain steel bars. As consequence most of the bridges do not employ seismic details and hence their structural performance is generally inadequate under earthquake ground motions. The state-of-the-art in the field of evaluation of existing bridges is scarce, it is thus urgent to propose reliable procedures for assessing the seismic vulnerability of existing bridge structures. The aim is to provide comprehensive guidelines for the seismic assessment and retrofit of existing bridges.

The “Retro” TA project funded by the European commission within the Series-project aims at studying the seismic behaviour of existing reinforced concrete (RC) bridges and the effectiveness of innovative retrofitting systems. The research activity focuses on experimental and numerical investigations of old bridges, designed chiefly for gravity loads. Towards this aim, the seismic vulnerability of an existing Italian viaduct with portal frame piers (Rio Torto Viaduct) was evaluated and an isolation system was designed using both yielding-based and friction-based bearings. An experimental test campaign was performed at ELSA Laboratory of JRC (Ispra, Italy). Two specimens (scale 1:2.5), 2 floors (total height is 6.8 m) and 3 floors (total height is 11.2 m) one-bay reinforced concrete frame respectively, were built and tested using the continuous PsD technique with non-linear substructuring; the modelling of the entire viaduct was considered along with the non-linear behaviour of each pier, due to bending, shear on the transverse beams and strain penetration effect at the column bases.

During the test two configurations have been considered: 1) retrofitted viaduct using Friction Bearings 2) “as-built” viaduct imposing several damage levels. For each phase of the experimental campaign a proper model updating has been performed. Natural records selected based on a specific hazard analysis have been used during the tests.

The comprehensive PsD campaign has shown the high vulnerability of the bridge and the needs of an earthquake protection system. In particular, an extensive damage pattern was detected during the tests, starting at the 100% ULS and exacerbated at the 200% ULS, especially in the short pier, where the transverse beam was subjected to severe cracking

damage due to shear. In addition, an important fix-end-rotation effect was shown by both piers. This is due to the high bond slip effect typical of plain steel bars used for the construction of the bridge.

Concerning base isolation, in view of the higher friction coefficient performed by the FP devices (7% with respect to the design target value of 4%), in order to assess the isolated configuration, a combination of numerical and experimental substructuring setups of the PFS isolation systems was used to prevent damage of the piers; the cause for this difference is still under investigation. Nevertheless, the effectiveness of the isolation system in protecting the bridge was verified. The isolated bridge responded in a quasi linear-elastic mode at the 100% ULS earthquake: base shear was reduced approximately by half for both piers, and displacements were reduced in average to 30% and 20% with respect to the non-isolated configuration for the tall and short piers, respectively.

Model updating was successfully used for modelling the numerical piers and, above all, it was shown that with the procedures developed by ELSA for continuous substructured PsD testing, it was possible to run for the first-time hybrid tests with the high level of complexity demanded by the simultaneous control of eighteen hydraulic actuators moving four physical experimental substructures.

Analysis and interpretation of the experimental results is still on-going, by using the data recorded by the instrumentation used in the test campaign: extensometers, strain gauges, photogrammetry. The results from this work will serve to calibrate numerical models and to provide a detailed analysis of the performance of the as-built configuration and of the effectiveness of friction pendulum systems for seismic protection, which will ultimately lead to guidelines for the assessment and design of similar structures as part of pre-Normative research in support to the Eurocodes.

REFERENCES

[1] Pinto P.E., Mancini G., (2009), Seismic assessment and retrofit of existing bridges, The state of Earthquake Engineering Research in Italy: the ReLUIS-DPC 2005-2008 Project, 111-140, © 2009 Doppiavoce, Napoli, Italy.

[2] FHWA-ATC. "Retrofitting guidelines for Highway Bridges" Report ATC-06-2, Applied Technology Council, Redwood City, California, 1983.

[3] FHWA. Seismic Retrofitting Manual for Highway Bridges, Publ. FHWA-RD-94 052, Federal Highway Administration, 1995.

[4] FHWA-MCEER. Seismic retrofitting manual for Highway Structures. Part 1-Bridges, 2006.

[5] CEN 1994. Eurocode 8—Structures in Seismic Regions—Design—Part 2: Bridges. Comitè e Europaèen de Normalisation: Brussels, 1994.

[6] CEN 2005. Eurocode 8: Design of structures for earthquake resistance – Part 3: Assessment and retrofitting of buildings, 2005.

[7] Fabbrocino G., Verderame G.M., Manfredi G., (2005). Experimental behaviour of anchored smooth rebars in old type reinforced concrete buildings. Engineering Structures27, 1575–1585.

[8] Feldman LR, Bartlett FM. Bond Strength Variability in Pull-out Specimens with plain Reinforcement. ACI Structural Journal 2005; 102(6): 860–867.

[9] Fernandes C., Melo J., Varum H., Costa A., (2011), Cyclic behaviour of a two-span RC beam built with plain reinforcing bars, Civil Engineering 55/1 (2011) 21–29, doi: 10.3311/pp.ci.2011-1.03

[10] Makris, N. and Chang, S. [2000] "Effect of viscous, viscoplastic and friction damping on the response of seismic isolated structures", Earthquake Engineering & Structural Dynamics, Vol. 29, No. 1, pp. 85-107

[11] Chang S., Makris N., Whittaker E. Thompson A. (2002), Experimental and analytical studies on the performance of hybrid isolation systems, Earthquake Engng Struct. Dyn.31:421–443

[12] Sohn H, Farrar CR, Hemez FM, Shunk DD, Stinemates DV, Nadler BR (2003) A review of structural health monitoring literature: 1996-2001. Los Alamos National Laboratory Report, LA-13976-MS.

[13] Bursi, O. S., Ceravolo, R., Erlicher, S. and Zanotti Fragonara, L. (2012), Identification of the hysteretic behaviour of a partial-strength steel–concrete moment-resisting frame structure subject to pseudo-dynamic tests. Earthquake Engng. Struct. Dyn., 41: 1883–1903. doi: 10.1002/eqe.2163,

[14] Verderame GM, Ricci P, De Carlo G, Manfredi G. Cyclic bond behaviour of plain bars. Part I: Experimental investigation, Construction and Building Materials 2009; 23(12): 3499–3511.

[15] Verderame GM, Ricci P, De Carlo G, Manfredi G. Cyclic bond behaviour of plain bars. Part II: Analytical investigation. Construction and Building Materials 2009; 23(12): 3512–3522

[16] Marefat M.S., Masood S., Shirazi H., Rostamshirazi R., Khanmohammadi M., (2009), Cyclic Response of Concrete Beams Reinforced by Plain Bars, Journal of Earthquake Engineering, 13:463–481.

[17] Paolacci, F. and Giannini, R. (2012), An experimental and numerical investigation on the cyclic response of a portal frame pier belonging to an old reinforced concrete viaduct. Earthquake Engng. Struct. Dyn., 41: 1109–1127. doi: 10.1002/eqe.1175

[18] Arani, K.K., Marefat, M.S., Di Ludovico, M., Prota, A., Manfredi, G., (2013), Hysteretic cyclic response of concrete columns reinforced with smooth bars, Bulletin of Earthquake Engineering 11 (6) , pp. 2033-2053

[19] Paolacci, F., Mohamad, A., (2010). Preliminary considerations on the seismic behaviour of the Rio-TortoViaduct. RETRO' project, Report n°1, 2010

[20] Verderame G.M., Stella A., Cosenza E., "Le proprietà meccaniche degli acciai impiegati nelle strutture in c.a. realizzate negli anni '60", X Congresso Nazionale L'ingegneria Sismica in Italia, Potenza-Matera 9-13 settembre 2001.

[21] Alessandri, S., Corritore, D., Derisi, R., Di Sarno, L., Mohamad, A.,Paolacci, F., Yenidogan, C., (2013). Numerical Simulation of the Siesmic response of the Rio-Torto Viaduct for PsD test Compaigon. RETRO' project, Report n°2, 2013

[22] Giannini R. (2000), Mathazard: a program for seismic hazard analysis, University Roma Tre

[23] Zayas, V.A., Low, S.S., Mahin, S.A., 1990, A simple pendulum technique for achieving seismic isolation, Earthquake Spectra, 6(2), 317–33.;

[24] Mokha, A., Constantinou, M.C., Reinhorn, A.M., 1991, Experimental study of friction-pendulum isolation system, Journal of Structural Engineering (ASCE), 117(4), 1201–17.

[25] Fenz, D.M. and Constantinou, M.,C. (2006). Behaviour of the double concave friction pendulum bearing. Earthquake Engineering and Structural Dynamics, 35, 1403-24

[26] Marin, C.C., 2006. Experimental and analytical study of the XY-Friction Pendulum (XY-FP) bearing for bridge applications, Ph.D thesis, State University of New York at Buffalo, Buffalo, New York

[27] Della Corte, G., De Risi, R., Di Sarno, L., (2013), Approximate method for transverse response analysis of partially isolated bridges, Journal of Bridge Engineering 18 (11) , pp. 1121-1130

[28] Priestley, M.J.N., Calvi, G.M., Kowalsky, M.J., 2007. Displacement-Based Seismic Design of Structures. IUSS PRESS, Pavia, Italy

[29] Kumar S., Itoh Y., Saizuka K., Usami T. (1997), Pseudodynamic Testing of Scaled Models, Journal of Structural Engineering. 123: 4.

[30] Krawinkler, H. “Scale effects in static and dynamic model testing of structures.” 9th World Conference on Earthquake, Engineering, Tokyo-Kyoto, Japan, Vol. VIII, 1988; 865–876.

[31] Priestley M.J.N., Verma R., and Xiao Y., “Seismic Shear Strength of Reinforced, Concrete Columns,” ASCE Journal of Structural Engineering, Vol. 120, 8, Aug., 1994, pp. 2310-2329.

[32] Ichinose T, Kanayamab AY, Inouec Y, Bolander JE Jr. Size effect on bond strength of deformed bars. Construction and Building Materials 2004; 18: 549–558.

[33] Pinto PE, Mancini G. Seismic assessment and retrofit of existing bridges. Final Report, Reluis DPC project, 2005–2009, (2009). (http://www.reluis.it)

[34] Bazant Z, Sener S. “Size Effect in Pullout Tests.” ACI Materials Journal 1988; 5: 347–351

[35] De Risi, R., Di Sarno, L., Della Corte, G., Paolacci F., Marioni A., and Taucer, F. (2011). Seismic analysis and retrofitting of an existing RC highway bridge Part II: Analysis of the isolated bridge. Proceedings of the 14th Italian National Conference on Earthquake Engineering, Bari, CD Rom.

[36] Dermitzakis S. N. and Mahin. S. A., (1985), Development of substructuring techniques for on-line computer controlled seismic performance testing. Technical report, Earth.Eng. Research Center, Univ. of California, Berkeley, CA, USA, 1985. Report No. UCB/EERC-85/04.

[37] G. Magonette. (2001), Development and application of large-scale continuous pseudodynamic testing technique. Phil. Trans. R. Soc. Lond. A, 359:1771–1799.

[38] Gravouil A. and Combescure A.. (2001), Multi-time-step explicit-implicit method for nonlinear structural dynamics. Int. J. Numer. Meth.Engng, 50:199–225.

[39] Pegon P and Magonette G., (2002). Continuous PsD testing with non-linear substructuring: presentation of a stable parallel inter-field procedure. JRC-Special publication No.SPI.02.167.

[40] M. Nakashima, T. Akazawa, and O. Sakaguchi. (1993). Integration method capable of controlling experimental error growth in substructure pseudo dynamic test.AIJ J. of Struct. Constr. Engng., 454:61–71.

[41] Combescure D. and Pegon P. (1997), α-operator splitting time integration technique for pseudodynamic testing: error propagation analysis. Soil Dynamics & Earthquake Engineering, 16:427–443.

[42] Pegon P. and Magonette G. (2005). Continuous PsD testing with non-linear substructuring: using the operator splitting technique to avoid iterative procedures. JRC-Special publication No.SPI.05.30.

[43] P. Pegon. Continuous PsD Testing With Substructuring. In O. S. Bursi and D. J. Wagg, editors, Modern Testing Techniques for Structural Systems, Dynamics and Control.CISM, 2008.

[44] Bonelli, A., Bursi O.S., He L., Magonette G., Pegon P. (2008). Convergence analysis of a parallel interfield method for heterogeneous simulations with dynamic substructuring. Int. J. Numer. Meth.Engng, 75:800–825.

[45] Millard A. (1993). CASTEM 2000, Guide dutilisation. Saclay, France. Rapport CEA 93/007.

[46] Menegotto M. and Pinto P.E. (1973). Method of Analysis for Cyclically Loaded R.C. Plane Frames Including Change in Geometry and Non-Elements Behaviour of Elements under Combined Normal Force and Bending. Proc. of IABSE Symposium on Resistance and Ultimate Deformability of Structures Acted on by Well Defined Repeated Loads, Vol.13, 1973: 15-22

[47] Zhao J, Sritharan S. (2007). Modelling of strain penetration effects in fiber-based analysis of reinforced concrete structures. ACI Structural Journal; 104(2): 133–141

[48] Ceresa P, Petrini L, Pinho R. (2007). Flexure-shear fiber beam-column elements for modelling frame structures under seismic loading – state of art. Journal of Earthquake Engineering; 11: 46–88

[49] Hildago PA, Jordan RM, Martinez MP. (2002). An analytical model to predict the inelastic seismic behaviour of shear-wall reinforced concrete structures. Engineering Structures; 24: 85–98.

[50] D'Ambrisi A, Filippou FC. (1999). Modelling of cyclic shear behaviour in RC members.Journalof Structural Engineering ASCE; 125(3): 1143–1150.

[51] Lee DH, Choi E, Zi G. (2005), Evaluation of earthquake deformation and performance for RC bridge piers. Engineering Structures; 27: 1451–1464

[52] Priestley MJN, Seible F, Calvi GM. (1996). Seismic Design and Retrofit of Bridges. Wiley:New York.

[53] Bentz EC. (2000). Sectional Analysis of Reinforced Concrete Members", PhD Thesis, Department of Civil Engineering, University of Toronto, 2000, 310

[54] Vecchio FJ, Collins MP. (1998), "Predicting the response of reinforced concrete beams subjected to shear using the modified compression field theory." ACI Structural Journal; 85(3): 258–268.

[55] Balan T., Filippou FC, Popov EP. (1998), "Hysteretic Model of Ordinary and High Strength Reinforcing Steels". Journal of Structural Engineering, American Society of Civil Engineers 1998; 124(3): 288–297

[56] Schellenberg A. (2010). Single Concave Friction Pendulum Bearing Element. Opensees Wiki. Available at http://opensees.berkeley.edu/wiki/index.php/Single_Concave_Friction_Pendulum_Beari ng_Element Date last accessed, Dec. 31th 2012

[57] Guyan J (1965) Reduction of stiffness and mass matrices. AIAA,N. 3

[58] Craig R and Bampton M (1968) Coupling of substructures in dynamic analysis. AIAA, N. 6

[59] Mostaghel, N. (1999). Analytical Description of Pinching, Degrading Hysteretic Systems. Journal of Engineering Mechanics, 125(2), 216–224. doi:10.1061/(ASCE)0733-9399(1999)125:2(216)

[60] Newmark, N.M., 1965. A method of computation for structural dynamics. Journal of the Engineering Mechanics Division, 3:67-94

[61] Pegon, P., Molina, F. J. and Magonette, G. , 2008, Continuous pseudo-dynamic testing at ELSA. Hybrid Simulation; Theory, Implementation and Applications, ed. SaoumaV.E.andSivaselvan M. V. (Taylor & Francis/Balkema) 79-88.

[62] Lomiento G., Bonessio N. and Benzoni G., (2013), Journal of Earthquake Engineering (2013): Friction Model For Sliding Bearings Under Seismic Excitation, DOI: 10.1080/13632469.2013.814611.

[63] Alessandri, S., Giannini, R. and Paolacci, F. (2013), Aftershock risk assessment and the decision to open traffic on bridges. Earthquake Engng. Struct. Dyn., 42: 2255–2275. doi: 10.1002/eqe.2324

ANNEX A: PHOTOGRAPHIC RECORDS

Figure A.1 Foundation Steel work

FigureA.2 Longitudinal and spiral steel in the columns

Figure A.3 Transversal beam construction

Figure A.4 Concrete pouring on beams

Figure A.5 Prestressing bars at top of the piers

Figure A.6 Completed Construction piers

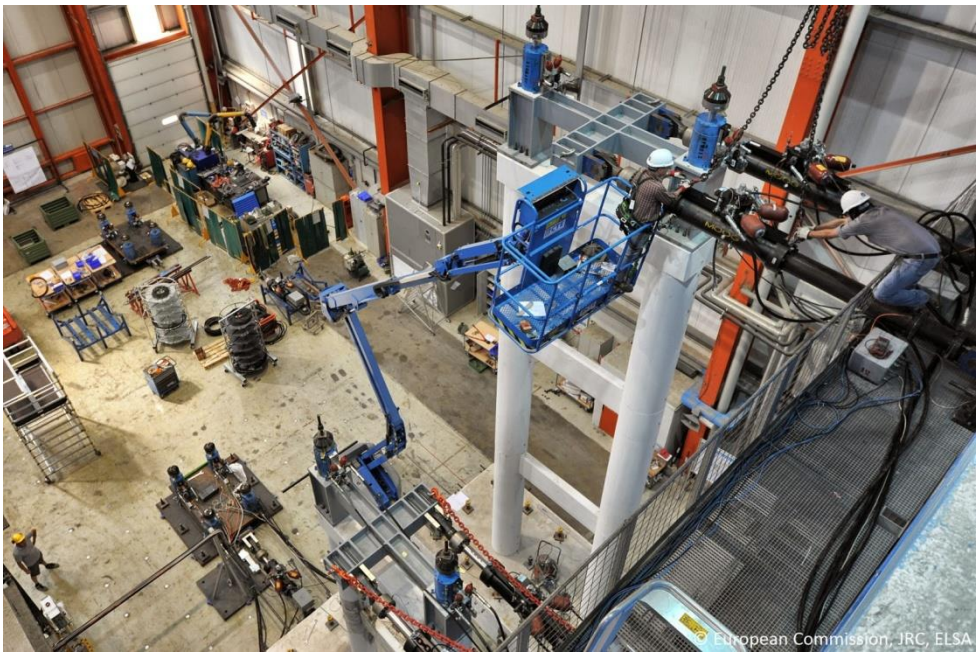

Figure A.7 Piers inside ELSA lab

Figure A.8 Connecting hydraulic actuators at the top of piers

ANNEX B: MOCK-UP DRAWINGS

Pier 9 : overall dimensions

Table : 1

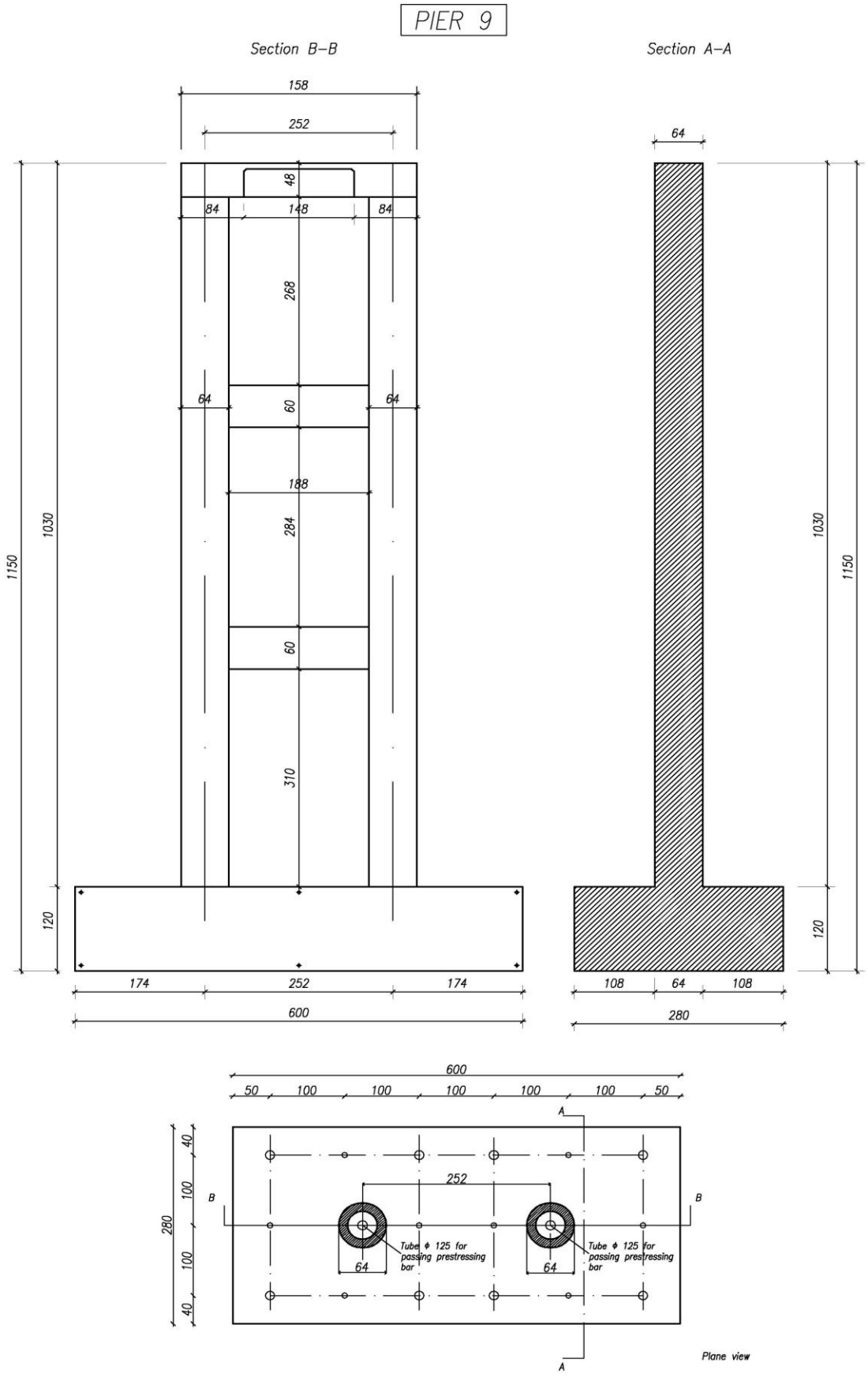

Description of tables for pier 9

Table : 2

PIER 9

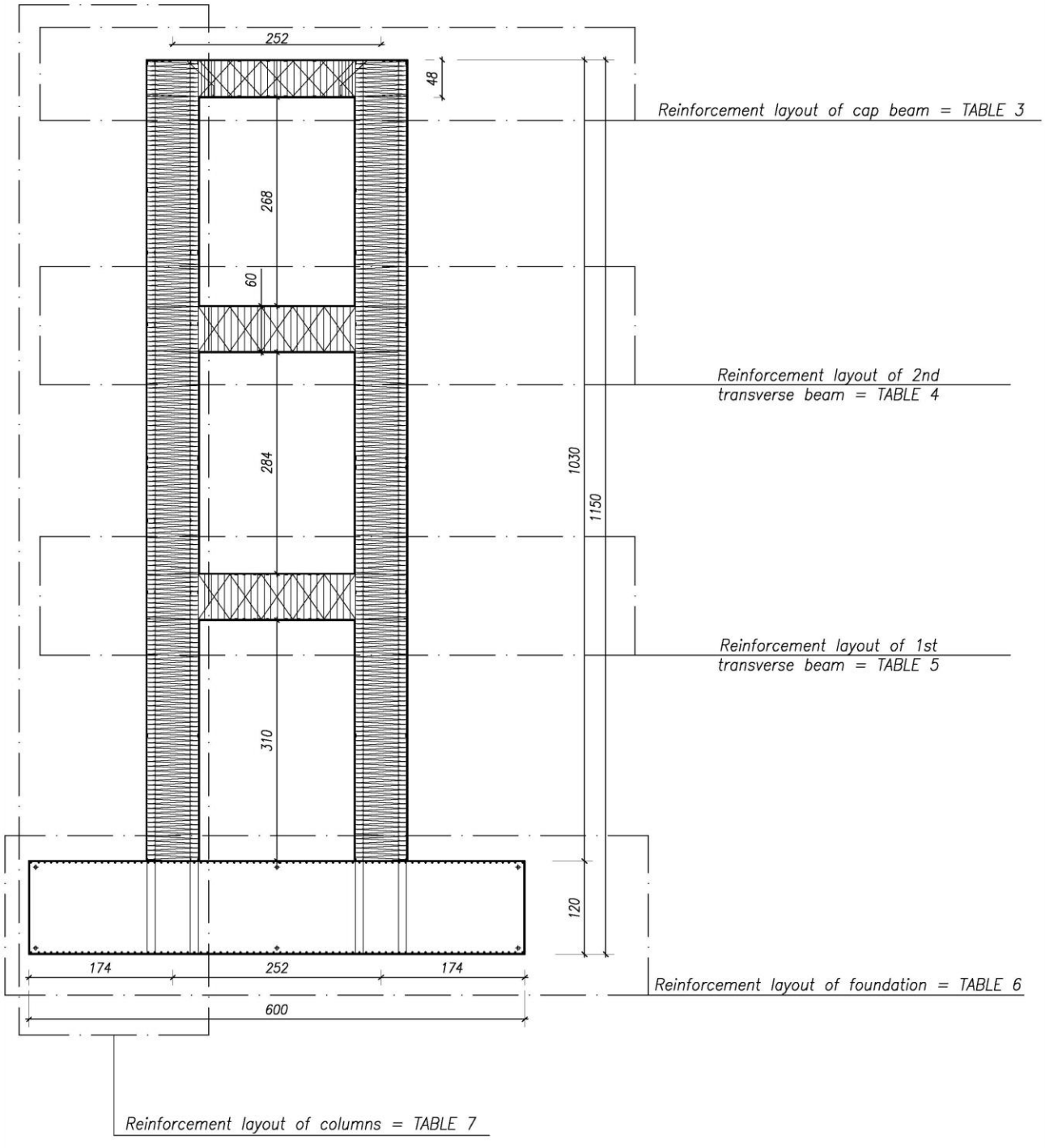

Reinforcement layout of cap beam

Table : 3

TOP BEAM PIER 9

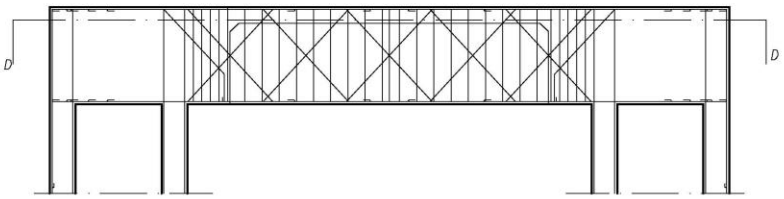

Pos. 16 e pos 23

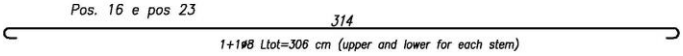

Pos. 17

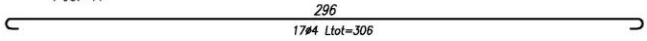

Pos. 18

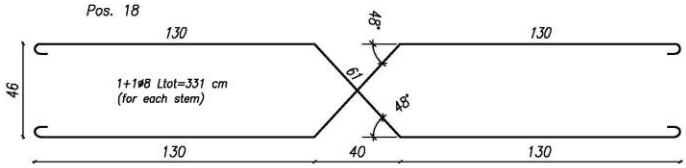

Pos. 19

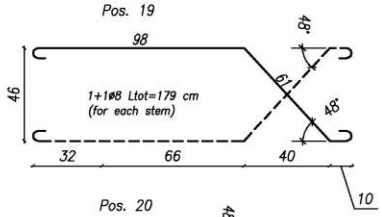

Pos. 19

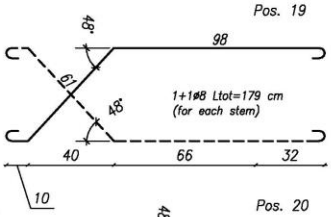

Pos. 20

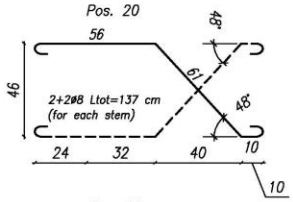

Pos. 20

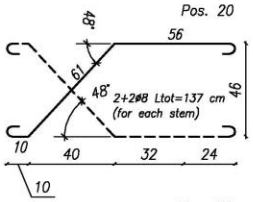

Pos. 21

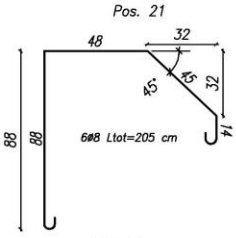

Pos. 21

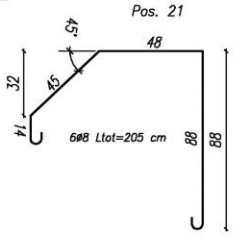

Pos. 22

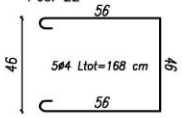

Pos. 22

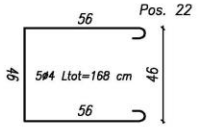

Section E–E

Pos. 27 1+1ø4/10 cm L = 68 cm

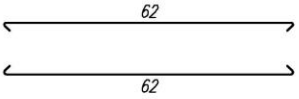

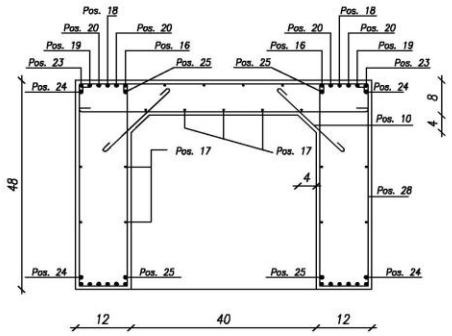

Pos. 28 1ø4/10 cm L = 108 cm

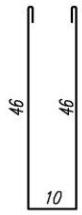

Pos. 29 16ø4 L = 184 cm

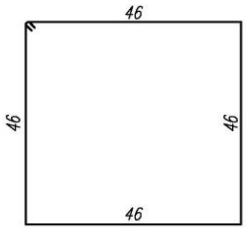

Pos. 30 1ø4/10 cm L = 26 cm

Section D–D

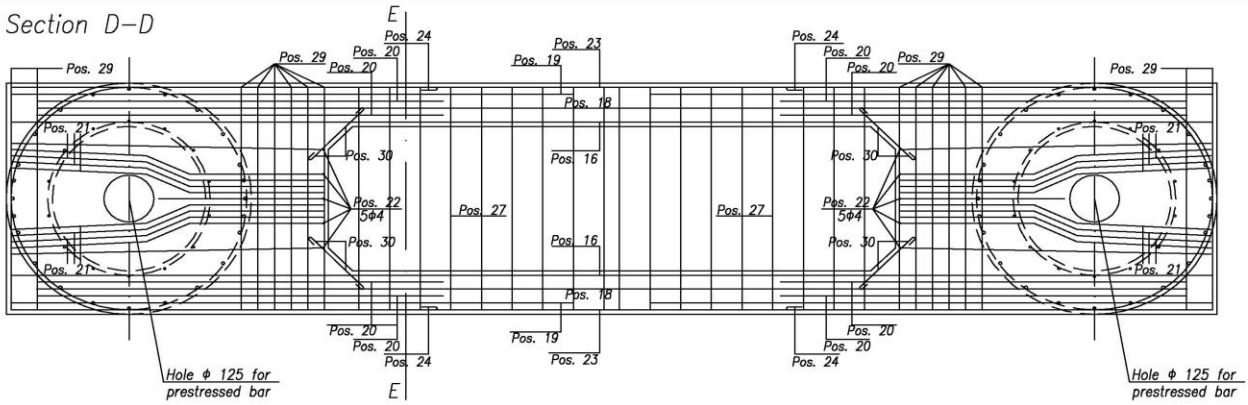

Reinforcement layout of 2nd transverse

Table : 4

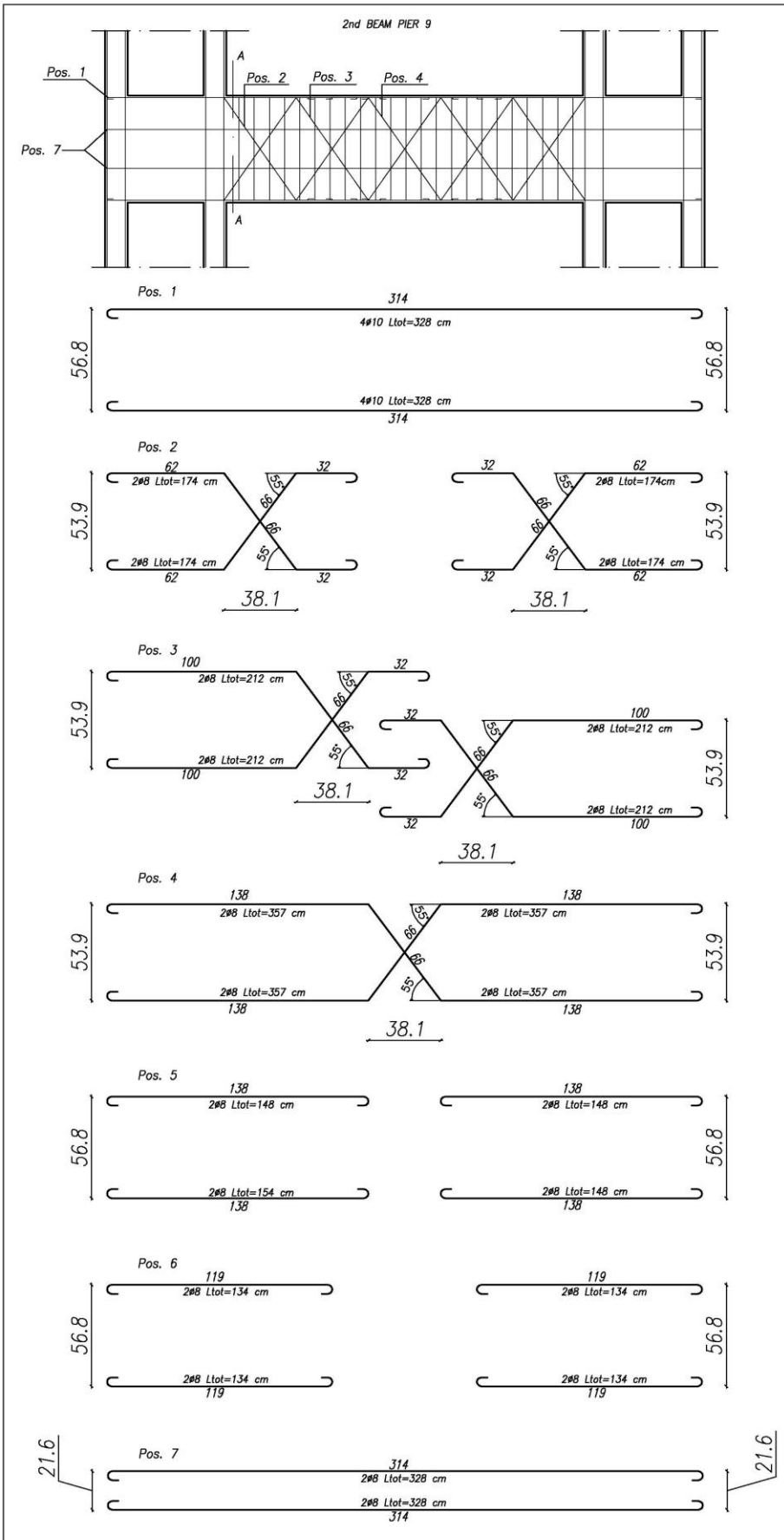

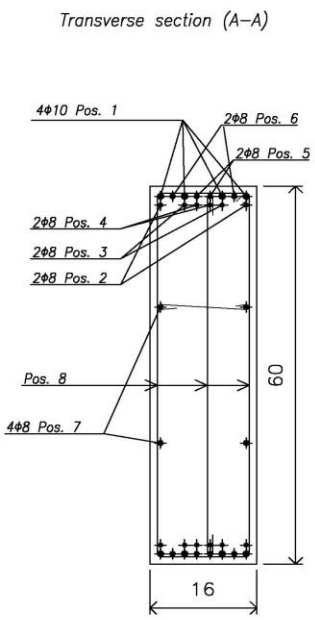

L = 23 cm
2ϕ3 each 10cm

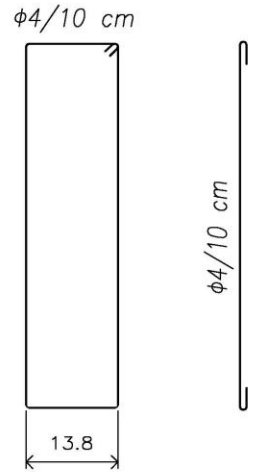

Reinforcement layout of 1st transverse

Table : 5

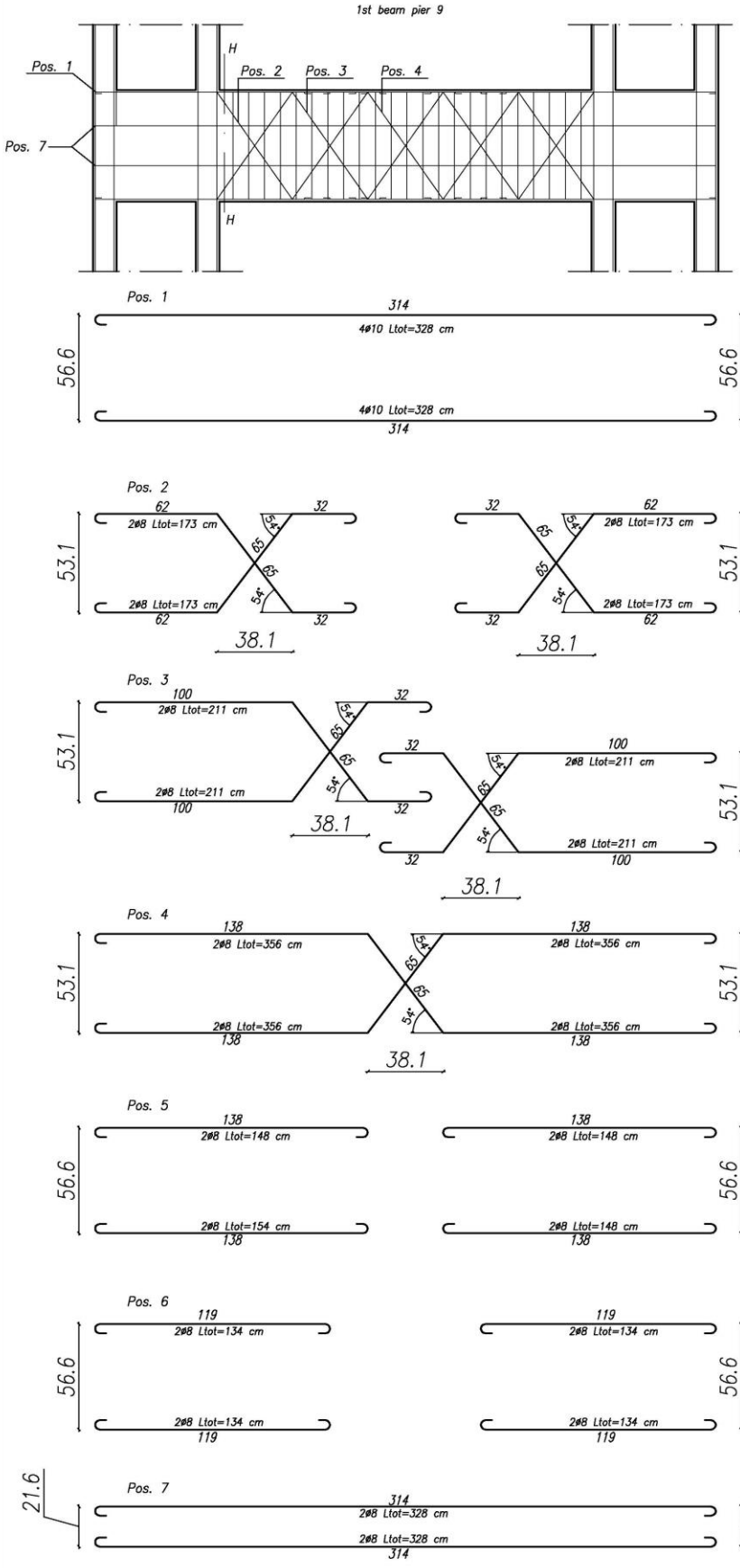

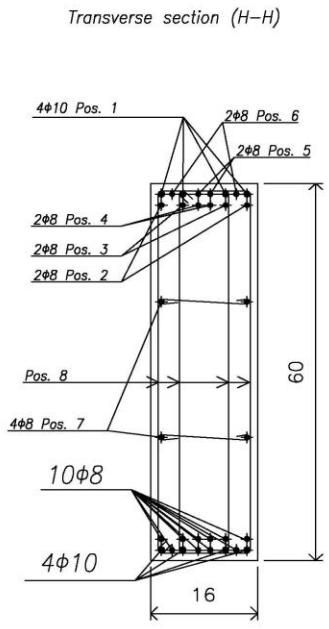

L = 22 cm

2ϕ3 each 10cm

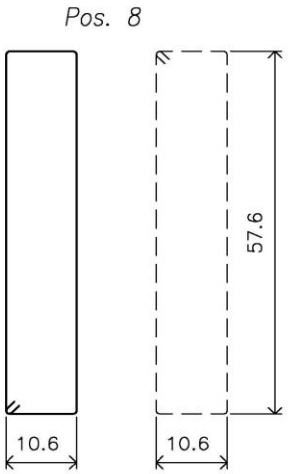

1+1ϕ4/10 cm

Reinforcement layout of foundation

Table : 6

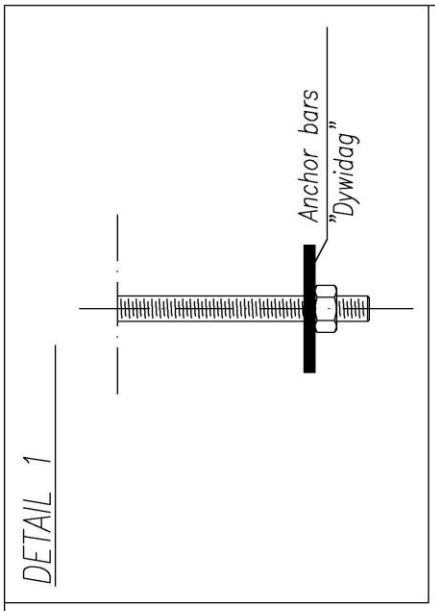

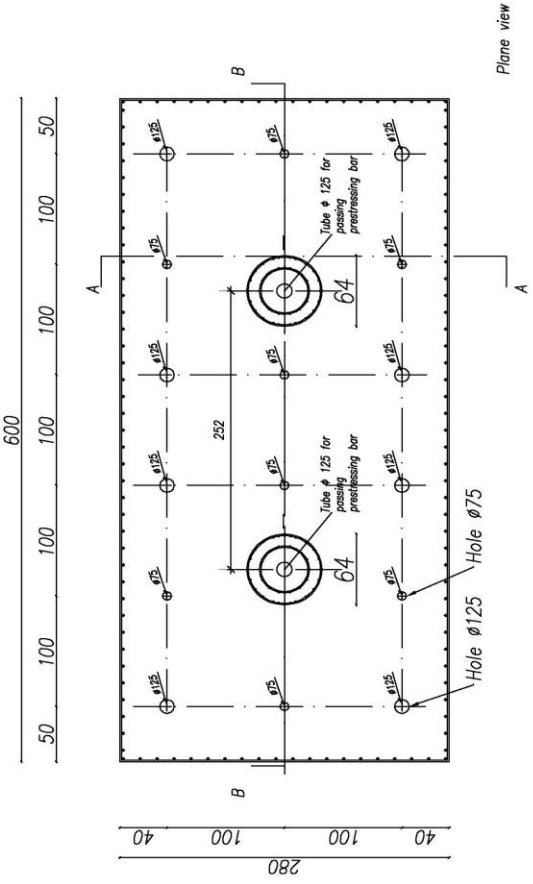

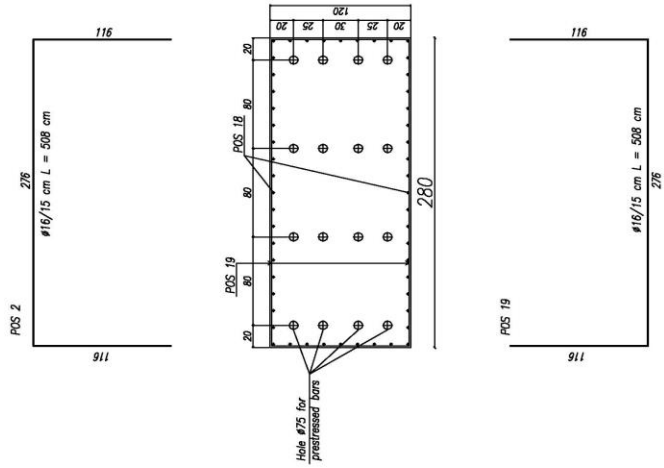

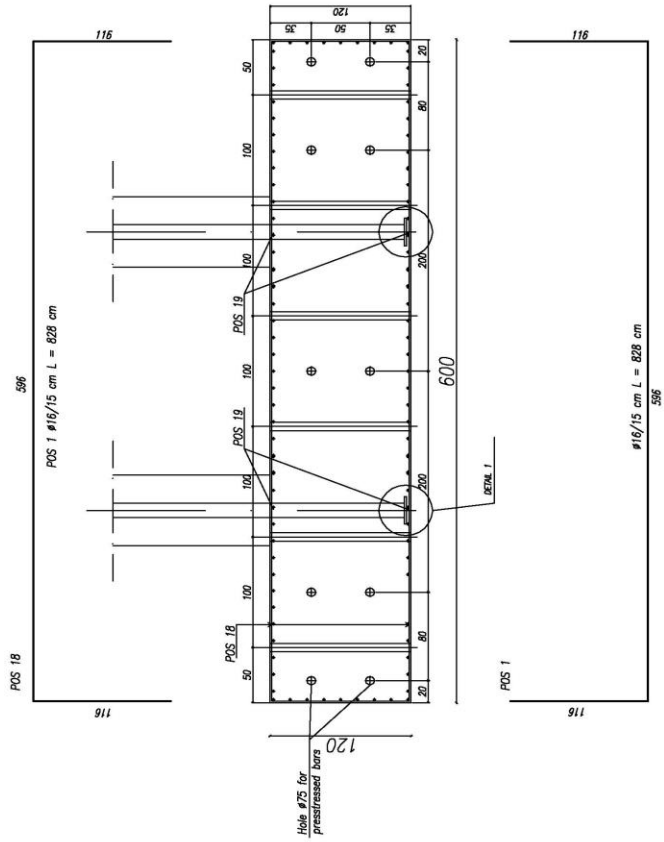

* Ribbed bars B450C

Reinforcement layout of colums

Table : 7

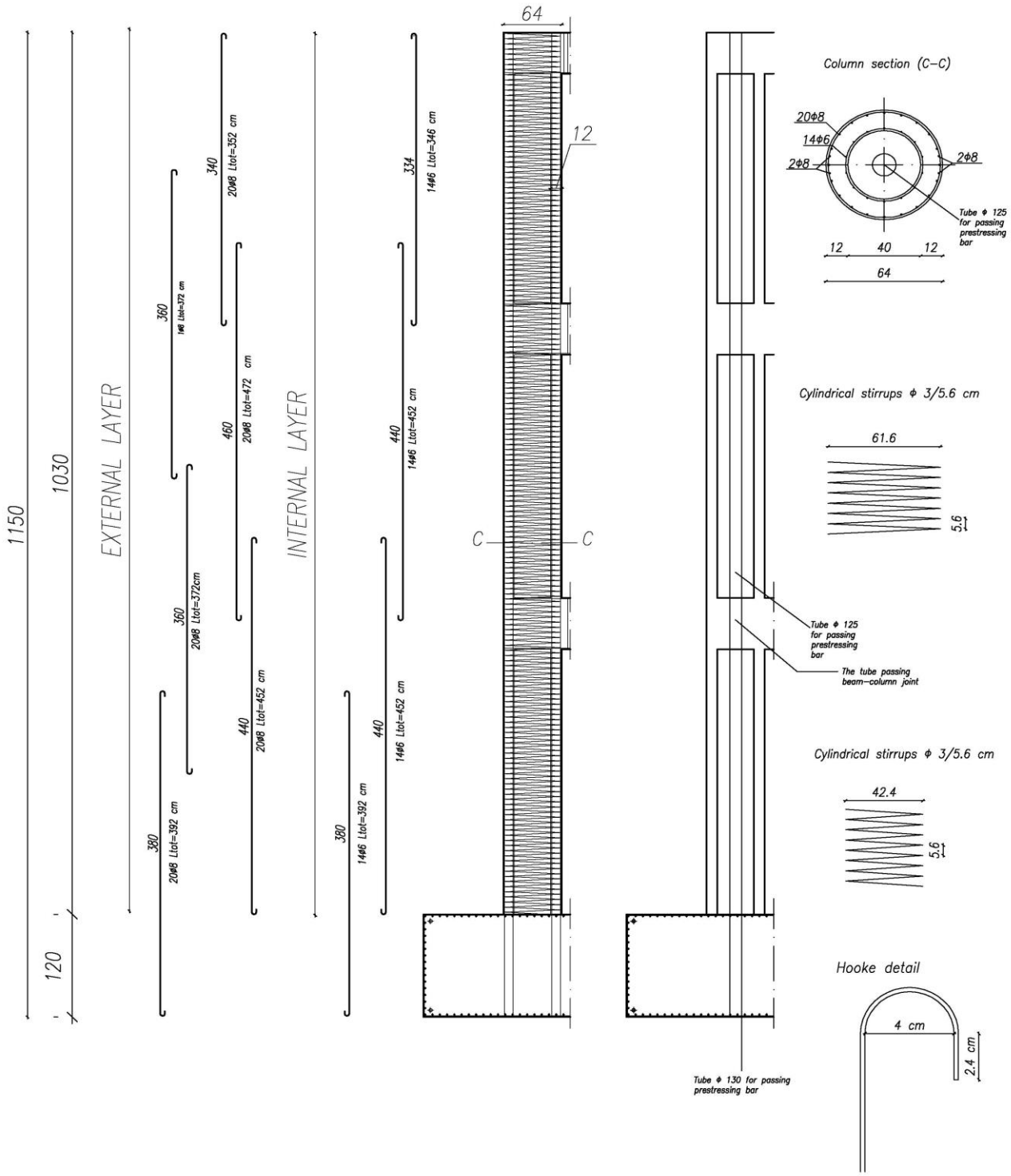

Pier 11 : overall dimensions

Table : 8

PIER 11

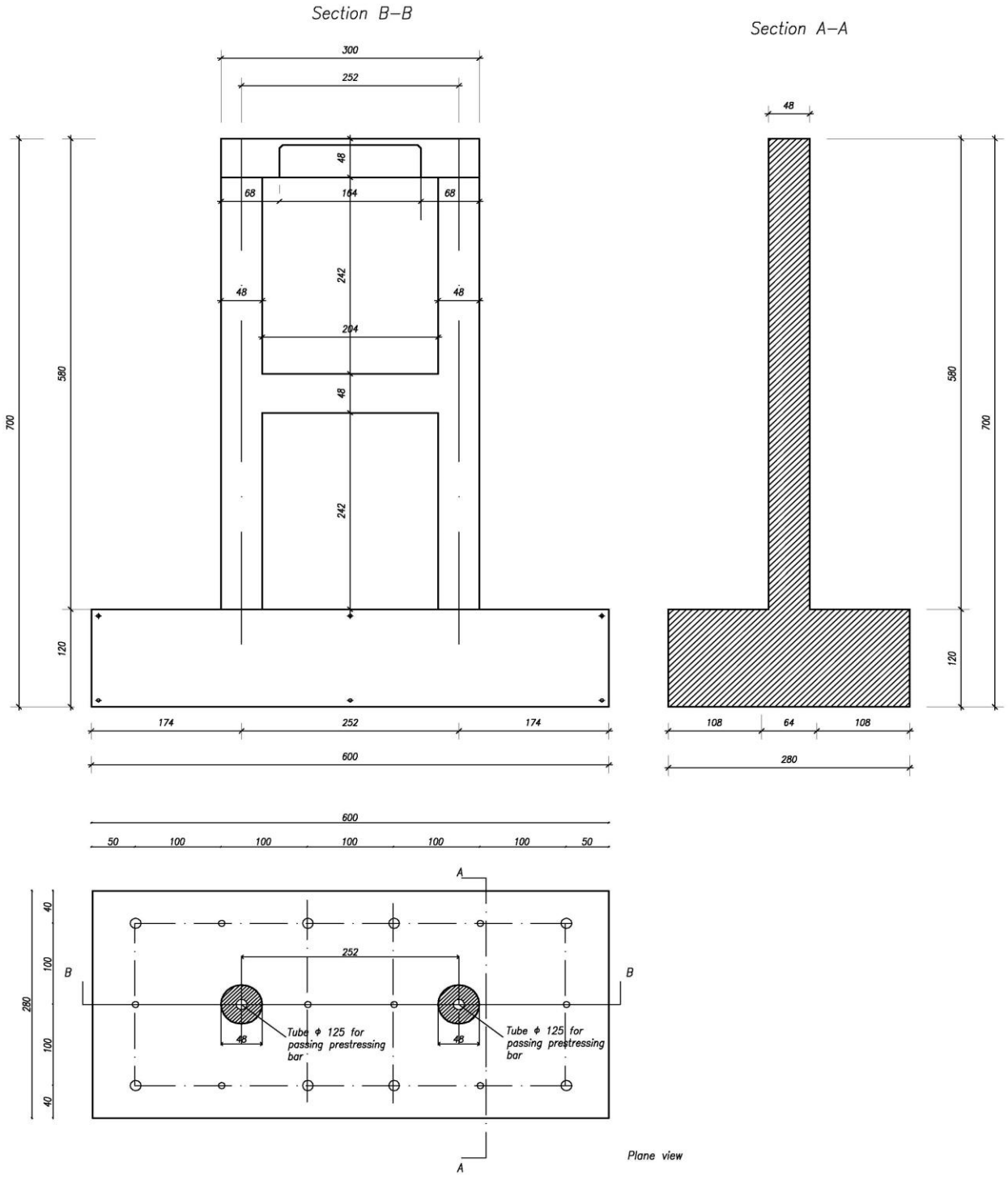

Description of tables for pier 11

Table : 9

PIER 11

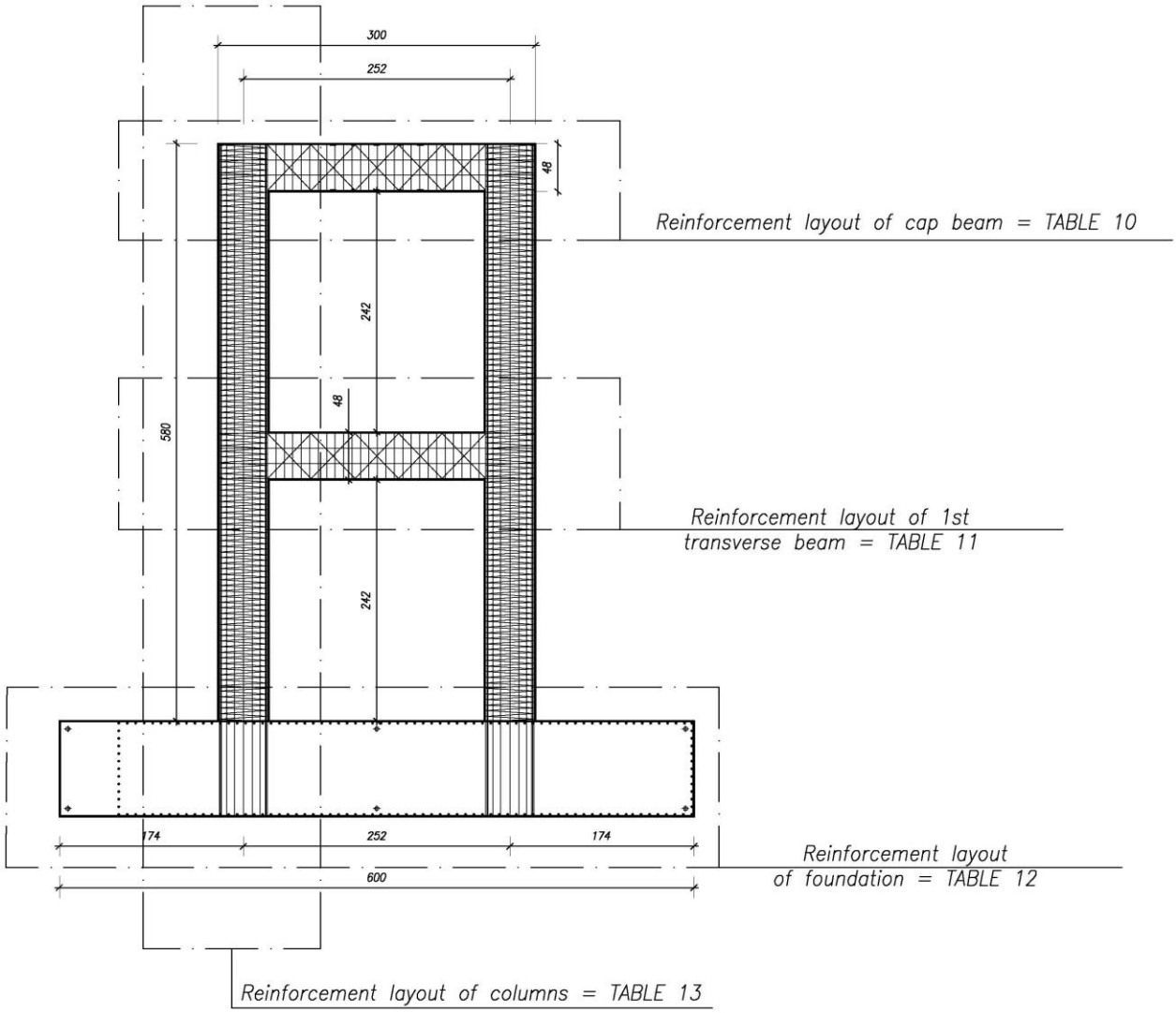

Reinforcement layout of cap beam

Table : 10

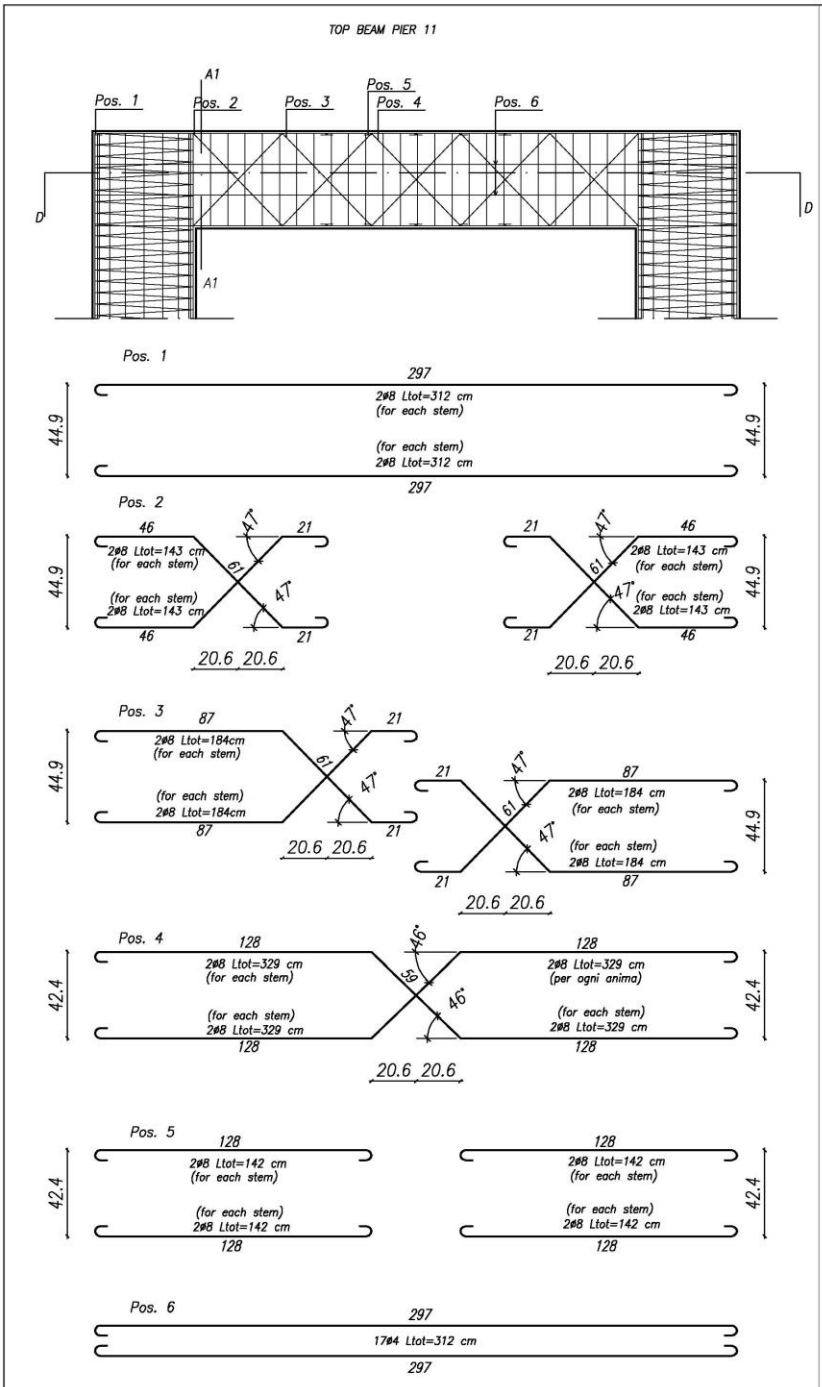

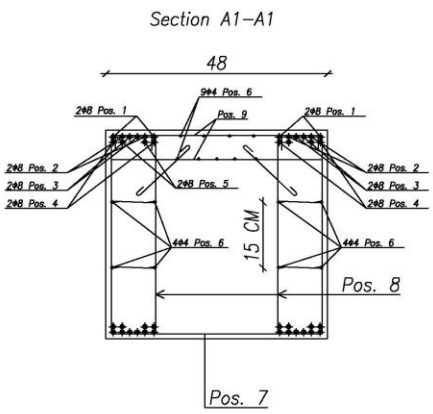

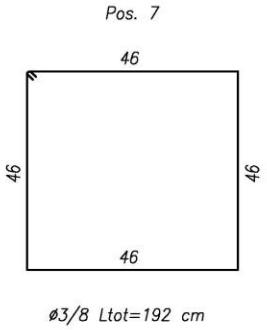

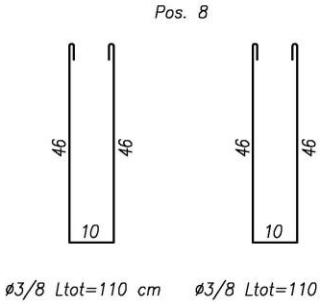

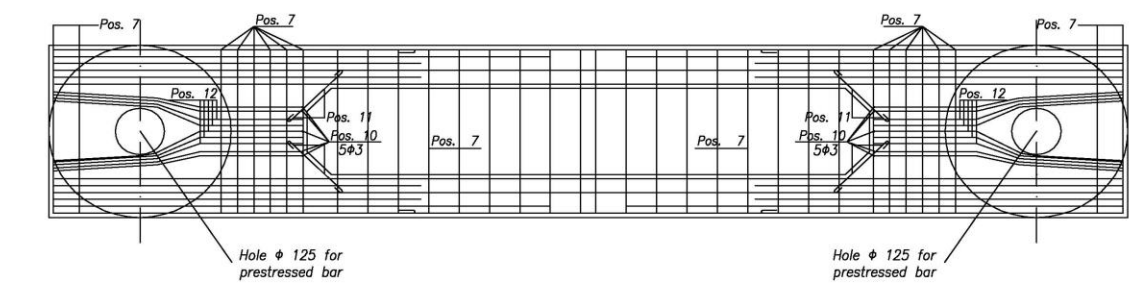

Reinforcement layout of 1st transverse

Table : 11

Reinforcement layout of foundation

Table : 12

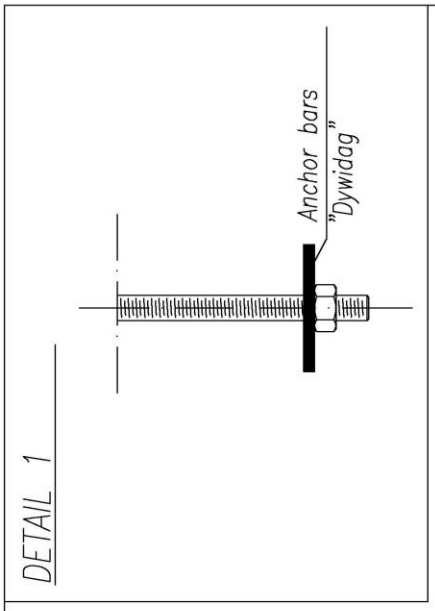

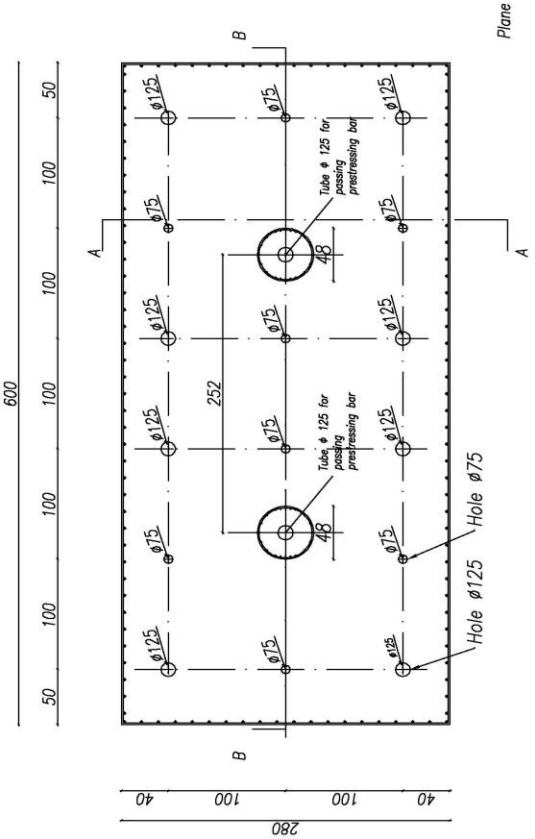

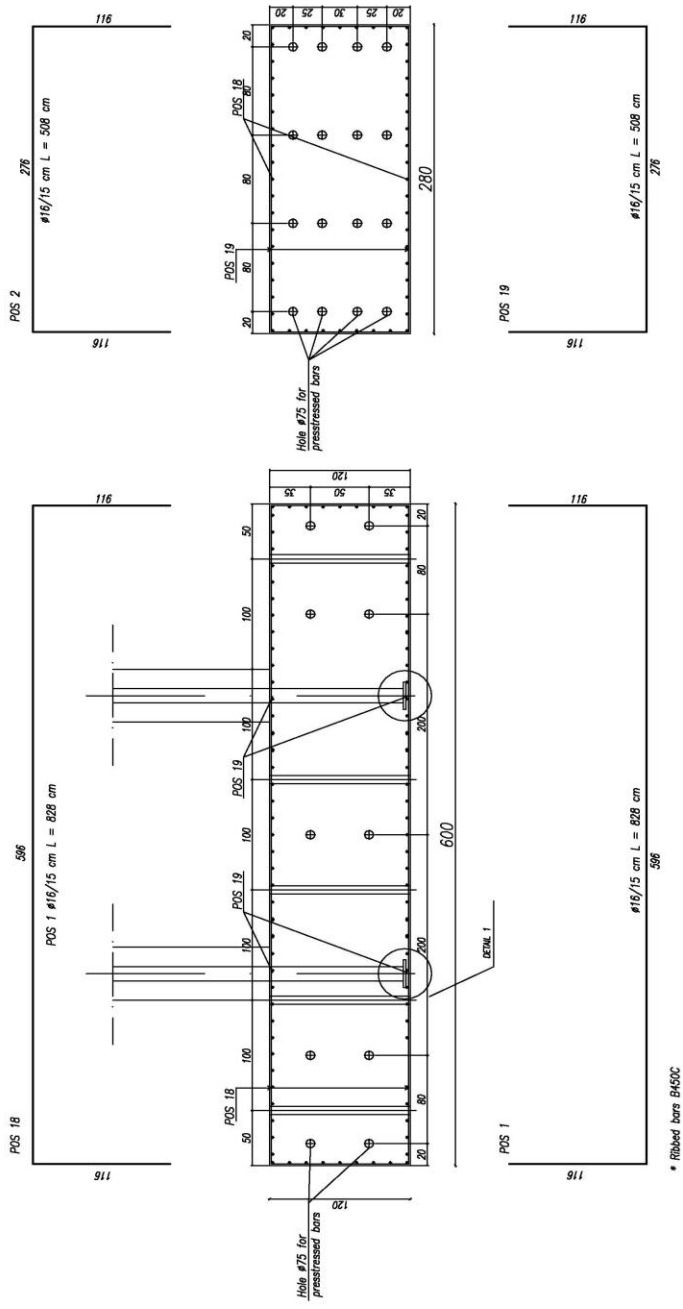

Reinforcement layout of colums

Table : 13

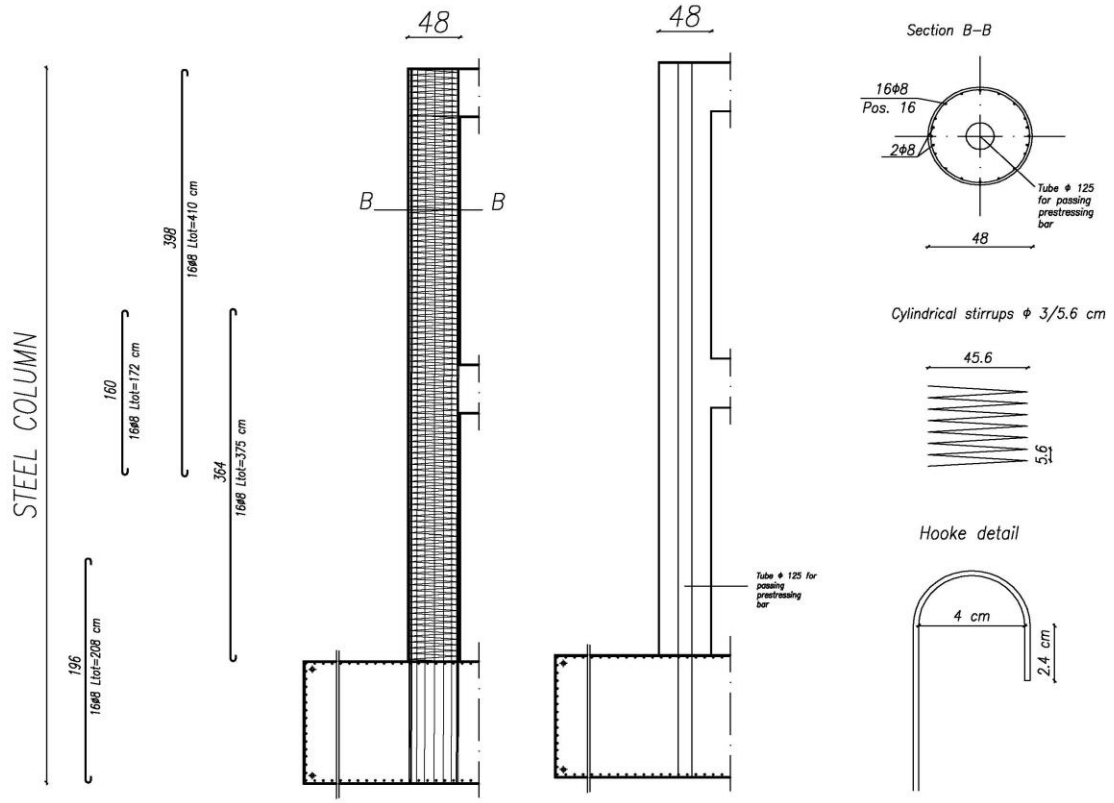

European Commission
EUR 26471 EN – Joint Research Centre – Institute for the Protection and Security of the Citizen

Title: **Assessment of the seismic vulnerability of an old RC viaduct with frame piers and study of the effectiveness of base isolation through PsD testing (RETRO)**

Authors: Fabrizio Paolacci, Pierre Pegon, Francisco Javier Molina, Martin Poljansek, Renato Giannini, Luigi Di Sarno, Giuseppe Abbiati, Arkam Mohamad, Oreste Bursi, Fabio Taucer, Rosario Ceravolo, Philippe Caperan, Luca Zanotti Fragonara, Raffele De Risi, Mauro Sartori, Silvia Alessandri Cem Yenidogan

Luxembourg: Publications Office of the European Union

2014 – 144 pp. – 21.0 x 29.7 cm

EUR – Scientific and Technical Research series – ISSN 1831-9424

ISBN 978-92-79-36477-8

doi: 10.2788/33048

Abstract
The RETRO project aims at studying the seismic behaviour of existing reinforced concrete bridges (RC) and the effectiveness of innovative retrofitting systems. Emphasis has been paid on old bridges generally not properly designed for seismic action. On the basis of a previous experimental campaign consisting of cyclically imposed displacements on 1:4 reduced scale models of a frame pier, belonging to a typical old RC highway viaduct, a new experimental activity has been proposed. Two specimens (scale 1:2.5), a frame pier of 2 levels (height 5.8 m) and a frame pier of 3 levels (height 10.3 m), have been built and tested using the continuous Pseudo-dynamic (PsD) method with non-linear substructuring technique, including the modelling of the remaining entire viaduct to which they belong. Two test configurations have been considered: 1) retrofitted viaduct using Friction Pendulm Isolators, and an 2) "as-built" configuration imposing a Serviceability and Ultimate limit state conditions. For each phase of the experimental campaign model identification has been performed. The aim of the campaign was twofold: 1) increasing the knowledge on the non-linear behaviour of RC frame piers in presence of plain steel bars and detailing of the late 1950's for which few studies have been carried out, and 2) study the effectiveness of seismic isolation systems for the seismic response mitigation.

LB-1A-26471-EN-N

As the Commission's in-house science service, the Joint Research Centre's mission is to provide EU policies with independent, evidence-based scientific and technical support throughout the whole policy cycle.

Working in close cooperation with policy Directorates-General, the JRC addresses key societal challenges while stimulating innovation through developing new standards, methods and tools, and sharing and transferring its know-how to the Member States and international community.

Key policy areas include: environment and climate change; energy and transport; agriculture and food security; health and consumer protection; information society and digital agenda; safety and security including nuclear; all supported through a cross-cutting and multi-disciplinary approach.

Publications Office

ISBN 978-92-79-36477-8